MEASUREMENT OF STRESS IN III-V SEMICONDUCTORS

MEASUREMENT OF STRESS IN III-V SEMICONDUCTORS USING THE DEGREE OF POLARIZATION OF LUMINESCENCE

By

PAUL DWIGHT COLBOURNE, B.Sc., B.Eng., M.Eng.

A Thesis

Submitted to the School of Graduate Studies

in Partial Fulfilment of the Requirements

for the Degree

Doctor of Philosophy

McMaster University

DOCTOR OF PHILOSOPHY (1992)
(Engineering Physics)

McMASTER UNIVERSITY
Hamilton, Ontario

TITLE: Measurement of Stress in III-V Semiconductors using the Degree of Polarization of Luminescence

AUTHOR: Paul Dwight Colbourne, B.Sc. (Mount Allison University)
B.Eng. (Technical University of Nova Scotia)
M.Eng. (McMaster University)

SUPERVISOR: Professor D. T. Cassidy

NUMBER OF PAGES: ix, 130

Abstract

The techniques of polarization-resolved electroluminescence and photoluminescence have been demonstrated to be accurate methods of measuring mechanical stress in luminescent semiconductors. These techniques have been applied to measure stresses in AlGaAs/GaAs and InGaAsP/InP superluminescent diodes and diode lasers and bulk GaAs and InP crystals. Stresses due to various diode laser manufacturing processes have been measured. Individual dislocations in bulk crystals and strained epitaxial layers have been detected and characterized by their stress patterns.

Acknowledgements

I would like to thank my supervisor, Dr. Dan Cassidy, for his foresight in proposing this research, and for his encouragement and guidance during my Ph.D. studies. I am fortunate to have had the use of the scanning setup and software which Frank Peters developed during his studies at McMaster. Charles Adams deserves the credit for laying the groundwork of polarization-resolved measurements.

I wish to acknowledge financial support from the Natural Sciences and Engineering Research Council of Canada, the Department of Engineering Physics at McMaster, and indirectly from EG&G Optoelectronics and the Ontario Ministry of Colleges and Universities through a URIF grant. The diode samples were provided by EG&G Optoelectronics and the National Research Council of Canada. Dan Mitchell and Brad Robinson of McMaster University provided the MBE-grown samples used in the dislocation studies.

And of course my parents deserve thanks for their many years of support.

Table of Contents

List of Figures

Chapter 1. Introduction

1.1 Background

Mechanical stress in GaAs and InP-based diode lasers and LED's is of concern to manufacturers because it has been correlated with reduced lifetimes of the devices. Increased degradation has been attributed to externally-applied stress [1,2], oxide stress [3,4,5], ridge waveguide stresses [6], bonding stress [7,8], lattice mismatch stress [9,10,11], and thermal stress [12]. Stress can affect the optical properties of diode lasers, including the threshold current [13,14,15,16] and the polarization state of the light output above threshold [16,17,18,19]. Stress can induce changes in the refractive index profile in and around the active region of the laser due to the photoelastic effect, affecting the waveguiding properties of the active region [20]. To have better control over the device performance, manufacturers would like to be able to measure quickly and accurately the stresses induced by the various manufacturing processes.

Measurements of stress in laser diodes and other semiconductor devices have been previously done using several techniques, including micro-Raman spectroscopy [21,6], X-ray Automatic Bragg Angle Control (ABAC) diffraction [22,23,24], X-ray topography [25], cathodoluminescence spectroscopy [26], photoluminescence spectroscopy [27], electron beam induced current (EBIC) [28], and infrared

birefringence [29]. However, none of these techniques are completely satisfactory for diode laser analysis. The stress resolution of Raman spectroscopy, cathodoluminescence spectroscopy, and photoluminescence spectroscopy is relatively low due to the small change in the emission wavelength compared to the width of the peak. Therefore these techniques do not have sufficient sensitivity to measure the stresses of about 10^8 dyn/cm^2 which have been linked with increased device degradation in AlGaAs diode lasers [5,10,11]. X-ray ABAC diffraction measurements of the radius of curvature of the device crystal reveal only the average stress over the entire surface [23], which does not necessarily indicate the stress at the active region. EBIC is not yet a quantitative technique, and requires long exposures (10 hours or more) of electron irradiation before the stress effects become apparent. The spatial resolution of about 15 μm of infrared birefringence and the spatial resolution of about 5-10 μm of X-ray topography are not sufficient for diode laser analysis.

Recently, polarization-resolved electroluminescence has been shown to indicate the stress in the active layer of diode lasers [30]. Polarization-resolved electroluminescence is limited to measuring the stress in the light-emitting active region, but usually the active region is the area of greatest interest. In some of the work reported in this thesis, polarization-resolved electroluminescence was used to measure stresses in the active region of GaAs/AlGaAs diode lasers and superluminescent diodes (SLD's). The success of the electroluminescence experiments suggested the use of polarization-resolved photoluminescence to enable accurate stress measurements to be performed without being limited to the light-emitting active region. Both of these techniques are

based on the effect of stress on the polarization state of luminescence from a semiconductor. For unstressed GaAs and InP semiconductors, the probability of emission of a photon polarized in a given direction is independent of the direction. A uniaxial tensile stress causes a reduced probability of emission of light polarized in the direction of the stress. To quantify the polarization state of the luminescence, the degree of polarization ρ can be calculated,

$$\rho = \frac{L_x - L_z}{L_x + L_z} \tag{1}$$

where L_x and L_z are the measured luminescence signals polarized in the x and z directions respectively. It has been observed (see Chapter 3) that the degree of polarization varies linearly with the applied stress:

$$\rho = K_\sigma(\sigma_{xx} - \sigma_{zz}) \tag{2}$$

Therefore, the value of ρ indicates the local stress $(\sigma_{xx} - \sigma_{zz})$ over the area from which the luminescence is being produced.

1.2 New Contributions

In the work reported in this thesis, polarization-resolved electroluminescence was used to measure stresses induced by bonding of GaAs SLD's to heat sinks [31,32], an important measurement for the semiconductor diode laser industry. The magnitude of the bonding stress was observed to depend mainly on the type of solder used, and the sign of the stress depended on the thermal expansion coefficient mismatch between the

diode and the heat sink. The bonding stress was observed to relax over time after bonding, with the rate of relaxation dependent upon the type of solder used and the heat sink temperature. The solder relaxation measurements are relevant to the interpretation of diode lifetest data, since observed changes in light output during a lifetest may be due to solder relaxation and not device aging. The coefficient K_σ for electroluminescence was experimentally determined for the AlGaAs diodes used in order to obtain quantitative stress information from the degree of polarization measurements.

A correlation between applied stress and degradation rate was observed in some devices but not others, suggesting that stress only enhances or accelerates the effect of other degradation-inducing defects such as dislocations. This is in agreement with current theories of stress-induced defect motion. The observation of enhanced degradation under stress, a confirmation of results reported by others, underlines the importance of the present research into stress measurement.

Polarization-resolved photoluminescence was used to measure stress distributions due to metallization, bonding, and ridge structures in diode lasers [33,34], with a stress resolution as low as 3×10^6 dyn/cm^2 and a spatial resolution of about 1 μm. To my knowledge, this is the first technique capable of measuring diode laser stresses with this combined resolution. The coefficient K_σ was determined for photoluminescence of GaAs and InP, and for GaAs was found to be the same as for the AlGaAs electroluminescence, within experimental error.

The resolution of polarization-resolved photoluminescence was demonstrated to be sufficient to detect and characterize (i.e., determine the Burgers vector and dislocation

direction of) individual dislocations penetrating the surface of a GaAs or InP crystal, or running near the surface as occurs for misfit dislocations in epitaxial layers [35,36]. The detection of misfit dislocations is of prime importance to those involved with epitaxial growth of strained layers or ternary or quaternary layers which may be excessively strained if the compositions are not carefully controlled. The detection of dislocations penetrating the surface of substrate material is important for quality control of the substrate material and the resulting manufactured devices. Many techniques currently in use for detecting dislocations, such as chemical etching, decoration, and transmission electron microscopy (TEM) [37], are destructive and therefore not suitable for routine screening of semiconductor wafers. To my knowledge, there are only two non-destructive techniques other than polarization-resolved photoluminescence currently available which are capable of detecting and characterizing individual dislocations, namely X-ray topography [38] and infrared birefringence [39,40]. Polarization-resolved photoluminescence provides a higher spatial resolution than either of these techniques. X-ray topography requires the use of a special X-ray source, and is very sensitive to external stresses and the condition of the sample surface. Infrared birefringence, while fast and simple, requires a sample about 1 mm thick with a polished rear surface and the dislocations running perpendicular to the surface. Polarization-resolved photoluminescence provides a simple and non-destructive technique of detecting and characterizing dislocations which has advantages over other available techniques.

1.3 Summary

In summary, the research performed for this thesis has provided some stress measurements of practical importance for the semiconductor diode laser industry, and has produced new practical techniques for measuring stresses and detecting and characterizing dislocations in semiconductor devices.

This thesis is divided into nine chapters, including this introductory chapter. Chapter 2 introduces the theory of the relationship between degree of polarization and stress, and gives a description of stress-enhanced aging. Chapter 3 describes the experimental apparatus and the experimental results of the electroluminescence measurements. Chapter 4 describes the apparatus and results of photoluminescence on the facets of diode lasers. Chapter 5 presents the calculations of stresses around dislocations, and the observed dislocation stresses. Chapter 6 outlines some of the future work which could be done using polarization-resolved photoluminescence and electroluminescence. Chapter 7 contains some concluding remarks, and Chapter 8 is an appendix containing one of the electronic circuits referred to in this thesis. Chapter 9 contains the cited references.

Chapter 2. Theory

2.1 Introduction

The measurements reported throughout this thesis are based on stress-induced changes in the degree of polarization of luminescence from III-V semiconductors. This thesis would be incomplete without some treatment of the mechanisms behind the effect. Therefore, this chapter deals with the theory of stress-induced changes in the degree of polarization. Stress-enhanced aging is also discussed. More specific aspects of theory, such as stress calculations, are dealt with in subsequent chapters as the need arises.

2.2 Band structure and polarization changes induced by stress

This section presents a simplified theory of the stress-induced degree of polarization of luminescence in III-V semiconductors, in order to provide the reader with sufficient background to understand the physical mechanisms behind polarization-resolved stress measurements. The theory is developed assuming conditions which are normally met during the present experiments, such as a sample temperature near room temperature, and applied stresses below about 2×10^9 dyn/cm^2. Only first-order effects, linear with stress, are considered. Many simplifying assumptions have been made, since the object of this section is more to provide a physical picture of the effects rather than

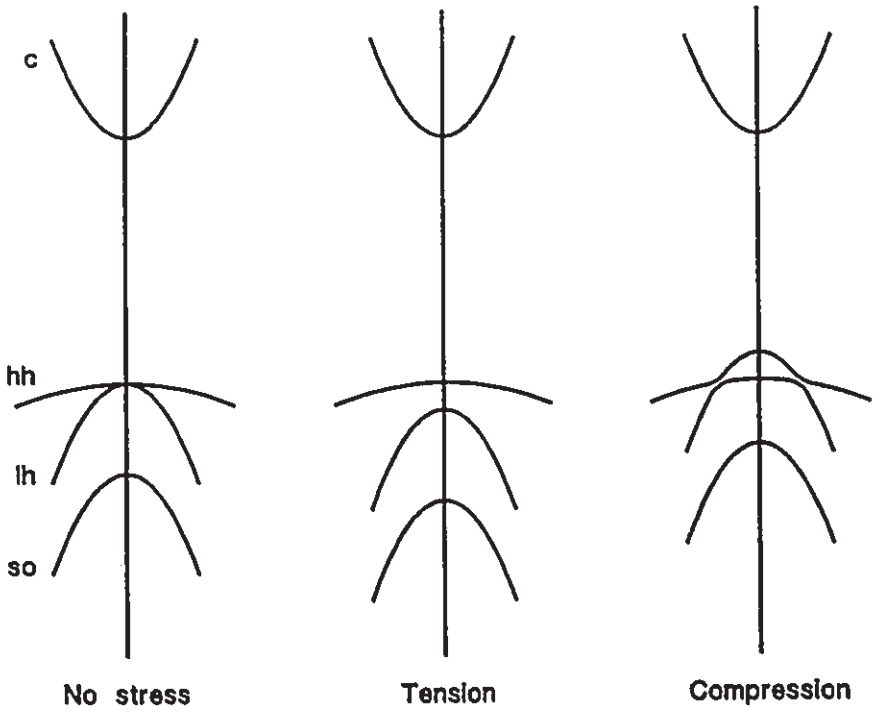

Figure 2.1 The band structure of GaAs or InP for the case of no applied stress, uniaxial tension, or uniaxial compression, for **k** along the stress direction.

to provide an accurate quantitative model.

The band structure of semiconductors is known to be affected by applied stress or strain. For a uniaxial applied stress, the effect is to reduce the crystal symmetry and cause a splitting between the heavy hole and light hole bands and deformations of the bands [41]. The band structure is illustrated in Fig. 2.1 for the case of no applied stress, uniaxial compression, and uniaxial tension, evaluated along the stress direction (the *z* axis). In Fig. 2.1, the labels *c*, *hh*, *lh*, and *so* refer to the conduction, heavy hole, light hole, and split-off bands respectively. Figure 2.2 illustrates the heavy hole and light hole band structure evaluated along the *x*, *y*, and *z* axes for various strain states, according to formulae presented by Pikus and Bir ([41], eqs. (14-17)) using the values

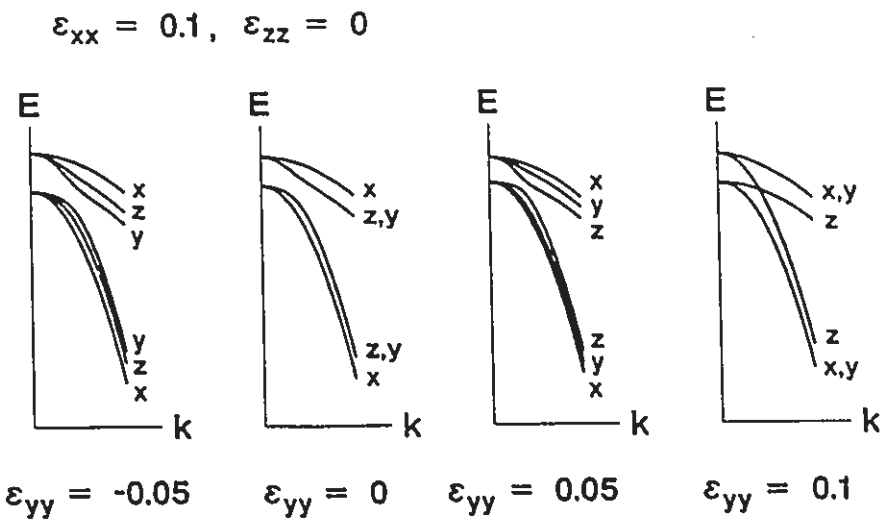

Figure 2.2 Shifts in the heavy hole and light hole bands of GaAs for various strain states, evaluated along the x, y, and z axes.

for GaAs of the band structure parameters [42] and deformation potentials [43]. The magnitudes of ϵ_{xx}, ϵ_{yy}, and ϵ_{zz} are in arbitrary units, since if the strains are scaled, appropriate scaling of the E and k axes will produce the same graphs. In an unstrained crystal, the E-k curves (electron energy E vs. wave vector magnitude k) are identical along the x, y, and z axes. The strain causes the heavy hole and light hole bands to deform, so that they are no longer identical along the x, y, and z directions. Note in Fig. 2.2 that away from k=0, the shift in the band energy along the y axis is proportional to ϵ_{yy}. If the energy shifts are small compared to kT, where kT represents Boltzmann's constant times the temperature in degrees Kelvin, most of the free carriers will occupy states away from the zone center k=0. (Boltzmann's constant will always be written in conjunction with the temperature, as kT, to avoid confusion with the electron wave vector magnitude k.) Far from the zone center, the direction-dependent components of the

energy shifts in the bands can be approximated by ([41], Eq. (31))

$$\begin{aligned} \delta E_h &= \pm \frac{3bB}{2\bar{B}} \sum_i \frac{k_i^2}{k^2} \epsilon_{ii} \\ &= \pm \frac{3bB}{2\bar{B}} \sum_i \cos^2\beta_i \epsilon_{ii} \end{aligned} \tag{3}$$

where

$$\begin{aligned} \bar{B} &= \sqrt{B^2 + C^2/5} \\ k &= \sqrt{k_x^2 + k_y^2 + k_z^2} \end{aligned} \tag{4}$$

and δE_h is the direction-dependent component of the energy shift, the plus and minus signs are for the heavy and light hole bands respectively, b is a deformation potential of the valence band, B and C are valence band parameters, the index i takes the values x, y, and z corresponding to the three coordinate axes, β_i is the angle between the electron momentum vector $\mathbf{k}$ and the axis i, and ϵ represents the strain tensor referred to its principal axes so that $\epsilon_{xy} = \epsilon_{yz} = \epsilon_{xz} = 0$. Other energy shifts occur which are independent of $\mathbf{k}$ or depend only on the magnitude of $\mathbf{k}$ and not its direction. These direction-independent energy shifts do not contribute to the degree of polarization of the luminescence, so they are ignored in this discussion. The band splitting corresponding to kT at room temperature (0.026 eV) occurs at an applied stress of about 4×10^9 dyn/cm^2 [44], well above most stresses of interest in this thesis, so the approximation of small energy shifts is valid. Note from Eq. (3) that for a given strain, the energy shift depends only on the direction of $\mathbf{k}$, not on the magnitude of $\mathbf{k}$.

The probability of interaction of a photon with the semiconductor is evaluated

using the optical matrix element,

$$|M|^2 = \frac{1}{|\mathbf{e}|^2} \sum_{\psi_1} \sum_{\psi_2} | <\psi_1|\mathbf{e}\cdot\mathbf{p}|\psi_2> |^2 \tag{5}$$

where ψ_1 and ψ_2 are the final and initial states, $\mathbf{p}$ is the electron momentum operator, $\mathbf{e}$ is the polarization vector of the incident radiation, and $\mathbf{e}\cdot\mathbf{p} = e_x p_x + e_y p_y + e_z p_z$. The wave functions for the conduction, heavy hole, light hole, and split-off bands, for quantization along the z axis (i.e., $\mathbf{k}$ along the z axis, one of the crystal axes) are given by [45]

$$\begin{aligned}
\psi_c &= S\uparrow, \quad S\downarrow \\
\psi_{hh} &= (X+iY)\uparrow/\sqrt{2}, \quad (X-iY)\downarrow/\sqrt{2} \\
\psi_{lh} &= (2Z\uparrow - (X+iY)\downarrow)/\sqrt{6}, \quad (2Z\downarrow + (X-iY)\uparrow)/\sqrt{6} \\
\psi_{so} &= -(Z\uparrow + (X+iY)\downarrow)/\sqrt{3}, \quad -(Z\downarrow - (X-iY)\uparrow)/\sqrt{3}
\end{aligned} \tag{6}$$

where X, Y, and Z contain the symmetry of the p_x, p_y, and p_z orbitals respectively, S is an s-like wave function, and the up and down arrows represent the spin up and spin down states respectively. The only non-zero components of the optical matrix element are

$$\begin{aligned}
&<X\uparrow|p_x|S\uparrow> = <Y\uparrow|p_y|S\uparrow> = <Z\uparrow|p_z|S\uparrow> \\
&= <X\downarrow|p_x|S\downarrow> = <Y\downarrow|p_y|S\downarrow> = <Z\downarrow|p_z|S\downarrow> = \frac{m_0}{\hbar}P
\end{aligned} \tag{7}$$

Normally, the split-off band is well below the heavy hole and light hole bands, so its hole density is negligible and interactions with the split-off band can be ignored. For an arbitrary direction of electric field, the matrix elements for transitions between the

conduction band and the light and heavy hole bands can be written as [46]

$$|M'_{hh}|^2 = 1-\cos^2\alpha$$
$$|M'_{lh}|^2 = 1/3+\cos^2\alpha \tag{8}$$

where $|M'|^2 = |M|^2(\hbar/m_0P)^2$ is a normalized matrix element, P is the momentum matrix element as originally defined by Kane [45], and α is the angle between the electric field vector **e** and the electron momentum vector **k**. Equation (8) is readily derived from Eqs. (5)-(7) for the case of **k** parallel to the z direction. For arbitrary directions of **k**, the basis functions of the bands are no longer given by Eq. (6), but become more complicated due to a rotation of the basis functions [45]. However, Eq. (8) can also be shown to apply when **k** is in an arbitratry direction [46]. The matrix elements represent the probability of interaction for a single electron. The total emission intensity from each valence band into a given polarization will be proportional to the integral of the hole density times the electron density and the matrix element, over all possible **k** values,

$$L = A\int |M|^2(\theta,\phi)f_e(E_e(r))f_h(E_h(r)+\delta E_h(\theta,\phi))r^2\sin\phi\,dr\,d\theta\,d\phi \tag{9}$$

where $f_e(E_e)$ and $f_h(E_h)$ are the distributions of electrons and holes as a function of energy,

$$f_e(E_e) = \frac{1}{\exp[(E_e-E_{fe})/kT]+1}$$
$$f_h(E_h) = \frac{1}{\exp[(E_{fh}-E_h)/kT]+1} \tag{10}$$

$E_e(r)$ and $E_h(r)$ are the electron and hole energies with the assumption of spherical constant energy surfaces for zero applied strain, E_{fe} and E_{fh} are the electron and hole

quasi-Fermi levels, δE_h is the strain-induced shift in the hole energy, A is a normalizing constant, and r, θ, and ϕ represent the k vector in polar coordinates. If $E_{fh}-E_h \gg kT$, i.e., the material is not heavily p-doped or under high excitation, then

$$f_h(E_h) \approx \exp\left[\frac{E_h-E_{fh}}{kT}\right] \tag{11}$$

and $f_h(E_h+\delta E_h) \approx f_h(E_h)\,(1+\delta E_h/kT)$. The integral of Eq. (9) can then be separated into radial and angular components,

$$\begin{aligned} L &= A \int f_e(E_e(r)) f_h(E_h(r))\, r^2 dr \int |M|^2(\theta,\phi) \left[1+\frac{\delta E_h(\theta,\phi)}{kT}\right] d\Omega \\ &= G \int |M'|^2(\theta,\phi) \left[1+\frac{\delta E_h(\theta,\phi)}{kT}\right] d\Omega \end{aligned} \tag{12}$$

where

$$G = \frac{A P^2 m_0^2}{\hbar^2} \int f_e(E_e(r)) f_h(E_h(r))\, r^2 dr \tag{13}$$

and $d\Omega = \sin\phi\; d\theta\; d\phi$ represents an element of solid angle. The integral of Eq. (12) must be performed for the light and heavy hole bands, with δE_h evaluated for each band using Eq. (3), and the results summed to obtain the total luminescence.

For the case of a uniaxial strain $\epsilon = \epsilon_{xx}$ along the x axis, Eq. (3) consists of only one term with $i = x$. If the polarization direction is parallel to the strain direction, $\beta_x = \alpha$. Substituting for $|M'|^2$ and δE_h, the luminescences from the heavy holes and light holes respectively are given by

$$L_{hh\parallel} = G_{hh}\int (1-\cos^2\alpha)\left(1+\frac{3bB\epsilon}{2\overline{B}kT}\cos^2\alpha\right)d\Omega$$
$$L_{lh\parallel} = G_{lh}\int \left(\frac{1}{3}+\cos^2\alpha\right)\left(1-\frac{3bB\epsilon}{2\overline{B}kT}\cos^2\alpha\right)d\Omega \qquad (14)$$

For a strain $\epsilon = \epsilon_{yy}$ applied along the y axis, perpendicular to the polarization direction, and dropping the subscript on β,

$$L_{hh\perp} = G_{hh}\int (1-\cos^2\alpha)\left(1+\frac{3bB\epsilon}{2\overline{B}kT}\cos^2\beta\right)d\Omega$$
$$L_{lh\perp} = G_{lh}\int \left(\frac{1}{3}+\cos^2\alpha\right)\left(1-\frac{3bB\epsilon}{2\overline{B}kT}\cos^2\beta\right)d\Omega \qquad (15)$$

Note that Eqs. (14) and (15) apply for any directions of strain and polarization provided that the two directions are parallel in Eq. (14) and perpendicular in Eq. (15). For a uniaxial strain in the x direction, and with the degree of polarization defined as in Eq. (1), the degree of polarization is given by

$$\rho = \frac{L_\parallel - L_\perp}{L_\parallel + L_\perp} \qquad (16)$$

where

$$L_\parallel - L_\perp = L_{hh\parallel} + L_{lh\parallel} - L_{hh\perp} - L_{lh\perp}$$
$$= -\frac{3bB\epsilon_{xx}}{2\overline{B}kT}(G_{hh}+G_{lh})\int (\cos^4\alpha - \cos^2\alpha\cos^2\beta)\,d\Omega \qquad (17)$$

Note that in Eq. (17), β represents the angle between $\mathbf{k}$ and the perpendicular polarization direction; the angle between $\mathbf{k}$ and the parallel polarization direction is equal to α. To simplify the integral in Eq. (17), the angle γ is introduced as the angle between

k and a vector c perpendicular to both the stress direction and the perpendicular polarization direction. Since the stress direction, the polarization direction, and c are mutually perpendicular, we have $\cos^2\alpha + \cos^2\beta + \cos^2\gamma = 1$. Because of symmetry,

$$\begin{aligned}\int \cos^2\alpha\cos^2\beta\, d\Omega &= \int \cos^2\alpha\cos^2\gamma\, d\Omega \\ &= \int \cos^2\alpha(1-\cos^2\alpha-\cos^2\beta)\, d\Omega \\ &= \int (\cos^2\alpha-\cos^4\alpha-\cos^2\alpha\cos^2\beta)\, d\Omega\end{aligned} \tag{18}$$

and therefore

$$\int \cos^2\alpha\cos^2\beta\, d\Omega = \frac{1}{2}\int (\cos^2\alpha-\cos^4\alpha)\, d\Omega \tag{19}$$

which can be used to simplify Eq. (17) to

$$\begin{aligned}L_\parallel - L_\perp &= -\frac{3bB\epsilon_{xx}}{2\overline{B}kT}(G_{hh}+G_{lh})\int\left[\frac{3}{2}\cos^4\alpha-\frac{1}{2}\cos^2\alpha\right]d\Omega \\ &= -\frac{3bB\epsilon_{xx}}{2\overline{B}kT}(G_{hh}+G_{lh})\left[\frac{3}{2}\left[\frac{4\pi}{5}\right]-\frac{1}{2}\left[\frac{4\pi}{3}\right]\right] \\ &= -\frac{4\pi bB\epsilon_{xx}}{5\overline{B}kT}(G_{hh}+G_{lh})\end{aligned} \tag{20}$$

Evaluating the denominator of Eq. (16) for the case $3bB\epsilon_{xx}/2\overline{B}kT \ll 1$,

$$\begin{aligned}L_\parallel + L_\perp &= L_{hh\parallel} + L_{lh\parallel} + L_{hh\perp} + L_{lh\perp} \\ &\approx 2\int\left[G_{hh}(1-\cos^2\alpha)+G_{lh}\left[\frac{1}{3}+\cos^2\alpha\right]\right]d\Omega \\ &= \frac{16\pi}{3}(G_{hh}+G_{lh})\end{aligned} \tag{21}$$

which gives

$$\rho = -\frac{3bB\epsilon_{xx}}{20\overline{B}kT} \tag{22}$$

If the strain is applied along the z direction, ρ is given by

$$\rho = \frac{3bB\epsilon_{zz}}{20\overline{B}kT} \tag{23}$$

and for a combination of strains in the x and z directions,

$$\rho = -\frac{3bB}{20\overline{B}kT}(\epsilon_{xx}-\epsilon_{zz}) \tag{24}$$

Strain in the direction of light propagation (ϵ_{yy}) does not affect ρ in isotropic materials. Using the stress-strain relationship for an isotropic material ([47], p. 203), ρ can be written as a function of stress instead of strain,

$$\begin{aligned}\rho &= -\frac{3bB(1+\nu)}{20E\overline{B}kT}(\sigma_{xx}-\sigma_{zz}) \\ &= K_\sigma(\sigma_{xx}-\sigma_{zz})\end{aligned} \tag{25}$$

in agreement with Eq. (2), where E is Young's modulus and ν is Posson's ratio. Using the known values for GaAs of $b = -2.0$ eV [43], $B = -4.4$, $|C| = 6.2$ [42], and $E/(1+\nu) = c_{11} - c_{12} = 6.5\times10^{11}$ dyn/cm^2 [48], and $kT = 0.026$ eV at room temperature, the theoretical value of K_σ is given by

$$K_\sigma = -\frac{3bB(1+\nu)}{20E\overline{B}kT} = -1.5\times10^{-11}\ \text{cm}^2/\text{dyn} \tag{26}$$

which is at least of the same order of magnitude as the experimental value of

-5.1×10^{-11} cm^2/dyn measured in Chapter 4.

Taking into account the non-spherical valence band constant energy surfaces and band mixing under stress will introduce modifications to K_{zz}, including nonlinearities at high stress, and anisotropy. The additional complications of including these effects in the calculation of K_o are beyond the scope of this thesis; interested readers are referred to the work of Kane [45], Pollak and Cordona [44], Luttinger and Hohn [49], and Ahn and Chuang [50].

The degree of polarization is proportional to the applied stress (or strain) for sufficiently small applied stress, so that the stress or strain may be determined from a measurement of the degree of polarization ρ. Usually stresses are easier to determine experimentally, so throughout this thesis, calculations are performed using stresses. Under tensile stress, a hole has a lower probability of interaction with a photon polarized in the stress direction, so a tensile stress σ_{xx} decreases the proportion of stimulated or spontaneous emission polarized in the x direction and hence decreases the value of ρ for the emitted light. Similarly, a tensile stress σ_{zz} increases ρ. Often it is known that $\sigma_{zz} = 0$, so in that case it is convenient to refer to the dependence of ρ on σ_{xx} only. I have observed experimentally that the degree of polarization is proportional to the applied stress for stresses up to at least 10^9 dyn/cm^2.

For GaAs, the effect of stress on electron-photon interactions is only slightly dependent upon the orientation of the stress with respect to the crystal axes [44]. The assumption of isotropy should therefore be reasonable in most cases. However, there will likely be occasions when the isotropic assumption is not adequate. The next section

discusses the treatment of anisotropy in K_o in cubic semiconductors such as GaAs and InP.

2.3 The tensor nature of luminescence

III-V semiconductors such as GaAs and InP are not isotropic in elasticity or photoelasticity, so it is expected that they are not isotropic in the response of ρ to stress. This section discusses the possibility of representing the polarization of the luminescence in terms of a tensor. To my knowledge, the polarization state of luminescence has not been previously described using tensors. However, this representation would be very useful for performing calculations of stress-induced degree of polarization for arbitrary stresses and crystal orientations in anisotropic materials such as semiconductor crystals. The tensor representation of luminescence is not an exact relationship in birefringent materials, but it is shown to be sufficiently accurate for practical purposes for calculating the stress-induced degree of polarization in cubic crystals. Although the tensor nature of stress-induced degree of polarization has not yet been demonstrated experimentally, this section shows that the tensor nature is expected from thermodynamic and phenomenological arguments.

If two vectors, such as electric field **E** and current **J**, are linearly related to one another, the relationship may be expressed as

$$\mathbf{J} = \sigma\mathbf{E} \tag{27}$$

where σ is the electrical conductivity. If **J** and **E** are always parallel, then σ is a single

constant, a scalar. In general, however, the vectors J and E are not always parallel. An applied field E_x may induce current components J_y and J_z as well as J_x. The conductivity σ is then a second-rank tensor with nine components specifying the dependence of J_x, J_y, and J_z on E_x, E_y, and E_z. The relationship between J and E is then written as

$$J_i = \sigma_{ij} E_j \tag{28}$$

where i and j take the values 1, 2, or 3 (representing x, y, and z respectively), and summation over repeated indices is assumed. Thus, Eq. (28) represents three equations, each with three terms on the right hand side. Stress σ and strain ϵ are also second-rank tensors, and are related to each other by the fourth-rank tensor of elastic stiffness c,

$$\sigma_{ij} = c_{ijkl} \epsilon_{kl} \tag{29}$$

If the coordinate system is changed by rotations of the primary axes, the new coordinates (x_1', x_2', x_3') can be obtained from the old coordinates (x_1, x_2, x_3) using the direction cosines α_{ij},

$$x'_i = \alpha_{ij} x_j \tag{30}$$

Note that the direction cosines α_{ij} do not form a tensor, although Eq. (30) resembles Eq. (28). A vector such as E or J will also transform according to Eq. (30). The values of a second-rank tensor such as σ will transform according to

$$\sigma'_{ij} = \alpha_{ik} \alpha_{jl} \sigma_{kl} \tag{31}$$

and a fourth-rank tensor such as c will transform according to

$$c'_{ijkl} = \alpha_{im}\alpha'_{jn}\alpha_{ko}\alpha_{lp}c_{mnop} \tag{32}$$

Note that Eq. (32) represents 81 equations, each with 81 terms, for a total of 6561 multiplications and additions required to perform the transformation. If it is required to evaluate an equation such as (29) for a rotated coordinate system, it is often easier to transform ϵ to the original coordinates, evaluate Eq. (29), and transform σ back to the rotated coordinate system, rather than transform c to the rotated coordinate system.

The transformation rules of Eqs. (30)-(32) apply to all tensor quantities of the appropriate rank, and enable calculations of tensor relationships to be performed for arbitrary choices of primary axes. Most crystals are symmetric about several planes and axes, which reduces the number of independent coefficients in their tensor properties. The use of tensor transformation rules then allows the calculation of tensor relationships to be done for any crystal orientation after experimental calibration of the relationships in only a few crystal orientations. The relationship between stress and the degree of polarization is expected to be anisotropic for semiconductor crystals such as GaAs and InP, since related properties such as elasticity and photoelasticity are anisotropic for these materials. It would be desirable to be able to apply tensor transformation rules to stress-induced degree of polarization calculations, since the crystal orientation of a given sample may not always be the same as that for which the calibration experiments were performed. To do this, it is necessary to determine how tensor relationships may be applicable to calculation of stress-induced degree of polarization.

It is known that the real and imaginary parts of the dielectric constant, $\epsilon' = (n^2-k^2)$ and $\epsilon'' = 2nk$ respectively, transform as second-rank tensors [51]. Here n and

k are the real and imaginary parts of the refractive index. These terms can be expanded as

$$\begin{aligned} \epsilon_0' + \delta\epsilon' &= n_0^2 + 2n_0\delta n + \delta n^2 - k_0^2 - 2k_0\delta k - \delta k^2 \\ \epsilon_0'' + \delta\epsilon'' &= 2n_0k_0 + 2n_0\delta k + 2\delta n k_0 + 2\delta n\delta k \end{aligned} \tag{33}$$

where ϵ_0', ϵ_0'', n_0, and k_0 are the (isotropic) values of ϵ', ϵ'', n, and k for zero applied stress, and $\delta\epsilon'$, $\delta\epsilon''$, δn, and δk are the stress-induced variations of the respective values. The terms $\delta\epsilon'$ and $\delta\epsilon''$ transform as tensors since ϵ' and ϵ'' are known to be tensors.

It can be shown, by equating absorption and spontaneous emission at thermal equilibrium, that the expected emission intensity is related to k by ([52], p. 109),

$$R = Un^2k \tag{34}$$

where R is the number of radiative recombinations per unit volume at thermal equilibrium, and $U = 32\pi^2\nu^3/c^3(\exp(h\nu/kT)-1)$ is independent of the material. Although Eq. (34) was developed to relate the spectral dependence of the emission to the spectral dependence of k, it also must relate the directional dependence of the luminescence to the directional dependence of k. This is because the incident flux of thermal radiation is equal in all directions. If there is a difference in k (and hence a difference in the absorbed thermal radiation) between two directions, there must be a corresponding difference in the spontaneous emission in the two directions in order for thermal equilibrium to be maintained. For nonequilibrium conditions in which free carriers are being generated in the semiconductor, there can be no distinction between free carriers which have been generated by thermal radiation and free carriers generated by other

types of external excitation. Therefore, at low excitation levels, the spectral dependence and the directional dependence of the luminescence are expected to be the same for thermal equilibrium and nonequilibrium conditions. The radiative recombination rate at nonequilibrium can be written as AR, where $A>1$ is a factor indicating the increase in the recombination rate over thermal equilibrium conditions.

To a good approximation, the external luminescence intensity L (photons per unit solid angle per second) outside the planar surface of the material is related to the internal radiative recombination rate AR by [53]

$$L = \frac{ARV\cos\theta}{\pi n(n+1)^2} \tag{35}$$

where V is the volume of luminescent material. Self-absorption in the material can be ignored if the absorption length at the pump wavelength (and hence the distance through which the emitted light has to travel in the material) is much smaller than that at the emission wavelength. Assuming normal incidence ($\theta=0$), the external luminescence intensity is given by

$$\begin{aligned} L &= \frac{AVUnk}{\pi(n+1)^2} \\ &= \frac{AVU(n_0k_0+\delta(nk))}{\pi(n_0+1)^2}\left[1-\frac{2\delta n}{n_0+1}+\cdots\right] \\ &= \frac{AVU}{\pi(n_0+1)^2}\left[n_0k_0+\delta(nk)-\frac{2n_0k_0\delta n}{n_0+1}+\cdots\right] \end{aligned} \tag{36}$$

where $\delta n/n_0 \ll 1$ is assumed so that terms of higher order of $\delta n/n_0$ can be ignored. The

assumption $\delta n/n_0 \ll 1$ is met at sufficiently low applied stress in cubic crystals such as GaAs and InP, which are not birefringent at zero stress. The quantity $\epsilon'' = 2nk$ is known to transform as a tensor, so L will also transform as a tensor if δn can be shown to transform as a tensor. Evaluating the quantity

$$\delta\epsilon' + \frac{k_0}{n_0}\delta\epsilon'' = 2\left(n_0 + \frac{k_0^2}{n_0}\right)\delta n + 2\delta n\delta k + \delta n^2 - \delta k^2 \tag{37}$$

it is seen that the left hand side of Eq. (37) is a tensor quantity (the sum of two tensor quantities), and the right hand side is proportional to δn, to first order in δn and δk. Therefore, δn can be treated as a tensor quantity for sufficiently small applied stress, and hence the approximation that L transforms as a tensor is as good as the approximation $\delta n/n_0 \ll 1$. For an applied stress of 10^9 dyn/cm^2 in GaAs, $\delta n/n_0 \approx 0.002/3.5 = 0.0006$ [20], so this approximation is excellent. This means that calculations of δL made using tensor relationships will be accurate to better than 0.1 percent. It is therefore a good approximation to assume that the luminescence intensity L can be represented as a tensor in cubic crystals such as GaAs, with low applied stress.

The representation quadric for the tensor L is an ellipsoid, similar to the index ellipsoid for refractive index, with the radius of the ellipsoid in any direction representing $1/\sqrt{L}$ for light polarized in that direction. The luminescence intensity is the same for light polarized in a given direction but emitted in any direction perpendicular to the polarization vector. It can be shown that this is true for radiation from a classical oscillating dipole. Moreover, the directional dependence of dipole radiation satisfies tensor transformation rules, supporting the validity of the tensor representation of

luminescence.

It is convenient to break the tensor L into two components,

$$L_{ij} = L_0 + \delta L_{ij} \tag{38}$$

where L_0 is the isotropic luminescence intensity in the unstrained material, and δL_{ij} includes the stress-induced variations in luminescence intensity. Assuming a linear relationship between $\delta L/L_0$ and stress σ, a fourth-rank tensor K can be defined which relates δL and σ according to

$$\frac{\delta L_{ij}}{2L_0} = K_{ijkl}\sigma_{kl} \tag{39}$$

where i, j, k, and l assume the values 1, 2, or 3, corresponding to the three coordinate axes, and the factor of 2 has been added to simplify degree of polarization calculations, as will be seen later. Summation over repeated indices is assumed. Equation (39) represents nine equations (one for each coefficient of δL), each with nine terms. The tensors δL and σ are symmetric, so they each have only six independent coefficients. For this reason, an abbreviated matrix notation is often used, with the following index substitutions:

$$\begin{aligned} 11 &\rightarrow 1 \\ 22 &\rightarrow 2 \\ 33 &\rightarrow 3 \\ 23,32 &\rightarrow 4 \\ 31,13 &\rightarrow 5 \\ 12,21 &\rightarrow 6 \end{aligned} \tag{40}$$

In the abbreviated notation, Eq. (39) becomes

$$\frac{\delta L_m}{2L_0} = K_{mn}\sigma_n \tag{41}$$

However, note that in order for Eq. (41) to be equivalent to Eq. (39), the relationship between K_{ijkl} and K_{mn} must be assigned according to

$$\begin{aligned} K_{ijkl} &= K_{mn} \qquad \text{if } n = 1,2,3 \\ K_{ijkl} &= \frac{K_{mn}}{2} \qquad \text{if } n = 4,5,6 \end{aligned} \tag{42}$$

For the cubic symmetry T_d ($\bar{4}3m$) of zincblende type semiconductors such as GaAs and InP, there are three independent constants in the tensor K, analogous to the three independent constants of the photoelastic tensor relating stress and refractive index [54]. The tensor K for cubic crystals can be written in the abbreviated notation as

$$K = \begin{pmatrix} K_{11} & K_{12} & K_{12} & 0 & 0 & 0 \\ K_{12} & K_{11} & K_{12} & 0 & 0 & 0 \\ K_{12} & K_{12} & K_{11} & 0 & 0 & 0 \\ 0 & 0 & 0 & K_{44} & 0 & 0 \\ 0 & 0 & 0 & 0 & K_{44} & 0 \\ 0 & 0 & 0 & 0 & 0 & K_{44} \end{pmatrix} \tag{43}$$

where K_{11}, K_{12}, and K_{44} are the three independent coefficients of K. As an example, suppose the analyzing axes x and z of the polarizing beamsplitter are along the x_1 and x_3 axes ([100] and [001] crystal directions) of the semiconductor crystal lattice. An equivalent crystal orientation occurs in Chapter 5 for a 45° sample orientation. In this

case, the degree of polarization is given by

$$\rho = \frac{L_x - L_z}{L_x + L_z} \approx \frac{\delta L_1 - \delta L_3}{2L_0} = (\sigma_x - \sigma_z)(K_{11} - K_{12}) \tag{44}$$

where it has been assumed that $\delta L \ll L_0$. Comparing Eq. (44) with Eq. (2), it is seen that the constant K_a is given by $K_a = K_{11} - K_{12}$ for this crystal orientation. If the analyzing axes do not coincide with the crystal axes, it is necessary to transform the stress tensor to the crystal axes, calculate δL using Eq. (39) (or Eq. (41)), transform δL back to the analyzing axes, and calculate ρ. Note that the transformations must be performed on the full tensors, not using the abbreviated notation. These calculations were performed using Maple [55], a symbolic computation program, on a personal computer. For the case of x and z aligned in the [110] and [1$\bar{1}$0] directions, which is equivalent to the case of a 0° sample orientation in Chapter 5, the degree of polarization is given by

$$\rho = (\sigma_x - \sigma_z) K_{44} \tag{45}$$

In this case, $K_a = K_{44}$. For the case of x and z aligned in the [110] and [001] crystal directions respectively, which is the case for the measurements on diode laser facets performed in Chapters 3 and 4, the calculation yields

$$\rho = \sigma_x \frac{K_{11} - K_{12} + K_{44}}{2} + \sigma_y \frac{K_{11} - K_{12} - K_{44}}{2} - \sigma_z (K_{11} - K_{12}) \tag{46}$$

For this crystal orientation, the relationship between σ and ρ cannot be reduced to the form of Eq. (2) due to the different coefficients mulitplying σ_x and σ_z. This is because

the x and z axes do not represent equivalent crystal directions. By equating the coefficients multiplying σ_x and σ_z in Eq. (46), it can be seen that the condition for isotropy is $K_{11}-K_{12} = K_{44}$. There is a term in Eq. (46) involving σ_y; however, at the free surface ($y=0$), the boundary condition is $\sigma_{yy} = \sigma_{xy} = \sigma_{yz} = 0$, so that the term containing σ_y does not normally contribute to ρ. In the beam-bending calibration experiments reported in Chapters 3 and 4, only σ_x is present, so in that case the value $K_{\sigma av} = (K_{11}-K_{12}+K_{44})/2$ has been experimentally determined.

For arbitrary crystal orientations, it is observed from the Maple calculations that when the degree of polarization is calculated, only two independent constants occur in the resulting expressions, namely $(K_{11}-K_{12})$ and K_{44}. If a uniaxial stress σ_x is applied along one of the analyzing axes, the extreme values of the proportionality constant relating ρ and σ_x are $(K_{11}-K_{12})$, for the case of [100] stress and analyzing along [100] and [010] (or [100] and [011]), and K_{44} for the case of [110] stress and analyzing along [110] and $[1\bar{1}0]$. For all other crystal orientations and stress directions, the proportionality constant is between those two extremes. It is noted that the value $K_{\sigma av}$ measured in the beam-bending calibration experiments represents the average of the extremes of K_σ, so it is reasonable to use the measured value of $K_{\sigma av}$ for all crystal directions when only one measurement has been performed. Two calibration experiments with stresses and analyzing axes in different crystal directions are required to determine the two constants $(K_{11}-K_{12})$ and K_{44} independently. Once these two constants are known, the degree of polarization can be calculated for any crystal orientation and any applied stress or strain. The tensor representation of luminescence is therefore useful for relating

degree of polarization measurements to stresses when the sample crystal orientation is different from the crystal orientations of the calibration experiments.

Equations (44)-(46) could be written in terms of strain ϵ instead of stress σ, with a different tensor K_{ϵ}. Usually stresses are easier to determine experimentally, so I will make reference only to the effects of stress on ρ.

If the approximation $\delta n/n_0 \ll 1$ is not met, for example in a material which is initially birefringent or at high applied stress, it will be necessary to determine the coefficients of the real and imaginary components of the complex dielectric constant ϵ' and ϵ'', and the two fourth-rank tensors relating ϵ' and ϵ'' with the stress σ. To calculate the degree of polarization for a given stress, it will be necessary to calculate ϵ' and ϵ'' along each analyzing axis using tensor relationships, then determine n and k from ϵ' and ϵ'' and use the first line of Eq. (36) to calculate the luminescence intensity.

2.4 Stress-enhanced aging

It is known that the motion of dislocations and other defects is enhanced under the presence of free-carrier recombination [56]. This effect is called recombination enhanced defect motion (REDM). REDM occurs under current injection, laser illumination, or electron beam irradiation, all of which inject minority carriers into the semiconductor. REDM can be an important degradation mechanism occurring in diode lasers and similar devices, since they operate under conditions of high current injection. The REDM mechanism can be explained by assuming that an energy level occurs in the

band gap due to the defect, and that this energy level causes an injected minority carrier to be captured by the defect. The energy released in the subsequent nonradiative recombination of the carrier is transferred to the lattice in the neighborhood of the defect, with a certain probability of stimulating a vibrational mode which causes defect motion. These assumptions lead to an expression for the defect velocity which fits the form of the experimental observations for dislocations [56],

$$V = V_{th0}\exp(-E_{th}/kT) + V_{r0}\left[\frac{I}{I_0}\right]\exp[-(E_{th}-\delta E)/kT] \tag{47}$$

where the first term represents the dislocation velocity in the absence of carrier injection, and the second term represents the enhancement of dislocation velocity in the presence of carrier injection I. E_{th} is an activation energy for the dislocation motion, and δE represents the reduction in activation energy due to the presence of minority carriers.

It is important to recognize that in order for dislocations to move through a crystal, a stress must be present to cause the dislocation motion to be energetically

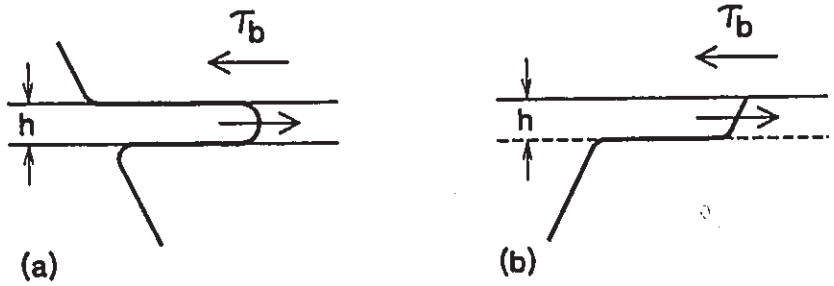

Figure 2.3 A back stress τ_b tends to oppose dislocation motion. This is illustrated for (a) a strained heterostructure active layer, and (b) the stressed region under a ridge or oxide stripe.

favorable. The stress dependence of the dislocation velocity often exhibits a threshold effect, which can be explained by a 'back stress' τ_b due to the dislocation line tension. There is an effective tension along the dislocation which tends to oppose dislocation motion, as illustrated in Fig. 2.3 for a strained heterostructure active layer and the stressed region under an oxide window. Thus, recombination enhanced dislocation motion will be suppressed at stresses below $\tau_b \approx bG/h$ [56], where b is the magnitude of the dislocation Burgers vector, G is the shear modulus, and h is the layer thickness. Therefore, it is important to reduce the internal stresses in diode lasers in order to prevent dislocation motion leading to device degradation.

2.5 Summary

This chapter has discussed the background information required to interpret measurements of stress-induced degree of polarization and understand stress-enhanced degradation. In the following chapters, the experimental results are presented and discussed.

Chapter 3. Electroluminescence Measurements

3.1 Introduction

When observing electroluminescence in planar structures such as diode lasers, it is customary to refer to the two polarization directions as TE (transverse electric) and TM (transverse magnetic). These names refer to the orientation of the electric and magnetic fields with respect to the plane of the diode active region. When the diode is mounted horizontally, the TE and TM polarizations correspond to the x and z polarizations respectively of previous chapters, and L_{TE} and L_{TM} refer to the intensities of the emitted light in the respective polarizations.

Near and above threshold in a diode laser, stimulated emission amplifies the difference in gain (or loss) between the TE and TM polarizations, causing most of the emission to be in one polarization. The major factor affecting round-trip gain is the higher facet reflectivity for the TE polarization, which normally causes a diode laser to lase in the TE polarization [57]. Well below threshold, however, stimulated emission is negligible, and ρ is a sensitive function of the stress in the active region. The emitted light is produced along the entire length of the active region, so the stress measurement represents an average stress along the active region, weighted toward the facet being observed. In comparison with other techniques such as Raman spectroscopy or X-ray diffraction, measuring the degree of polarization of the emitted light is very fast and

simple, making the technique practical as a quality assurance tool in a production environment.

In this chapter, measurements of stress induced by bonding AlGaAs superluminescent diodes to Cu, SiC, and diamond heat sinks with Pb-Sn (40% Pb-60% Sn by weight) and Au-Sn (80% Au-20% Sn by weight) solders are reported. The change in ρ per unit applied stress was determined experimentally, then bonding stresses were determined by measuring ρ before and after bonding. The relaxation of the bonding stress was characterized as a function of time and temperature for each solder. Experiments demonstrating stress-enhanced degradation are reported. Polarization-resolved electroluminescence is applicable to AlGaAs and InGaAsP diode lasers as well as superluminescent diodes.

3.2 Experimental Technique

The measurements reported here were made on AlGaAs 830 nm superluminescent diodes. These devices are 500 μm long and have a planar active region and a current-blocking oxide with a 4 μm wide window [58]. This structure is similar to that of a gain-guided diode laser [59], but the active region is angled 5 degrees from perpendicular to the facets, and both facets have an anti-reflection coating to reduce optical feedback and inhibit lasing.

The experimental setup is shown in Fig. 3.1. The emitted light from the devices was collimated by a 20× microscope objective and put through a polarizing beamsplitter

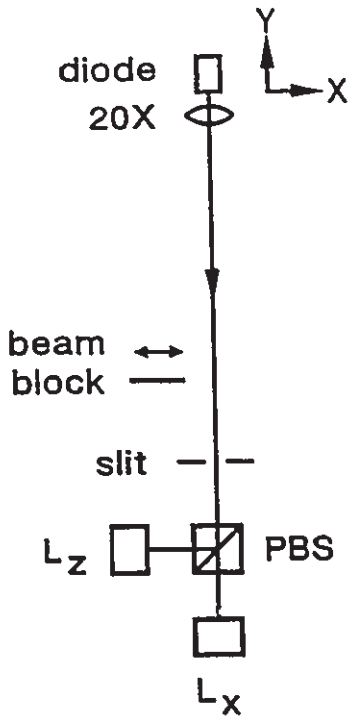

Figure 3.1 The experimental setup for polarization-resolved electroluminescence.

cube (PBS) to separate the TE and TM polarizations. The microscope objective was mounted on an x-y-z translation stage to enable focussing. The TE and TM signals were detected using two large-area (5 mm diameter) Si p-i-n photodiodes (L_x, L_z). The device current was modulated at 1 kHz with a 50% duty cycle, and the detected signals were analyzed using phase-sensitive detectors. Current heating of the active region was not considered significant because of the low current level used (5 mA). The beam block, operated under computer control, was used to obtain the zero-light signal readings, to eliminate the offsets in the phase sensitive detectors (PSD's) and analog-to-digital converters (ADC's). The slit was placed in the setup only when performing high-resolution imaging of the active layer stresses (discussed in Section 3.5).

The degree of polarization ρ could be measured reproducibly within ± 0.0004, based on repeated measurements of a single device with repositioning of the device on the apparatus between each measurement. This corresponds to a resolution of applied stress of about 10^7 dyn/cm^2, or a strain of about 10^{-5}, for the superluminescent diodes based on the observed relationship between stress and ρ (Section 3.3). To obtain this reproducibility, several steps were taken. The two detectors were positioned such that their images through the beamsplitter aligned within 10 μm, by adjusting the detector positions until a small displacement of the collimating objective caused a minimal change in ρ [60]. The splitting ratio of the polarizing beamsplitter varies slightly with the angle of incidence of the radiation, which will change if the diode position changes. The position of the diode was measured within 10 μm by measuring the position of the collimating objective at maximum TE signal, and the value of ρ was corrected if the diode position changed between readings (i.e., if the diode had been removed from the apparatus and replaced). Measurements of ρ were taken for several values of applied force on the probe (upper electrical contact), and the readings were extrapolated to zero applied force. The value of ρ varies with current, so all readings were taken at the same current level within 0.1 mA. A thermoelectric heater/cooler and a precision thermistor were used to keep the device at a constant temperature within 0.1°C to avoid unintentional thermal stresses.

To calibrate the relationship between ρ and stress for the superluminescent diodes, known stresses in the plane of the active region were induced by two methods: by direct application of bending forces on unbonded devices, and by changing the temperature of

devices bonded to heat sinks of various materials. With the resulting calibration of ρ vs. stress, the stresses induced by bonding devices to heat sinks were measured.

To apply bending forces to an unbonded diode, it was placed straddling two gold-coated diamond blocks, as shown in Fig. 3.2. The diamonds were bonded to a Cu heat sink, which was placed on the thermoelectric cooler. The diode was centered front to back and side to side within 10 μm over the gap between the diamonds. A steel probe, made from a #76 drill bit sharpened to a knife-edge using 600 grit emery paper, was

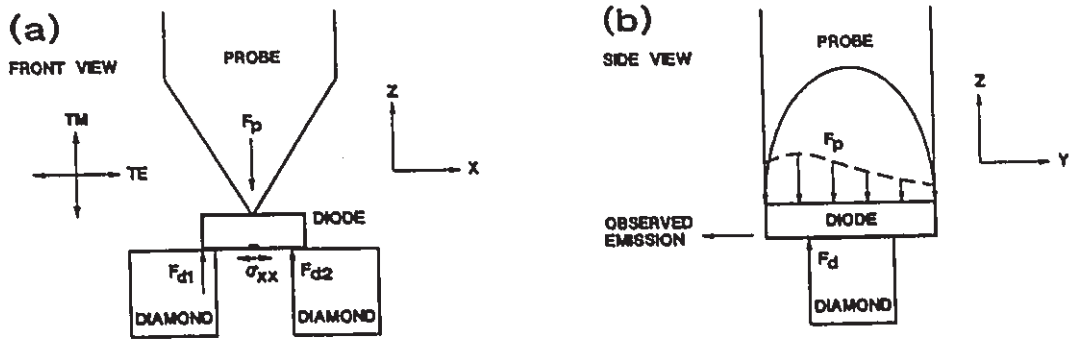

Figure 3.2 Bending forces were applied to unbonded diodes by placing them straddling two diamond blocks. (a) Front view, (b) side view.

pressed down on the center of the diode. The probe also served as the upper electrical contact. The applied force was measured by a strain gauge (Omega type 6/120LY13), with a reproducibility of ± 0.003 N. The strain gauge resistance was measured using an AC bridge circuit (given in the Appendix) and a Princeton Applied Research Model 116 Lock-in Amplifier. The strain gauge was calibrated by inverting the probe mount and balancing a weight on the probe tip. In most experiments, the maximum applied force was 0.5 N, which was low enough to avoid observable damage to the devices.

The device was placed with the active region down to avoid the effects of the probe contact stress. One of the diamond blocks was 3 μm above the other, causing the support points to be asymmetric, as shown in Fig. 3.2(a). This asymmetry was confirmed by moving the diode and probe in the x direction and re-measuring the change in ρ with applied force; the change in ρ increased if the diode and probe were moved to the left ($-x$) and decreased if the diode and probe were moved to the right ($+x$), as expected. The probe was tilted slightly forward to cause the diode to press on the front corners of the diamond blocks as shown in Fig. 3.2(b); otherwise the distribution of force on the diamonds would be indeterminate and dependent upon the surface condition of the diode and diamonds. With this geometry, the induced stress in the active region will vary along the length of the diode, with a greater stress nearer the emitting facet. Since the sensitivity of ρ to stress is weighted toward the facet being observed, this causes an enhanced change in ρ per unit applied force. Readings were also taken with the probe rotated 180 degrees (in case of irregularities in the probe edge) and tilted slightly back, to cause the diode to press on the back corners of the diamonds and induce greater stress near the back facet. Values of the change in ρ per unit applied force were averaged for the two probe orientations. The average represents the change in ρ per unit applied force with uniform stress along the length of the active region, if the sensitivity of ρ to stress varies linearly along the length of the active region. Pressing the corner of the probe to several points along the active region of a device bonded active side up revealed that the sensitivity does in fact vary roughly linearly with position, as shown in Fig. 3.3, so this assumption is reasonable. The relatively large uncertainty in the

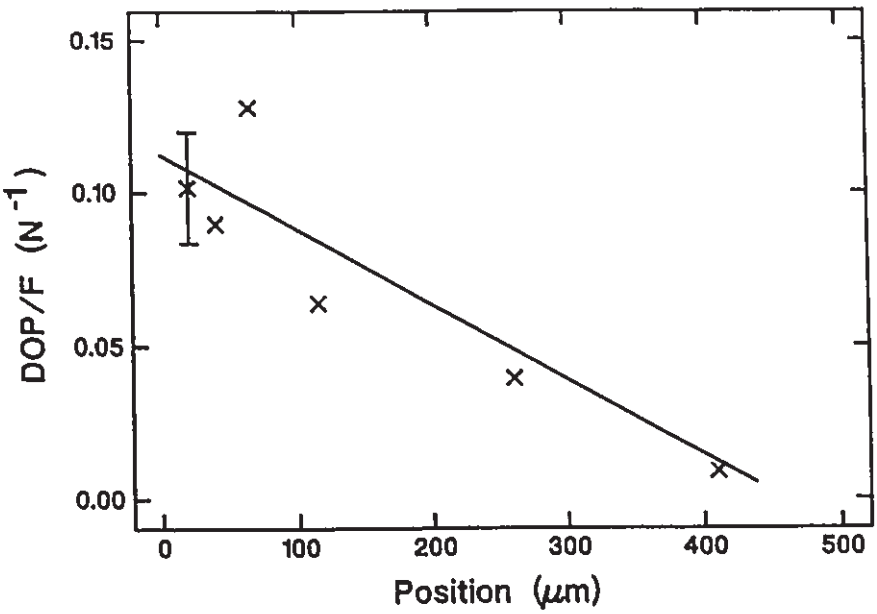

Figure 3.3 The sensitivity to force applied directly to the active region varies roughly linearly with the position along the active region. The observed facet is at 0 μm, and the opposite facet is at 500 μm.

measurements of Fig. 3.3 is due to the difficulty in placing the probe exactly on the center of the 5 μm wide active stripe.

The construction of the force probe is shown in Fig. 3.4. The force probe was designed such that the application of vertical force on the probe does not cause any lateral movement of the probe. The use of flexible beams instead of a sliding stage and a spring ensured zero friction and hence zero hysteresis, and allowed a strain gauge to be mounted on one of the beams as a means to measure the applied force. The length, width, and thickness of the beams were selected to produce a reasonably small spring constant ($\approx$6 N/mm) so that fairly small increments of force could be applied, and so that small deflections in other parts of the probe mount would be negligible. Another design criterion was that the beam material (aluminum) remain in the elastic range ($\sigma <$

35 MPa [61]) up to the maximum probe force that would likely ever be used (5 N). The equations used to design the force probe were

$$\frac{F}{d} = \frac{8Ebh^3}{L^3}$$
$$\sigma_{max} = \frac{3FL}{4bh^2} \tag{48}$$

where F is the applied force, d is the total deflection of the beams, $E = 70$ GPa is Young's modulus of aluminum [61], σ_{max} is the maximum stress in the beam, and $b = 1.27$ cm, $h = 0.159$ cm, and $L = 16.4$ cm are the width, thickness, and length of each beam. The probe was mounted in an acrylic block to provide electrical isolation, and a wire soldered to the probe (not shown in Fig. 3.4) was connected to the diode current source when required. The top of the probe assembly was bolted to an x-y-z translation stage so that the probe could be positioned accurately (within 10 μm) on the diode. The

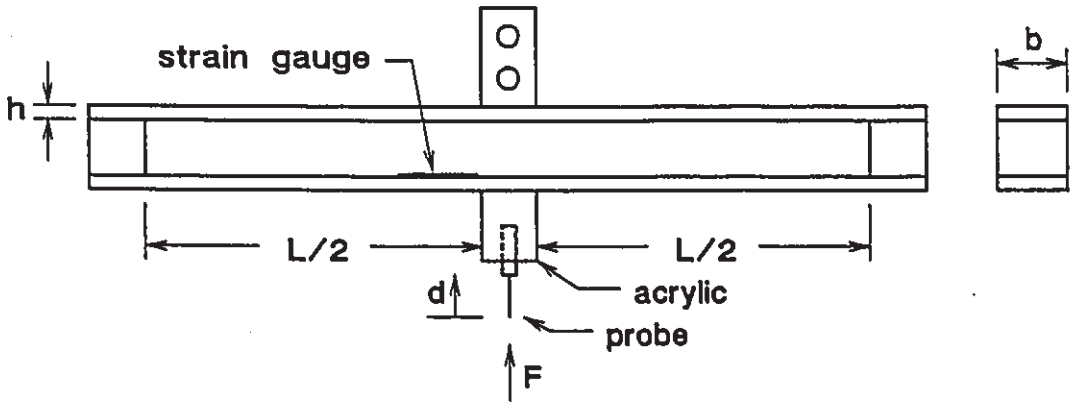

Figure 3.4 A flexible beam design was used for the force probe, to eliminate hysteresis and to allow the use of a strain gauge to measure the applied force.

force was applied by moving the translation stage vertically to press the probe onto the diode.

Stresses were also induced by varying the temperature of bonded devices between 25°C and 70°C. The temperature change induced a plane stress in the active region due to the difference in thermal expansion coefficient between the active region material and the heat sink. The thermal expansion coefficient of GaAs was taken to be the "consensus" value $\alpha = 5.73\times10^{-6}\ °C^{-1}$ [62], and the change in α due to Al content was taken to be $(-1.56\times10^{-6})x\ °C^{-1}$, where x is the mole fraction of Al in $Al_xGa_{1-x}As$ [63]. For the active region in the devices under test, $x = 0.06$, giving $\alpha = 5.64\times10^{-6}$. Copper (1.3 mm thick, $\alpha = 16.6\times10^{-6}\ °C^{-1}$ [64]), Hita-ceram SiC (1.3 mm thick, $\alpha = 3.7\times10^{-6}\ °C^{-1}$ [65]), and diamond (500 μm thick, $\alpha = 1.0\times10^{-6}\ °C^{-1}$ [66]) heat sinks were used to compare different thermal expansion coefficient mismatches. The SiC and diamond heat sinks were gold-coated for solder adhesion and electrical conductivity. Au-Sn solder was used to avoid yielding of the solder during the experiment.

Stress induced during bonding of diodes to heat sinks was determined by measuring ρ of each diode before and after bonding, and the bonding stress was inferred from the change in ρ. The bonding cycle consisted of heating the heat sink, flux, and solder preform using a modified temperature-controllable soldering iron at a rate of 10°C/sec until the solder preform melted (278°C for Au-Sn solder, 183°C for Pb-Sn solder [67]), then pressing the diode into the solder (maximum force 0.5 N) and cooling the heat sink at a rate of 2°C/sec back to room temperature. The devices were

rinsed in isopropyl alcohol and distilled water to remove flux.

The rate of relaxation of the bonding stress for Au-Sn solder was measured as a function of temperature, by observing the changes in ρ over periods of one to three days with the heat sink held at 25°C, 50°C, or 70°C. For the Pb-Sn solder, the rate of relaxation of the bonding stress was much higher, causing much of the stress to relax before ρ could be measured after bonding. Therefore, for Pb-Sn solder, bonding stress was simulated in an already-bonded device by suddenly (within 30 seconds) changing the heat sink temperature by at least 20°C. The relaxation was then observed by measuring ρ at intervals of 5 to 20 seconds for 7 to 30 minutes, with occasional measurements for times up to 2 days.

3.3 Degree of polarization vs. applied stress

The stress induced in the device at the active region per unit applied force on the probe can be approximated using a formula for simply-supported rectangular beams [61],

$$\frac{\sigma_x}{F} = \frac{6w_1w_2}{lh^2(w_1+w_2)} \tag{49}$$

where F is the applied force, w_1 and w_2 are the distances between the probe and the effective support points at the edges of the diode, and l and h are the length and thickness of the diode. The probe is assumed to be positioned directly above the active region. The diode is assumed to be placed active region down for the proper sign of the applied stress. The effect of the 5 degree angle of the active region is ignored. The applied

force and stress are assumed to be uniform along the length of the diode.

The stress induced by a temperature change in a bonded device is calculated assuming no deformation of the mount and no yielding or deformation of the solder. The induced stress is then a plane stress, with $\sigma_x = \sigma_y$ and $\sigma_z = 0$. The change in stress per unit change in temperature is given by

$$\frac{\delta\sigma_x}{\delta T} = \Delta\alpha \frac{E}{(1-\nu)} \tag{50}$$

where $\Delta\alpha = \alpha(\text{heat sink}) - \alpha(\text{active})$ is the difference in linear thermal expansion coefficients between the heat sink and the active region, and δT is the temperature change. For GaAs, $E = 8.5\times10^{11}$ dyn/cm^2 and $\nu = 0.31$ [68].

It is assumed that the relationship between ρ and σ is linear. Note that the value of ρ can only vary between -1 for pure TM radiation and $+1$ for pure TE radiation. Therefore, one cannot expect a linear relationship between ρ and applied stress if ρ varies by more than about 0.1. In the experiments performed here, however, the absolute value of ρ did not exceed 0.08, and the maximum observed change in ρ was less than 0.05, so the assumption of a linear relationship between ρ and σ is reasonable.

The change in degree of polarization per unit applied force ($\delta\rho/F$) was measured for three devices using the setup illustrated in Fig. 3.2. The results obtained were $\delta\rho/F = -0.033$, -0.034 and -0.036 N^{-1} with the probe tipped forward, and $\delta\rho/F = -0.020$, -0.021 and -0.022 N^{-1} with the probe tipped back, giving an average value of $\delta\rho/F = -0.028 \pm 0.001$ N^{-1} for the devices under test. Inserting the relevant dimensions ($l = 500$ μm, $w_1 = 150$ μm, $w_2 = 112$ μm, and $h = 110$ μm, all

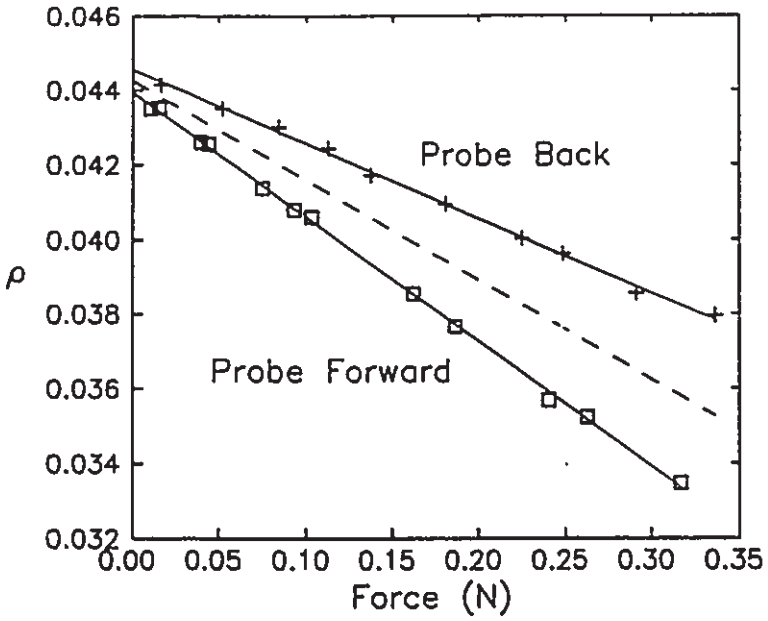

Figure 3.5 The change in ρ vs. applied force for an SLD on the diamond blocks. The dashed line represents the average slope.

measurements ± 10 μm) into Eq. (49) gives $\sigma_x/F = (6.4 \pm 0.9)\times 10^8$ dyn/cm^2·N, so the change in ρ per unit applied stress is $\delta\rho/\sigma_x = -(4.4 \pm 0.6)\times 10^{-11}$ cm^2/dyn. Figure 3.5 shows the observed relationship between ρ and applied force with the probe tipped forward and back for one of the tested devices. The linear relationship between ρ and F is evident from Fig. 3.5. Note that the data points plotted include measurements taken over a complete cycle of applied force, with both increasing and decreasing force. There is no significant deviation of the data points from a single straight line, so hysteresis in the measurement system is negligible. The dashed line in Fig. 3.5 represents the average slope of the two curves for the probe tipped forward and back, corresponding to the case of a uniform stress being generated along the length of the active region.

Stresses were induced thermally in bonded chips by varying the heat sink

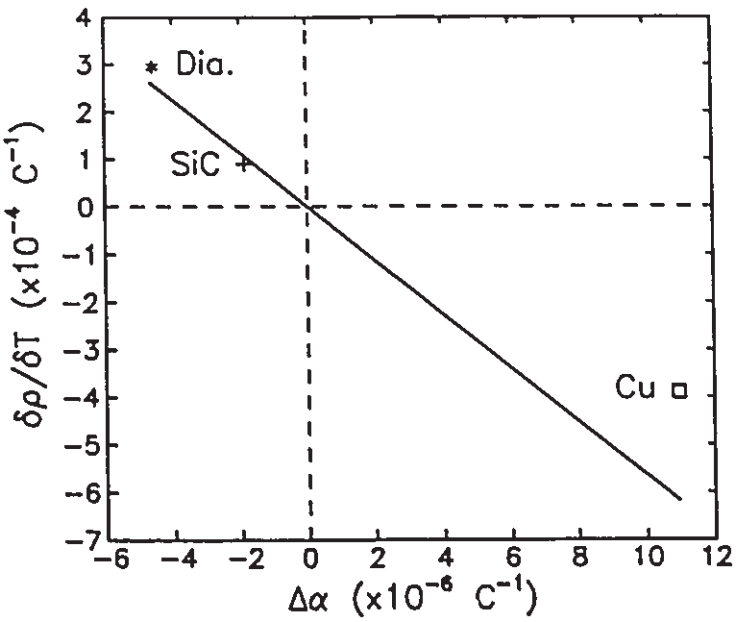

Figure 3.6 The change in ρ per degree of temperature, for devices bonded to diamond, SiC, and Cu heat sinks. The line represents the expected relationship.

temperature by 5 degree increments between 25°C and 70°C. The devices to be tested were bonded active-side down to copper, SiC, or diamond heat sinks using Au-Sn solder. The change in ρ per change in temperature ($\delta\rho/\delta T$) was averaged over the temperature range. Figure 3.6 shows the observed values of $\delta\rho/\delta T$ plotted against $\Delta\alpha$. The straight line represents the expected relationship between $\delta\rho/\delta T$ and $\Delta\alpha$ based on Eq. (50) and the value of $\delta\rho/\sigma_x = -4.4\times10^{-11}$ cm²/dyn measured by direct application of force. The observed values of $\delta\rho/\delta T$ agree reasonably well with the predicted relationship. The fairly large discrepancy in the case of the Cu heat sink may be due to elastic deformation of the heat sink under stress. Nevertheless, it is clear that ρ is indicating the stress in the active region.

3.4 Bonding stress measurements

Measurements were made of stresses induced during bonding of diodes active region down to copper, SiC, or diamond heat sinks, using Au-Sn or Pb-Sn solder. The results are given in Fig. 3.7. The stresses are based on the value of $\delta\rho/\sigma_x = -4.4\times10^{-11}$ cm^2/dyn determined from direct application of bending forces. It was observed for the case of Au-Sn solder that the stresses were of roughly the same magnitude (7-11$\times10^8$ dyn/cm^2) for each heat sink type, and uncorrelated with the magnitude of the difference in thermal expansion coefficient between the heat sink and the active region. The sign of the stress depended on the sign of $\Delta\alpha$, the thermal expansion coefficient mismatch between the heat sink and the active region. The results are consistent with the idea that the bonding stress results from the thermal expansion coefficient mismatch between the heat sink and active region as the device cools below the solder melting point, and that the Au-Sn solder yields if the bonding stress is above about 10^9 dyn/cm^2. For Pb-Sn solder, the magnitudes of the induced stresses were much lower (0-3.5$\times10^8$ dyn/cm^2). Note that the stresses observed for the Au-Sn solder are well above the value of about 1-4$\times10^8$ dyn/cm^2 found to reduce device lifetime in short-wavelength (<780 nm) AlGaAs lasers [5,11,10].

To compare my bonding technique with that of a commercial supplier, I measured bonding stresses for devices bonded to Cu heat sinks by EG&G Optoelectronics using Au-Sn and In solder. The Au-Sn bonding stresses for four EG&G-bonded devices were (1.9 $\pm$ 0.2)$\times10^9$ dyn/cm^2, which is about twice that for those which I bonded myself.

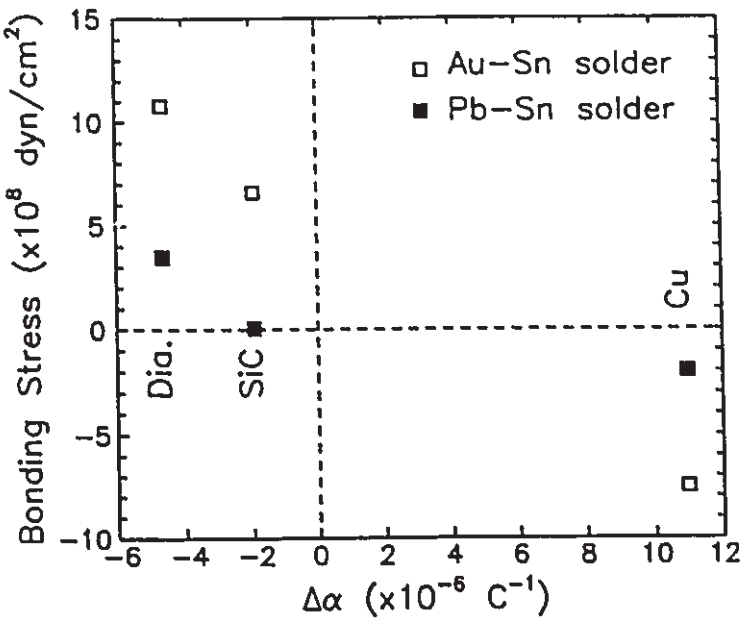

Figure 3.7 Measured bonding stresses for diodes bonded to diamond, SiC, or Cu heat sinks using Au-Sn or Pb-Sn solder. The stress magnitude depends on the solder type, and the sign of the stress depends on $\delta\alpha$.

The bonding stress for In solder would be expected to be lower than Pb-Sn solder due to its lower melting point (156°C). However, the four devices bonded with In solder by EG&G showed bonding stresses of $(3.7 \pm 2.5)\times10^8$ dyn/cm^2, which is greater than that for my Pb-Sn bonded devices. There are two possible explanations for the larger stresses in the EG&G-bonded devices. The Cu heat sinks used by EG&G had a gold coating, while mine did not. The gold coating could melt into the solder during the bonding and harden the solder, increasing the bonding stress. The bonding procedure, in particular the cooling rate after bonding, could also affect the bonding stress. The bonding procedure used by EG&G involves rapid temperature changes, about 50°C/s, to minimize the time required to bond each device. My procedure used relatively slow temperature changes (10°C/s heating, 2°C/s cooling), limited by the heating and cooling rates of the

modified soldering iron. It is possible that a slow cooling rate allows solder relaxation to occur while the solder is still relatively hot and soft. Extrapolating the solder relaxation time of Eq. (53) to 250°C results in a relaxation time of only 1.3 minutes. This suggests that allowing the device to cool over a period of several minutes after bonding could result in a lower bonding stress.

For comparison with the active-down measurements, two devices were bonded active region up to Cu heat sinks using Au-Sn solder. Both devices exhibited a tensile bonding stress (4.2×10^8 dyn/cm^2 and 1.8×10^8 dyn/cm^2), in contrast to the compressive stress observed for bonding active region down to Cu. This suggests that the compressive stress on the lower surface of the devices caused them to bend, resulting in a tensile stress on the upper (active) surface. Increasing the temperature of the bonded devices from 25°C to 70°C induced a slight additional tensile stress ($\delta\rho/\delta T = -0.33\times10^{-4}$ C^{-1} and -0.58×10^{-4} C^{-1} respectively), which is opposite to what would be expected based on the sign of the bonding stress. The reason for this behaviour has not been investigated.

3.5 Solder relaxation

Relaxation of the bonding stress for the device bonded to Cu using Pb-Sn solder was observed to follow an equation of the form

$$\Delta\rho = e^{A}t^{-B} \tag{51}$$

where $\Delta\rho$ = abs(ρ − (pre-bonding ρ)), t is the time in hours since the application of

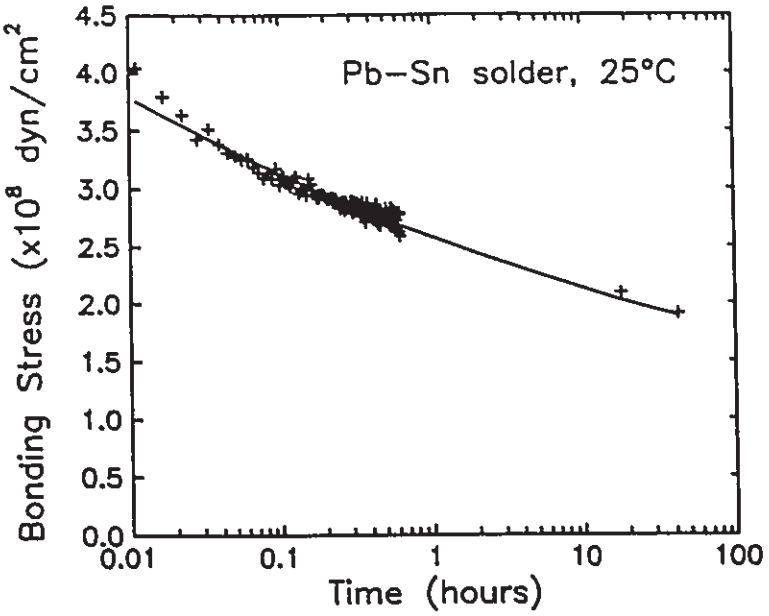

Figure 3.8 An example of Pb-Sn solder relaxation for a device bonded to a Cu heat sink. The line represents the fit curve $\rho = e^{-4.48}t^{-0.084}$.

stress (change in temperature), and A and B are constants which vary roughly linearly with temperature. This formula was followed over a time period from 30 seconds to 2 days after the application of stress. Based on data taken at 25°C, 50°C, and 70°C, the values of A and B are given by $A = (-3.3 - 0.052T) \pm 0.2$ and $B = (0.01 + 0.0032T) \pm 0.02$, where T is the heat sink temperature in degrees Celsius and the uncertainties indicate the scatter in the experimental data. An example of the relaxation behaviour is shown in Fig. 3.8. In this case the temperature was raised to 70°C for 10 minutes, then reduced to 25°C to induce stress, and readings were taken with the heat sink held at 25°C. Repeating the temperature cycling caused the relaxation behaviour to repeat itself, confirming that the relaxation is not due to irreversible strain relief in the device itself.

The relaxation rate for Au-Sn solder was much slower than that for Pb-Sn solder.

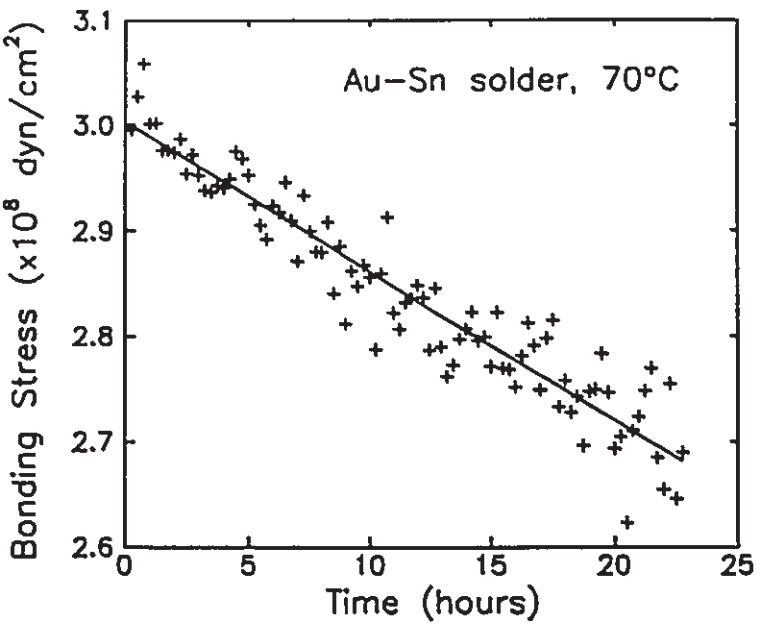

Figure 3.9 An expample of Au-Sn solder relaxation for a device bonded to a Cu heat sink.

Over a time period of 1 to 3 days, the change in ρ with time was essentially linear, as shown in Fig. 3.9. Occasionally there was an initial 4 to 7 hour period of increased relaxation after a temperature change. The bonding stress relaxation time τ was measured for the Au-Sn solder,

$$\tau = \frac{\Delta\rho}{\left[\frac{d\rho}{dt}\right]} \tag{52}$$

where $d\rho/dt$ is the rate of change of ρ after bonding, and any initial period of increased relaxation is ignored. The results are shown in Fig. 3.10 for the two devices tested (Cu and diamond heat sinks). The value of τ followed the formula

$$\tau = A e^{Q/kT} \tag{53}$$

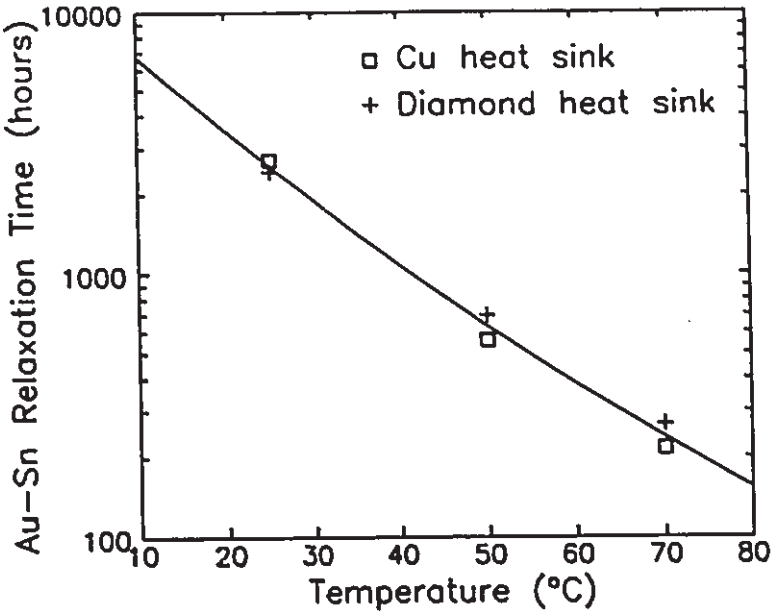

Figure 3.10 The variation in relaxation time τ with temperature for devices bonded to Cu and diamond heat sinks with Au-Sn solder. The fit curve is $(2.9\times10^{-5}\text{ hours})e^{(0.47\text{ eV})/kT}$.

within 15 percent for $T = 25°C$, 50°C, and 70°C, where $A = 2.9\times10^{-5}$ hours, $Q = 0.47$ eV is the activation energy for the solder relaxation, $k = 8.6\times10^{-5}$ eV/K is Boltzmann's constant, and T is the heat sink temperature in degrees Kelvin. A temperature dependence of the form of Eq. (53) is expected for creep in metals [69].

Figure 3.11 shows the relaxation behaviour for a device bonded with Au-Sn solder to a Cu heat sink over a longer time period. The relaxation behaviour follows the form of At^{-B} over the longer time period, similar to the behaviour of Eq. (51) for Pb-Sn solder.

In measurements presented so far in this chapter, no spatial resolution of the electroluminescence was attempted. Only the stress at the light-emitting active region was being sought, and it was assumed that most of the luminescence would be emitted

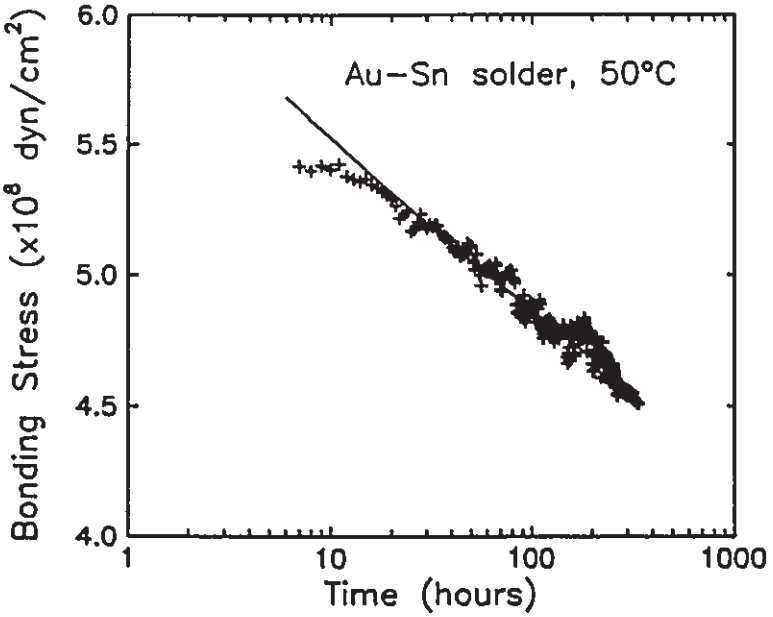

Figure 3.11 The relaxation behaviour for Au-Sn solder over a longer time period. The line represents the fit curve $\sigma = (3.9\times10^8\ \mathrm{dyn/cm^2})t^{-0.071}$.

near the 5 μm wide active stripe. This is in fact the case, but it was also observed that even at low current levels, light can be observed from the active layer across the full width of the diode facet. This light is of sufficient intensity to obtain degree of polarization measurements across the full width of the facet, providing more detailed stress information. With the optical setup used, the 5 mm diameter detectors would capture light from an area about 80 μm in diameter on the diode facet. To obtain a finer spatial resolution, a vertical adjustable slit was placed in front of the beamsplitter cube as shown in Fig. 3.2 and the facet emission was focussed onto the slit to allow only the emission from a selected region of the facet to reach the detectors. The active layer could then be scanned by moving the microscope objective, or for finer resolution (but a smaller scan range), by scanning the slit. The spatial resolution could be adjusted by

varying the width of the slit.

Figure 3.12 shows the degree of polarization of the electroluminescence of two SLD's with a 10 μm resolution across the entire facet. These devices were bonded active side down to Cu heat sinks with Au-Sn or In solder. The degree of polarization of these

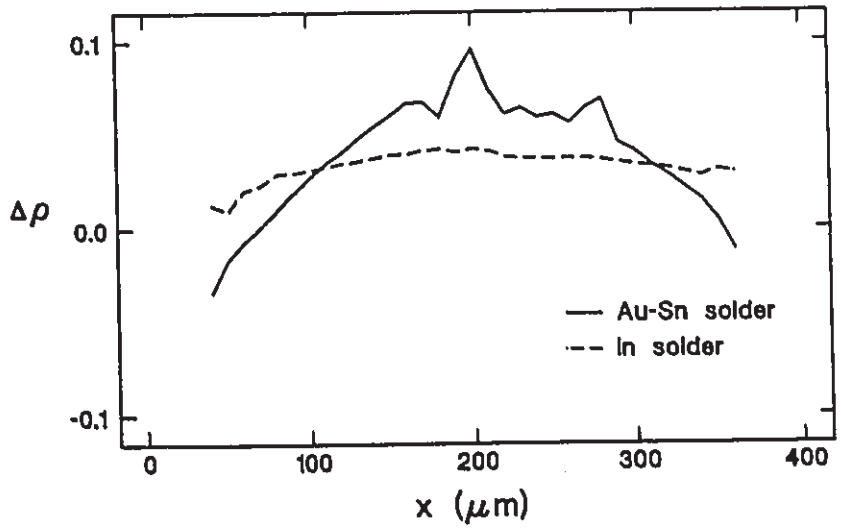

Figure 3.12 The degree of polarization of facet emission across the width of the facet for devices bonded to Cu heat sinks with In and Au-Sn solder.

devices before bonding ($\rho \approx 0.07$) has been subtracted from the data, so the ordinate axis is labelled as $\Delta\rho$. The bonding stress distributions are clearly not uniform across the width of the diodes. The distribution of ρ is much more uniform for the In-bonded device due to the smaller magnitude of the bonding stress.

A simplified theory of bonding stress relaxation can explain the shape of the Au-Sn bonding stress distribution observed in Fig. 3.12. Figure 3.13 illustrates the situation considered. It is assumed that the diode thickness h is much less than the width $2L$, so that the problem becomes one-dimensional and the diode stress can be considered

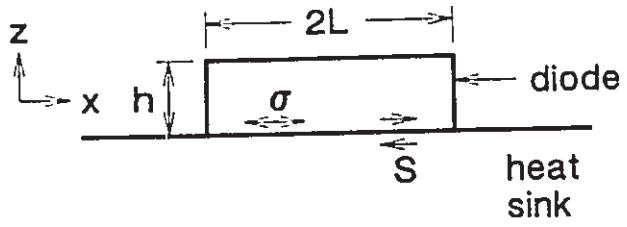

Figure 3.13 Illustration of the model for solder relaxation.

to be only a function of position x and time t, $\sigma(x,t)$. It is assumed that the heat sink does not deform, which will be reasonable if the heat sink is much thicker than the diode. The solder is assumed to support a shear stress distribution $S(x,t)$ at the bonded interface. The relationship between $S(x,t)$ and $\sigma(x,t)$ is given by

$$S = h\frac{d\sigma}{dx} \tag{54}$$

The diode stress is related to the strain by $\sigma = E\epsilon$, and the strain is related to the displacement u by $\epsilon = du/dx$, so

$$\sigma = E\frac{du}{dx} \tag{55}$$

Now it is assumed that the solder behaves as a viscous fluid, such that the rate of flow is proportional to the applied stress, or

$$\frac{du}{dt} = kS \tag{56}$$

The rate of creep in metals does not usually vary linearly with stress, but varies to a power of stress between 1 and 7 [69]. The power is usually between 2 and 4 for alloys. However, at low stresses and high temperatures (near the melting point), the

power approaches unity. Because of the low melting point of solder, room temperature could be considered to be in the 'high temperature' regime, so Eq. (56) may be reasonable. Note that as the solder deforms the resulting work-hardening may reduce the rate of subsequent flow [69], resulting in a time-dependent and spatially-dependent value of k. However, to keep the problem simple at this point, a constant value of k is assumed. Differentiating Eq. (55) with respect to time t and substituting (56) and (54),

$$\frac{d\sigma}{dt} = E\frac{d^2u}{dxdt} = kE\frac{dS}{dx} = kEh\frac{d^2\sigma}{dx^2} \tag{57}$$

which is the well-known diffusion equation. In this case, the boundary condition is $\sigma(x,t) = 0$ for $x = L$ and $x = -L$, and the initial condition is $\sigma(x,0) = \sigma_0$ for $-L<x<L$. The resulting solution is given by

$$\sigma(x,t) = \frac{4\sigma_0}{\pi}\sum_{n=1,3,\ldots}\frac{(-1)^{\frac{n-1}{2}}}{n}\cos\left[\frac{2\pi nx}{L}\right]\exp[-kEh(2\pi n/L)^2t] \tag{58}$$

For $t \gg 1/kEh(2\pi/L)^2$, the first term of the series will dominate, and

$$\sigma(x,t) = \frac{4\sigma_0}{\pi}\cos\left[\frac{2\pi x}{L}\right]\exp[-kEh(2\pi/L)^2t] \tag{59}$$

A cosine distribution of stress is therefore expected for highly relaxed solder. The observed stress distribution for Au-Sn solder in Fig. 3.12 does indeed resemble a cosine curve. A stress of about $\sigma_0 = E\Delta\alpha\delta T/(1-\nu) = (8.8\times10^{11}\ \text{dyn/cm}^2) \times (11.7\times10^{-6}\ \text{C}^{-1}) \times (-253°\text{C}) / (1-0.31) = -3.8\times10^9\ \text{dyn/cm}^2$ would be expected if no solder relaxation occurred, and the observed stress was about $-2\times10^9\ \text{dyn/cm}^2$, so some solder relaxation has occurred during the cooling process. The observed cosine shape of the

bonding stress is therefore expected.

The relaxation properties of the solders are important for interpretation of high-temperature life-testing of bonded superluminescent or laser diodes. When the temperature is increased to perform the life-test, a stress is induced in the device by the mismatch in thermal expansion coefficients of the active region and heat sink. The solder will gradually relax to relieve the induced stress caused by the temperature change. This will cause changes in threshold during the early hours of the life test which are due to reversible stress effects, not irreversible aging. If the device is returned to room temperature for several hours or days to test the device, the opposite stress is induced, and the solder will begin to relax again. Upon resumption of the aging test, a stress is again induced which will gradually relax, causing a transient discontinuity in the test data. Test data showing these effects have been reported [70],[71], and the duration of the effects correspond well with the relaxation times predicted by Eq. (53). The presence of initial rapid degradation has been noted to depend upon the solder type and mounting polarity (active side up or down) [72], suggesting that this effect may also be related to bonding stress or solder relaxation. The effect of bonding stress on initial rapid degradation certainly deserves further study.

3.6 Stress-enhanced aging

In this section, some experiments are described which indicate that mechanical stress accelerates the aging of diode lasers and superluminescent diodes. The

experiments were performed using the same force probe and diamond blocks used in the calibration experiments.

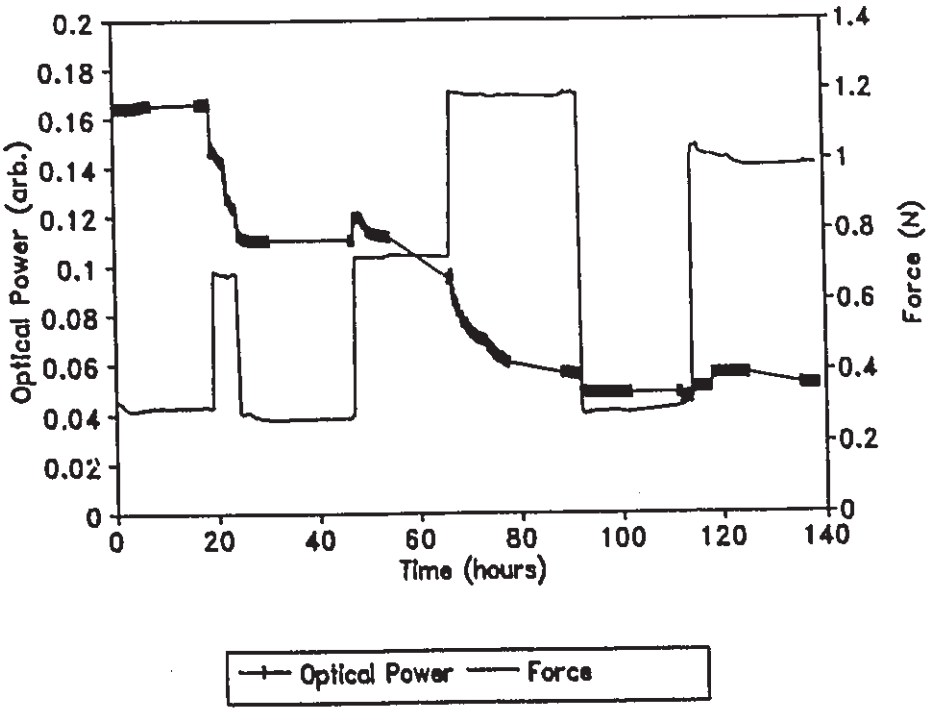

Figure 3.14 An aging experiment for sample 831-22 showing increased aging under the application of mechanical stress.

Figure 3.14 shows an aging experiment for a superluminescent diode, sample 831-22. The applied force was changed periodically during the experiment. In this case, the diode was placed active side up on the diamond blocks, but similar results were obtained with diodes placed active side down. It can be clearly seen that the application of stress induced accelerated degradation. Each time the applied stress was increased beyond the previous maximum, an initial rapid degradation occurred. When the applied stress was reduced, the degradation rate returned to the rate before the application of increased stress. When the stress was re-applied, the degradation rate seemed to return to the rate

at which it left off when the stress was last removed, without a new period of initial rapid degradation. Thus, it seems that each level of applied stress induces a different mode of degradation, or causes a different class of defects to form. Higher-level defects, induced by higher applied stress, cause more rapid degradation. The same degradation mechanism cannot be responsible for degradation occurring at all stress levels, otherwise the initial rapid degradation would occur only once, instead of each time the stress is increased.

It was observed that no degradation occurred if only stress was applied, with little or no current through the diode. Thus, the simultaneous application of stress and current are necessary for stress-enhanced degradation to occur. This is in agreement with the assumption that the applied stress accelerates recombination enhanced defect motion, increasing the degradation rate.

Figure 3.15 shows an aging experiment for a superluminescent diode number 164-12, which is similar to sample 831-22, but from a different batch. This sample showed a much lower degradation rate than sample 831-22, and did not show any increased degradation with applied stress. Other samples from batch 164 behaved similarly. The difference in degradation behaviour between the two batches suggests that the applied stress does not in itself induce degradation, but only activates degradation-inducing defects already present in the diode, such as dislocations.

The observed aging behaviour could be explained by the threshold stress effect of recombination enhanced dislocation motion discussed in Section 2.4. The dislocations present in the diode active layer will grow into larger defects only if the sum of the

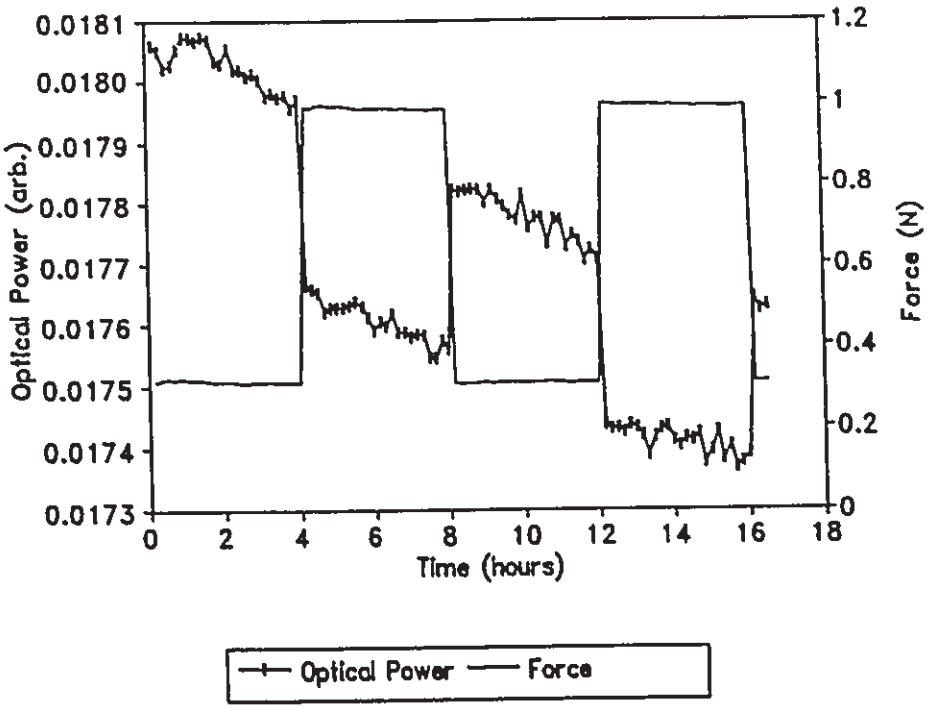

Figure 3.15 An aging experiment for diode 164-12, showing no change in the degradation rate with applied stress.

internal stress and the externally-applied stress exceeds the threshold stress. If the internal stress distribution varies across the active region of the diode, then as the external stress is increased, more and more dislocations will experience a total stress above the threshold stress. Also, different dislocation types may have different threshold stresses. This could explain the repetition of the initial rapid degradation behaviour with each increase in applied stress. It is reasonable that once each dislocation grows to a certain size such as the width of the active region, or reaches a pinning site such as an impurity atom, further degradation due to that dislocation is reduced. This would cause the observed initial rapid degradation. To further explore these hypotheses, an experiment could be devised in which the dislocation motion could be monitored during

aging under stress. Scanned polarization-resolved electroluminescence [60] or photoluminescence could be used to monitor the defect motion, and it should be possible to devise an arrangement for applying and varying the stress while the diode is in the scanning apparatus.

Although aging of diodes on the diamond blocks allows the applied stress to be varied during the test, it does not accurately represent the operation of properly bonded diodes, because the thermal contact between the diode and the diamond blocks is quite poor compared to a diode bonded to a heat sink. The thermal contact alone would not explain increased degradation with applied stress, because the thermal contact would improve with increased applied force on the probe, and would result in a lower junction temperature and hence decreased degradation with applied stress, which is opposite to the observed effects. However, the poor thermal contact may somehow contribute to the ability of stress to influence the degradation rate, possibly by allowing the active region to reach a higher temperature at which stress effects become significant. For this reason, an experiment was performed to compare the aging characteristics of diodes bonded to copper heat sinks, with Au-Sn and In solders used to induce different stress levels in the bonded devices. Six devices were bonded with each solder type. To ensure that the bonding procedure used would represent that used in commercial devices, the bonding was performed by staff at EG&G Optoelectronics. Some of the devices failed to operate after bonding due to short-circuiting of the devices by the solder. This was not considered to be a factor which would affect the behaviour of the surviving devices. The bonding stresses were determined using measurements of the degree of polarization of

the electroluminescence made before and after bonding for each device. The Au-Sn solder induced a stress of about 2×10^9 dyn/cm^2, and the In solder induced a stress of about 4×10^8 dyn/cm^2.

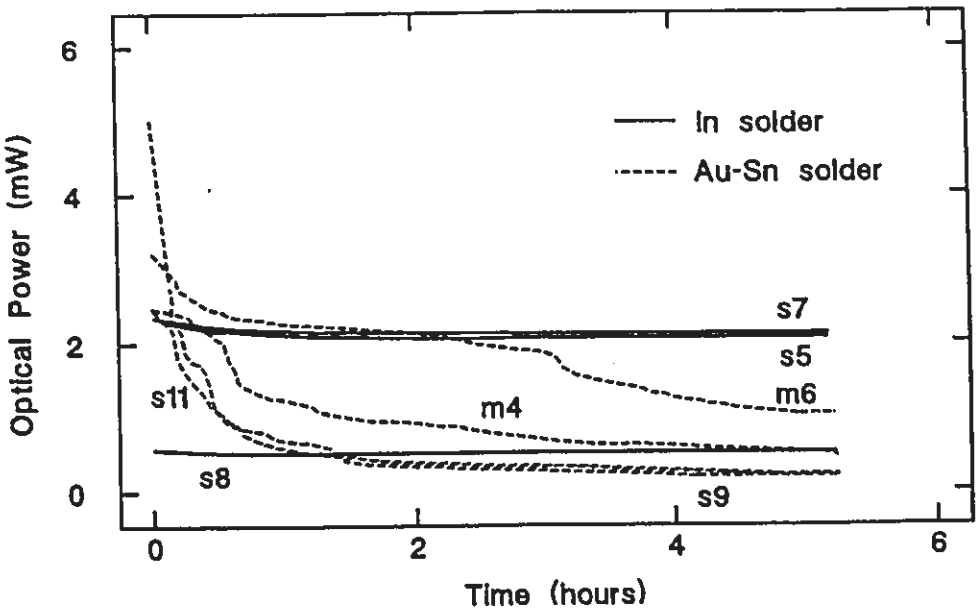

Figure 3.16 Superluminescent diodes bonded with Au-Sn solder degraded much more rapidly than those bonded with In solder.

The aging of the devices was performed at 50°C and 245 mA (normal operating conditions for these diodes would be 22°C and 250 mA). Figure 3.16 shows the results of the initial aging period for the devices which operated after bonding. The devices bonded with Au-Sn solder aged much more rapidly than those bonded with In solder, indicating that the increased bonding stress caused enhanced degradation. Thus, the increased degradation observed with applied stress using the diamond blocks is not due to factors such as poor thermal contact which would not be present in a properly bonded device.

3.7 Summary

Measurements of the stress induced by bonding AlGaAs superluminescent diodes to Cu, SiC, and diamond heat sinks with Pb-Sn and Au-Sn solder have been reported. The stress was deduced from changes in the degree of polarization of the facet emission for low current injection. The magnitude of the bonding stress was found to depend primarily on the solder used, with Au-Sn solder causing a larger induced stress. The sign of the stress (tensile or compressive) was found to depend on the sign of the thermal expansion coefficient mismatch between the heat sink and the active region.

The rate of relaxation of the bonding stresses was measured for the Au-Sn and Pb-Sn solders as a function of temperature, and empirical formulas were found for the rate of relaxation. The relaxation time for Au-Sn solder at 25°C was found to be about 100 days, while for Pb-Sn solder substantial relaxation occurred within minutes. The relaxation of the solder should be taken into account when interpreting aging data for bonded superluminescent and laser diodes, since some changes in light output may be due to relaxation of bonding stress, not device aging.

Stress-enhanced aging was observed in devices from batch 831, but not in devices from batch 164. This suggests that pre-existing defects such as dislocations, present in one batch but not the other, are responsible for the effect. The occurrence of stress-enhanced aging reinforces the importance of stress measurements in diode lasers and SLD's.

Chapter 4. Photoluminescence Measurements

4.1 Introduction

In this section, images of stresses on the facets of GaAs and InP diode lasers and SLD's, obtained using spatially-resolved and polarization-resolved photoluminescence, are presented. A stress resolution of about 10^7 dyn/cm^2 (strain resolution about 10^{-5}) and a spatial resolution of about 1 μm full width at half maximum (FWHM) have been achieved, which makes this the first technique capable of resolving the stress features near the active region of diode lasers with this combined resolution. Broader stress distributions over the entire laser facet can also be easily imaged.

The degree of polarization ρ is defined in this chapter, as in previous chapters, by Eq. (1). For the stress distributions measured in this chapter, it is expected that σ_{xx} is the dominant stress; measured stresses are therefore reported as the value of σ_{xx} rather than $(\sigma_{xx}-\sigma_{zz})$.

4.2 Experimental technique

The experimental setup is shown in Fig. 4.1, and the x, y, and z directions and the crystal axes relative to the observed facet are indicated in Fig. 4.2. A mechanically chopped (about 1 kHz, 5 mW) HeNe laser (633 nm wavelength) is reflected off a cold

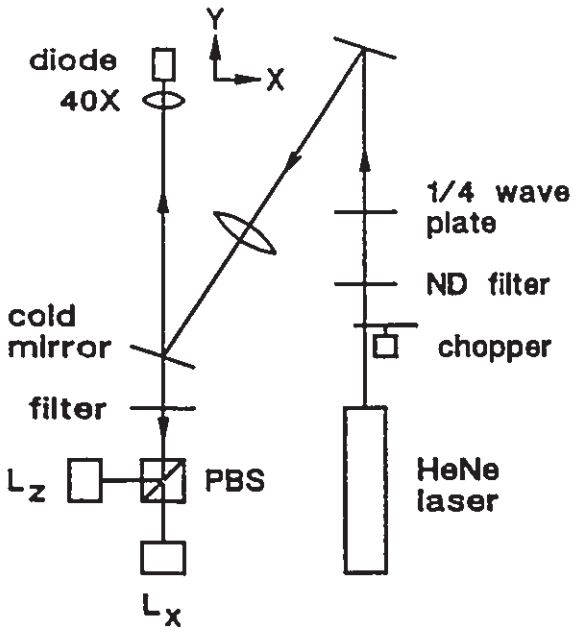

Figure 4.1 The experimental setup for polarization-resolved photoluminescence.

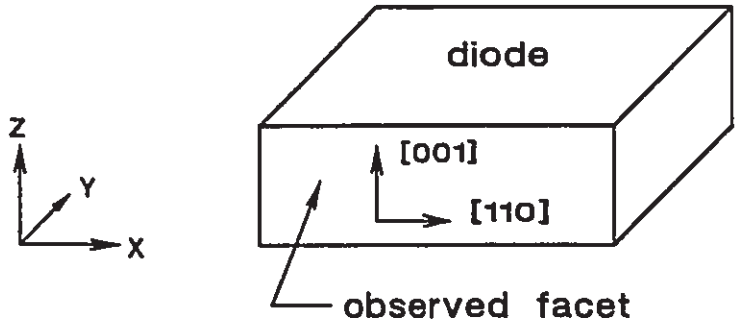

Figure 4.2 The coordinate axes and the crystal orientation with respect to the observed diode facet.

mirror and focused onto the diode facet using a 40×, 0.65 NA microscope objective (Newport M-40X). The luminescence from the facet is collected with the same objective in a confocal arrangement, and passes through the cold mirror (Melles Griot 03 MCS 005) to a polarizing beamsplitter cube (PBS) (Newport 10FC16PB.5). A filter (Melles Griot 03 FCG 111, RG715) removes any remaining HeNe light. The two polarizations

are detected using two 200 μm diameter Si p-i-n photodiodes (L_1, L_2), after an optical path length of 1.3 m. Phase-sensitive detectors (PSD's) are used to reject ambient light signals and reduce noise. The photodiodes must be aligned to within 10 μm to image the same point on the laser facet, in a manner described by Peters and Cassidy [60].

The lens in the path of the HeNe laser beam is required to make the focal point of the HeNe beam lie on the diode facet when the luminescence is focused on the photodiodes, and to compensate for chromatic aberration in the microscope objective between the HeNe and luminescence wavelengths. The focal length of 300 mm of this lens was selected such that the HeNe beam just filled the 6 mm aperture of the objective lens, to obtain the smallest diffraction-limited spot size on the diode facet while maintaining efficient throughput of the HeNe light. The neutral density (ND) filter (optical density 0.4) and quarter-wave plate in the HeNe path reduce the amount of the back-reflected HeNe light which feeds back into the laser, to reduce fluctuations in the HeNe laser power. The HeNe laser is polarized, so that a polarizer is not necessary in conjunction with the quarter-wave plate. About 2 mW of the HeNe optical power is transmitted through the ND filter.

The diode is scanned past the microscope objective to obtain spatially-resolved images of the photoluminescence. Scanning the diode rather than the objective lens leaves the optical alignment undisturbed. The scanning is done under computer control using DC motor drives (Oriel Motor Mike) to move the translation stages and electronic gauge units (Mitutoyo series 519 Mu-checker gauge heads) to determine the position. At each scan point, values of L_x, L_z, and ρ are recorded onto disk. Scanning is done

unidirectionally to eliminate hysteresis effects. The system allows positioning repeatability within about 0.1 μm, while the smallest step size used was 0.5 μm.

It is worth noting that the uncertainty of the calculated values of ρ is less than the relative uncertainty of L_x or L_z, because some of the uncertainties are due to factors which affect L_x and L_z equally, such as fluctuations in the HeNe laser power and sub-micron changes in the distance between the diode laser facet and the microscope objective as the diode is scanned past the objective. It is therefore important that L_x and L_z be measured simultaneously for minimum uncertainty in the calculated values of ρ. When the computer reads and averages the values of L_x and L_z, the readings are interleaved, taking 10 readings of one channel, then 10 readings of the other, to obtain readings as near to simultaneous as possible. Changing from one channel to the other after each reading is not desirable because of a time delay required after changing channels. A total of 300 readings of each signal are taken within the one second averaging time.

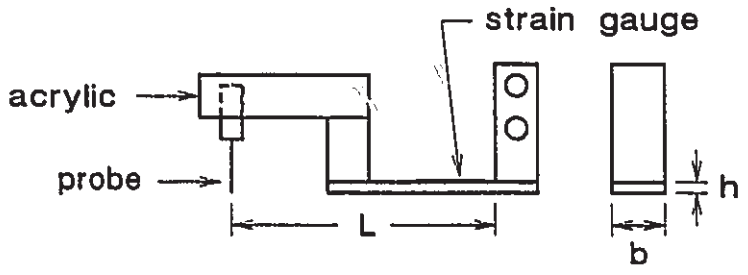

Figure 4.3 The design of the probe mount used with the photoluminescence setup.

A probe with a spherical tip (radius of curvature about 50 μm) is mounted on the moving platform which carries the diode. This probe can be used to apply force to

diodes while being scanned, to determine the effect of a known stress on the measured degree of polarization. The probe was made from a #76 drill bit by removing the grooved portion of the bit and shaping the tip with 600 grit emery paper. The probe mount is equipped with a strain gauge for measuring the applied force with a resolution of ± 0.004 N. The probe also serves as an electrical contact for unmounted diode lasers. The design of the probe mount is illustrated in Fig. 4.3. Since this probe mount is on a moving platform, its size and weight should be kept to a minimum. To minimize the size of the probe mount, a single beam spring design was used instead of the dual-beam design used in the electroluminescence experiments, and the design parameters were relaxed slightly, with a lower maximum applied force of 3.7 N and a higher spring constant of 6.8 N/mm. The probe mount was designed such that the probe point was on the same level as the beam spring, to minimize lateral motion of the probe point when force is applied. The design equations for the single-beam probe mount are

$$\frac{F}{d} = \frac{Ebh^3}{4L^3}$$
$$\sigma_{max} = \frac{6FL}{bh^2} \qquad (60)$$

where the dimensions are $L = 5.08$ cm, $b = 1.27$ cm, and $h = 0.159$ cm. The part of the probe mount holding the probe itself is made from acrylic to provide electrical isolation. A wire soldered to the probe (not shown in Fig. 4.3) is connected to the diode current source when required.

To align the system, first the electroluminescent signal from a GaAs-based diode laser is maximized. The full-width at half maximum (FWHM) of the electroluminescent

signal should be 2 μm or less in the vertical direction, perpendicular to the active layer, when the diode facet is properly focussed. Then the diode is moved vertically such that the detectors are imaging the substrate material. The HeNe beam is then aligned for maximum photoluminescence signal. Aligning the HeNe beam involves adjusting the two mirrors while monitoring the photoluminescence signal. This alignment is repeated for several positions of the lens in the HeNe path, to find the optimum position of the lens. A one-dimensional photoluminescence scan across the features near the active layer of the diode (with zero diode current) is done to check the spatial resolution of the system and ensure that optimum alignment has been obtained. A FWHM of 1 μm or less should be obtained for the photoluminescence peak from the active layer. The reduction in FWHM for photoluminescence compared to electroluminescence is due to the resolution enhancement of a confocal imaging system [73]. For electroluminescence, the resolution is determined by the point spread function of the microscope objective at the luminescence wavelength. The point spread function can be interpreted as either the shape of the best-focussed spot or the shape of the image of a point object. For photoluminescence, the resolution is determined by the product of the point spread functions of the pump laser beam and the luminescence. This product will be at least as narrow as the narrower of the two point spread functions. The point spread function for the HeNe pump beam should be narrower than that of the luminescence due to the smaller diffraction-limited spot size of the shorter wavelength, and due to the absence of chromatic aberration for the monochromatic HeNe laser light. Therefore, a higher spatial resolution is expected for photoluminescence.

Once the system is aligned, focusing onto each sample is done by simply adjusting the diode position to maximize the luminescent signal from the substrate. The HeNe light striking the diode may be viewed through a microscope to obtain a rough focus and to ensure that the HeNe beam is incident on the diode facet. Fine adjustments of the microscope objective toward and away from the facet will then bring the facet into focus, maximizing the photoluminescence signal. The program XYZ.FOR is used for alignment and focussing, providing a continuous readout of the detected signals and the diode position and controlling the diode movement and PSD gain. The program PL.FOR performs the scanning, moving the diode and saving the data to disk. The focus must be maintained within a tolerance of about 1 μm during a scan, so three points on the facet are focused before a scan to determine the plane of the facet, and the y position is continually adjusted as x and z vary to keep the plane of the facet in focus.

Each data point requires about 2 seconds, which includes averaging the optical signals for about 1 second to reduce noise, and movement to the next position. Therefore, a typical scan of 101 $\times$ 61 data points requires about 3 hours to complete. Reduction of the scan time by an order of magnitude should be possible by using a faster positioning system and by reducing the averaging time. The averaging time is determined by the signal-to-noise ratio of the detected luminescence, and by the required stress resolution. The noise level in each reading can be reduced and hence the stress resolution increased by averaging over a longer time period, or conversely, the averaging time could be reduced by accepting a higher noise level and hence a lower stress resolution. For the present system, the dominant noise source is the detector amplifier

circuit, and the noise equivalent power is about 0.3 pW/$\sqrt{}$Hz. The averaging time could be reduced without loss of stress resolution by increasing the signal-to-noise ratio of the detected luminescence. This could be accomplished by increasing the signal level with a higher pump laser power or larger-area detectors (this may cause some loss of spatial resolution [74]), or by decreasing the noise with lower-noise (e.g. cooled) detectors and/or amplifiers.

A spatial resolution of about 0.9 μm (FWHM) was obtained using a 40×, 0.65 NA microscope objective, based on the observed size of features in the images obtained. A slightly higher spatial resolution of about 0.7 μm (FWHM) could be obtained with a 60×, 0.85 NA objective, but with tighter focussing requirements and a resulting loss of stress resolution and repeatability, so the 40× objective was used for most measurements. With the 40× objective, a stress resolution of $\pm 1 \times 10^7$ dyn/cm^2 was obtained for GaAs and $\pm 3 \times 10^6$ dyn/cm^2 for InP based on the standard deviation of readings of ρ in scans of nominally unstressed material. The higher stress resolution for InP is due to its greater luminescence intensity, resulting in a higher signal-to-noise ratio. Repeatability of stress measurements between scans, with removal and replacement of the sample, is about $\pm 3 \times 10^7$ dyn/cm^2.

A major factor affecting the repeatability of stress measurements is the change in degree of polarization of the collected light as the objective lens is moved toward and away from the diode facet. Ideally, moving the objective lens toward or away from the facet should not affect the degree of polarization measurement. However, stress birefringence, circular asymmetry, or possibly dirt in the objective lens causes the degree

of polarization to vary by as much as 0.005/μm. The objective lens was determined to be the source of the effect because rotating the objective lens about the optical axis by 90 degrees reverses the sign of the polarization change. Several objectives were tried, some very expensive, but none were free of the effect. Apparently the minor asymmetry causing the change in degree of polarization with focussing is either difficult to eliminate or is not a problem in other microscopy applications. The problem was minimized by selecting the available objective lens which showed the minimum change in ρ with focussing. In addition, the objective lens was rotated to the angle at which the change in ρ was a minimum. Recall that a 90 degree rotation reverses the sign of the effect, so there must be an angle at which the effect is zero. A shim, made by cutting a circular hole in a piece of paper of the appropriate thickness, was placed between the objective seating surface and the threaded objective holder, such that when the objective was tightened into the holder the resulting angle of the objective corresponded to the angle of minimum change in ρ with focussing. With these precautions, the change in ρ with focussing was reduced to less than 0.001/μm.

4.3 Experimental Results

In this section, a scan taken near the active region of a ridge waveguide quantum-well laser is first presented, to illustrate the form of the luminescence data obtained and the methods used to depict the distribution of ρ. This scan also illustrates the spatial resolution and the resolution in degree of polarization ρ of polarization-resolved

photoluminescence. A ridge waveguide laser made by a different manufacturer is shown to have similar active region stresses. Next, a calibration experiment is described from which the relationship between ρ and applied stress σ_{xx} was determined. Finally, scans of devices bonded to copper heat sinks with Au-Sn and Pb-Sn solders are presented, showing the different bonding stress distributions. A scan of an unbonded device of the same type reveals stresses due to metallization and/or epitaxial layers.

4.3.1 Ridge Waveguide Laser Active Region

Figure 4.4 shows a scanning electron micrograph of the active region of a GaAs/AlGaAs ridge waveguide quantum-well laser. The ridge width is 3 μm, and the structure includes a current-confining oxide. Figures 4.5-4.7 show polarization-resolved photoluminescence data obtained near the active region of this device. Figure 4.5(a) shows the intensity polarized in the x direction, L_x, while Fig. 4.5(b) shows L_z. The stepsize between data points is 0.5 μm, and the total scanned area is 50 $\times$ 30 μm. In Figs. 4.5(a) and 4.5(b), the height of the graph above the baseline is proportional to the detected luminescence intensity. The greatest luminescence intensity is observed from the quantum well active layer of the laser. Below the active layer, other epitaxial layers are resolved. $Al_xGa_{1-x}As$ luminescence is not detected for $x > 0.2$ due to the cutoff wavelengths of the cold mirror and filter used, so some epitaxial layers appear dark in Figs. 4.5(a) and 4.5(b). The spatial resolution of less than 1 μm FWHM is evident from the thickness of the active layer image. Note that in Fig. 4.5(a), the location of the ridge of the laser is apparent due to a small shoulder on the active layer luminescence (circled

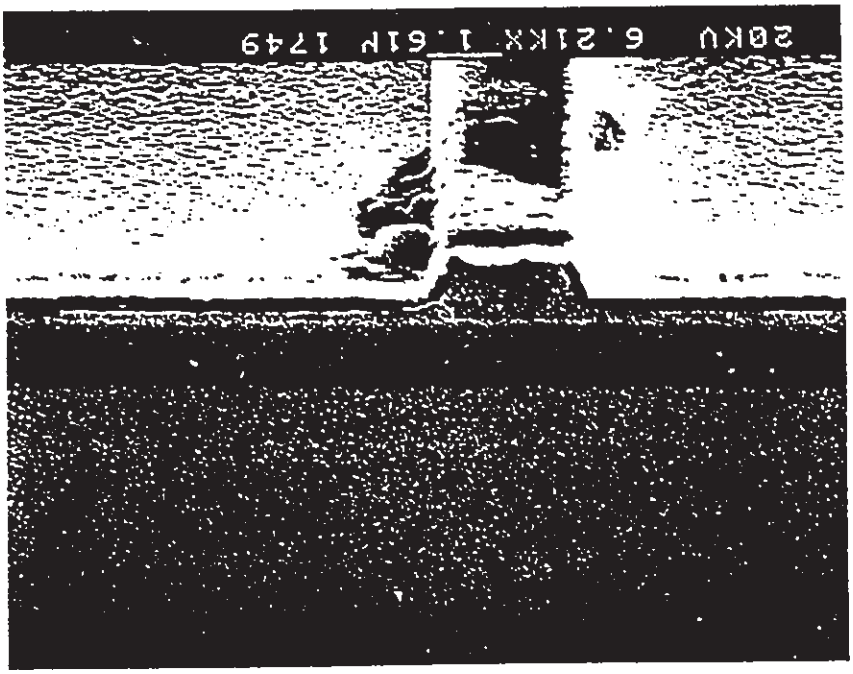

Figure 4.4 An electron micrograph of the ridge of a ridge waveguide diode laser. This laser was scanned using the photoluminescence setup. The ridge is 3 μm wide at the base and 1 μm high.

and inset). Fig. 4.5(b) is shown from a different angle to reveal the substrate and epitaxial layer luminescence under the active layer.

Figure 4.6 shows the distribution of the degree of polarization ρ calculated from the data of Figs. 4.5(a) and 4.5(b) according to Eq. (1). In Fig. 4.6 the height of the graph above the baseline is proportional to ρ; data points above the baseline represent positive values of ρ, and data points below the baseline represent negative values. The value of ρ is undefined when the scan point is off the facet and no signal is present; ρ has been set to zero in this case. The variations in ρ in the substrate material indicate

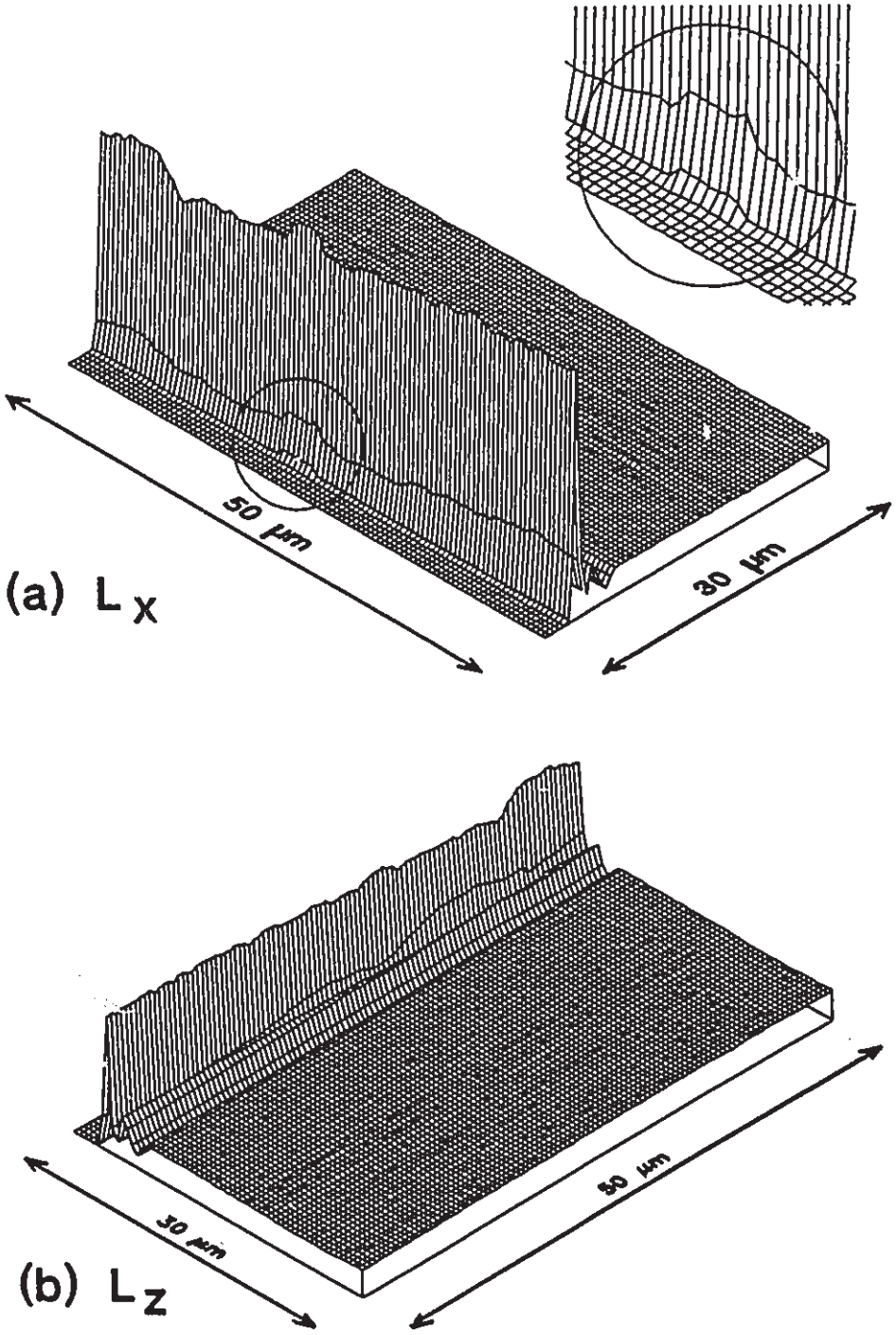

Figure 4.5 The polarization-resolved photoluminescence data obtained near the active region of the ridge waveguide diode laser, (a) L_x, (b) L_z.

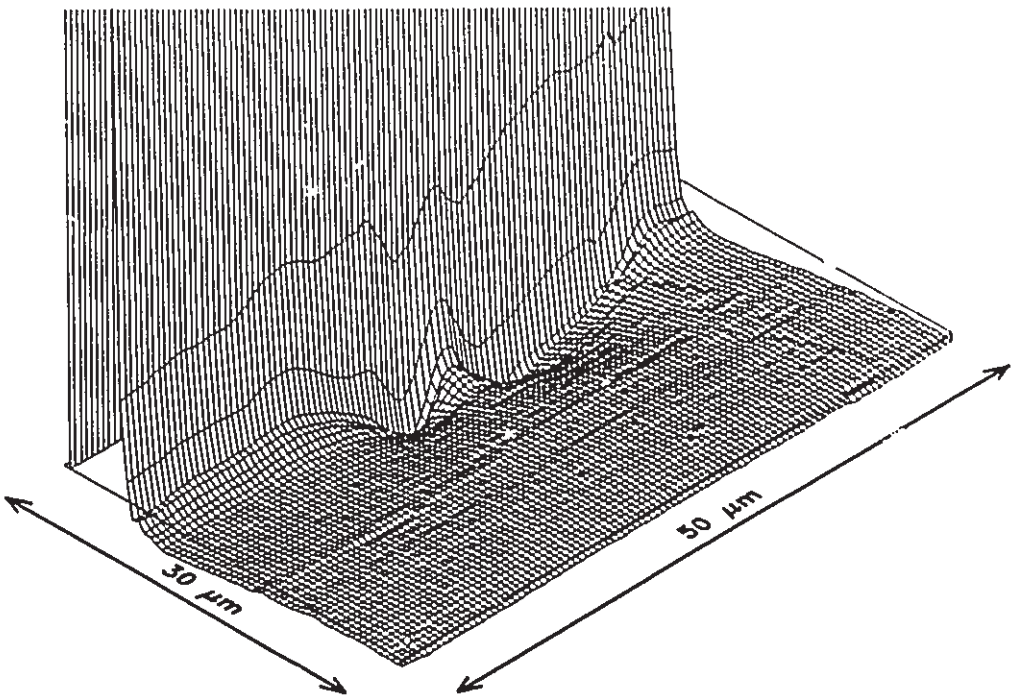

Figure 4.6 The distribution of the degree of polarization for the ridge waveguide laser.

stressed regions near the ridge structure, according to Eq. (2). The quantum well structure of the active layer causes its luminescence to be highly polarized even in the absence of stress, evident from a comparison of Figs. 4.5(a) and 4.5(b), so ρ is offscale in Fig. 4.6 for the active layer. The variations in ρ indicate a peak stress of σ_{xx} = 2.5×10^8 dyn/cm^2 in the substrate near the ridge waveguide, based on the value of K_σ determined later. The center of the stressed area in Fig. 4.6 lies directly below the location of the ridge visible in Fig. 4.5(a).

Fig. 4.7 is an image of the same data as Fig. 4.6, shaded to resemble the stress fringes of photoelastic measurements [75]. The shading at each point is assigned according to

$$I = \cos^2(\pi\rho/\rho_0) \tag{61}$$

where I is the 'intensity' of the shading (0=black, 1=white) and ρ_0 is the increment in ρ between 'fringes'. In Fig. 4.7, the fringe spacing is $\rho_0 = 0.005$. The fringes represent lines of equal values of ρ, similar to contour lines in a contour plot. The numbers in Fig. 4.7 denote the fringe order; the fringe of order 1 would indicate a value of $\rho = \rho_0$, the fringe of order 2 indicates $\rho = 2\rho_0$, and so on. For points of the image which lie between data points, the value of ρ was interpolated before assigning the shading to produce a smoother image. It is to be noted that photoelastic stress fringes indicate a stress difference $(\sigma_{xx}-\sigma_{zz})$ similar to polarization-resolved photoluminescence,

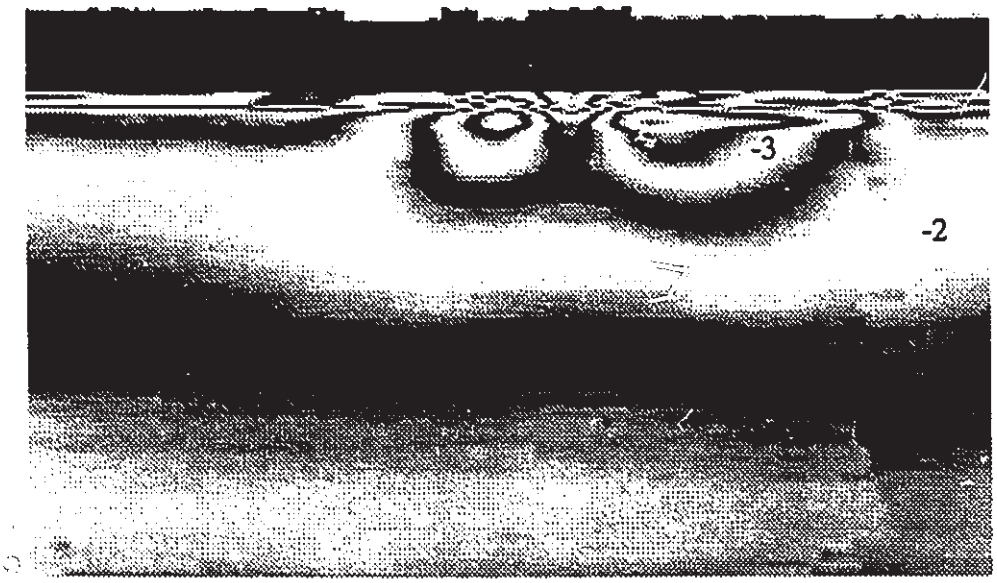

Figure 4.7 An image of the degree of polarization data of Fig. 4.6, shaded to resemble the stress fringes of photoelastic measurements.

so that similar stress distributions should yield similar images for the two measurement techniques.

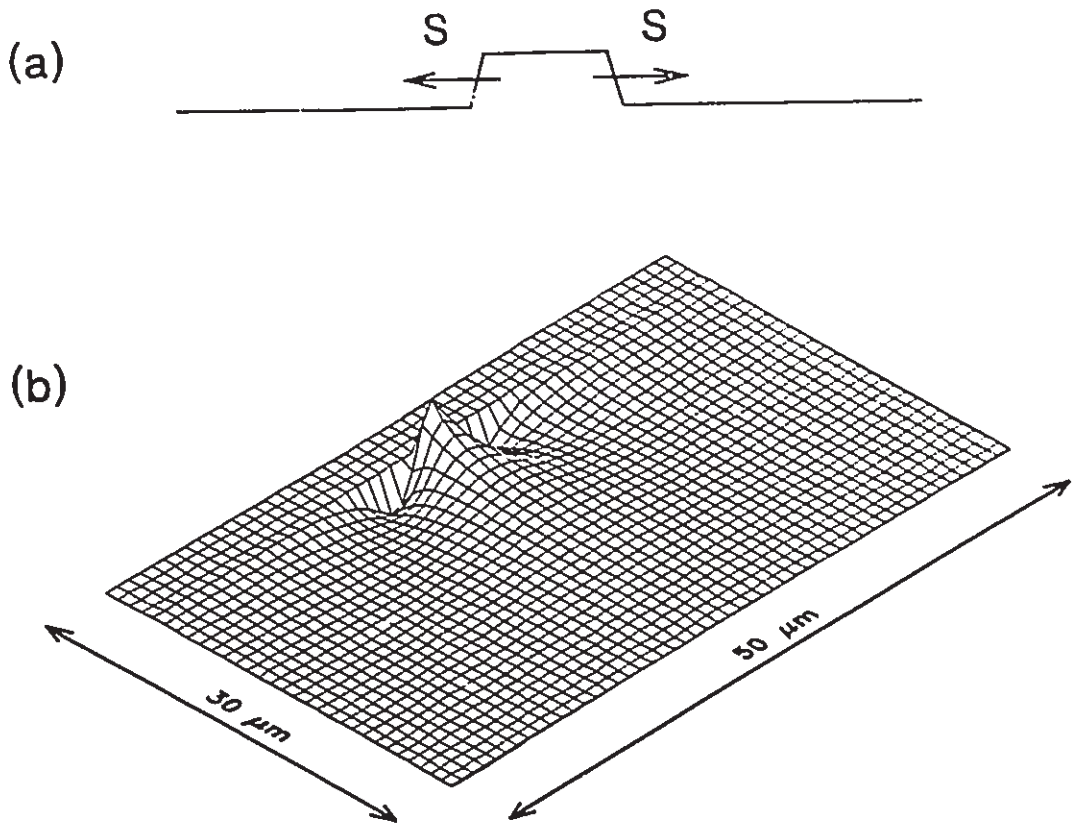

Figure 4.8 (a) The assumed forces acting on the edges of the ridge. (b) The calculated distribution of ρ due to the forces assumed in (a). Note the similarity to Fig. 4.6.

Figure 4.8(a) shows the assumed forces exerted by the ridge on the substrate. An outward-acting force of $S = 2\times10^5$ dyn/cm is assumed along the edges of the ridge. A force of this magnitude corresponds roughly to the force exerted at the edge of a 2000 Å thick layer of SiO_2/Si_3N_4 deposited onto GaAs [20], and could also be caused by metallization layers or slightly mismatched epitaxial layers. Figure 4.8(b) shows a calculated distribution of ρ beneath a 3 μm wide ridge, assuming that the stress-causing force is as shown in Fig. 4.8(a). The data of Fig. 4.8(b) was calculated over the same 50 × 30 μm area as the data of Fig. 4.6, and the vertical scale is the same as for Fig.

4.6. The calculation of stresses was done using equations presented by Kirkby et. al. [20] for the solution of stresses under an oxide stripe window. Isotropy was assumed, and the values chosen for the elastic constants of GaAs were as given by Kirkby et. al. Virtually identical results were obtained using formulae presented by Saada [47] for a tangential line force on the surface of an isotropic, semi-infinite material. The formulae presented by Saada are much simpler and are independent of the elastic constants of the material. It was assumed that the forces were applied at the planar surface of a semi-infinite medium; the presence of the ridge was not considered in performing the stress calculations. The values of ρ were assigned according to Eq. (2), with σ_{xx} and σ_{zz} calculated according to the equations presented by Kirkby et. al., and $K_\sigma = -5.1\times10^{-11}$ cm^2/dyn as determined in the next section. In Fig. 4.8(b), the top surface of the laser corresponds to the upper left edge of the figure. The calculated values of ρ were set to zero for points which are closer than 3 μm to the surface of the laser, since variations in the measured values of ρ in this region of the real device are obscured by the highly-polarized active layer luminescence. Also, the calculated values of ρ tend to infinity near the points of application of force, which will not happen in the real case since the force is not applied at infinitesimal points. The calculated distribution of ρ is very similar to the distribution observed in Fig. 4.6, supporting the claim that Fig. 4.6 represents a measurement of the stresses in the substrate due to the ridge structure, and suggesting that the force exerted at the edges of the ridge is about 2×10^5 dyn/cm.

If the lattice mismatch between the AlGaAs ridge and the GaAs substrate is causing the active region stress, the compressive strain in the ridge is about ϵ =

$-S(1-\nu)/Ed = -0.0016$, where $d = 1\ \mu m = 10^{-4}$ cm and $E/(1-\nu) = 1.2\times10^{12}$ dyn/cm^2 for GaAs. The mismatch strain for $Al_xGa_{1-x}As$ is about $-0.0013x$ [76], or about -0.0010 when $x = 0.75$ as in the ridge of this device [77], so it seems that the mismatch strain is not sufficient to account for the observed stresses. Other contributions may come from the current-blocking oxide (although it is expected that this stress is of the wrong sign [20]) or the metallization layers. It may be possible to reduce the lattice mismatch in the ridge layer by using a quaternary material which is better lattice-matched to GaAs, such as $Al_{.75}Ga_{.25}As_{.995}P_{.005}$. The stresses due to the oxide and metallization layers could be reduced by using different materials and different layer thicknesses [20],[24].

Figure 4.9(a) shows the degree of polarization data from another type of ridge waveguide laser in which the ridge was formed by etching two channels, one on each side of the ridge. Figure 4.9(b) shows the assumed forces of $S = 2\times10^5$ dyn/cm acting on the edges of each channel. Figure 4.9(c) shows the calculated distribution of ρ assuming the forces shown in Fig. 4.9(b). The calculated distribution resembles the measured distribution closely. It is interesting that the two diodes of Figs. 4.6 and 4.9, made using different techniques by different manufacturers, have active region stresses which can be modelled by similar forces at the edges of the ridges and grooves. The stress-causing factors may be the same in the two devices. If the stress-causing factors could be positively identified and the processing modified to reduce the stress, a more reliable device may result. This would be an important topic for future work.

It is worth mentioning here that the stresses induced near a ridge or oxide stripe

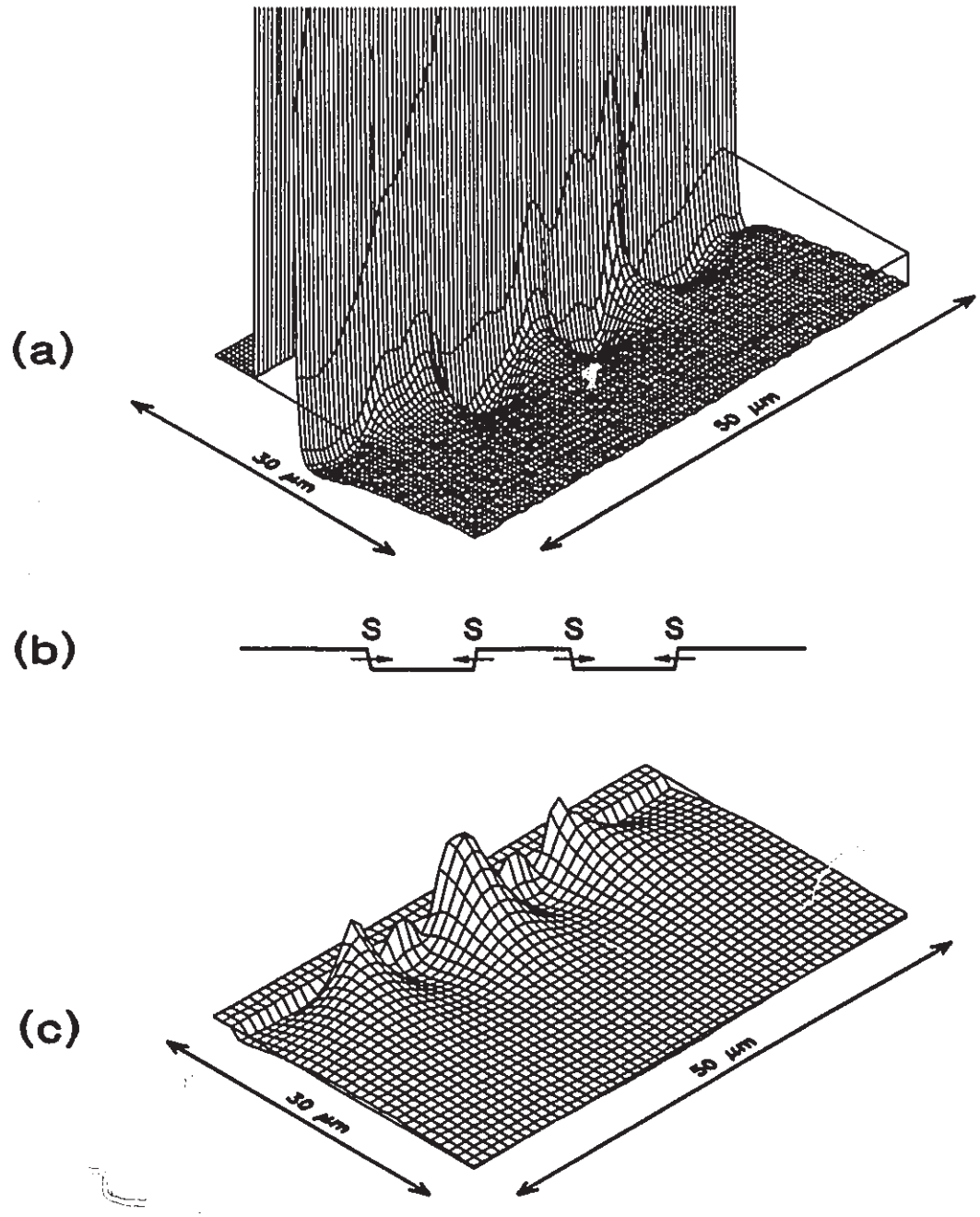

Figure 4.9 (a) The distribution of ρ for a ridge waveguide diode laser with etched channels. (b) The assumed forces on the channel edges. (c) The calculated distribution of ρ.

can affect the refractive index profile near the laser active region due to the photoelastic effect. This can affect the waveguiding properties of the active region in unwanted or unintended ways [20]. Polarization-resolved photoluminescence is capable of measuring the stresses, and given the stresses, the refractive index profile can be determined. Polarization-resolved photoluminescence is therefore a useful tool for investigating stress-induced waveguiding properties of various structures.

4.3.2 Calibration

To determine the value of the constant K_a for GaAs, a GaAs-based diode laser bar (consisting of 16 lasers side by side, not yet cut into individual lasers) was placed supported at two points 2.45 mm apart, and a force was applied to the top surface of the laser bar using a spherically-tipped probe (radius of curvature about 50 μm) as shown in Fig. 4.10. This induced a bending stress in the device, creating a tensile stress $+\sigma_{xx}$ on the lower surface and a compressive stress $-\sigma_{xx}$ on the upper surface. Because of the high length-to-thickness ratio of the laser bar (23:1), contact stresses (σ_{zz}) are negligible.

Figure 4.11 shows the measurements of the distribution of ρ over the edge of the diode laser bar (the laser facets) (a) with no applied force, (b) with an applied force of 0.075 N on the probe, and (c) with an applied force of 0.156 N. The total scanned area in each case is 2.80 mm (wide) x 0.144 mm (high). The vertical scale of each image is expanded 10 times relative to the horizontal scale for clarity. The stepsize is 40 μm horizontally and 4 μm vertically. The fringe spacing is $\rho_0 = 0.01$ in each case. In Figs. 4.11(b) and 4.11(c), the tensile stress $+\sigma_{xx}$ near the bottom of the bar decreases ρ, and

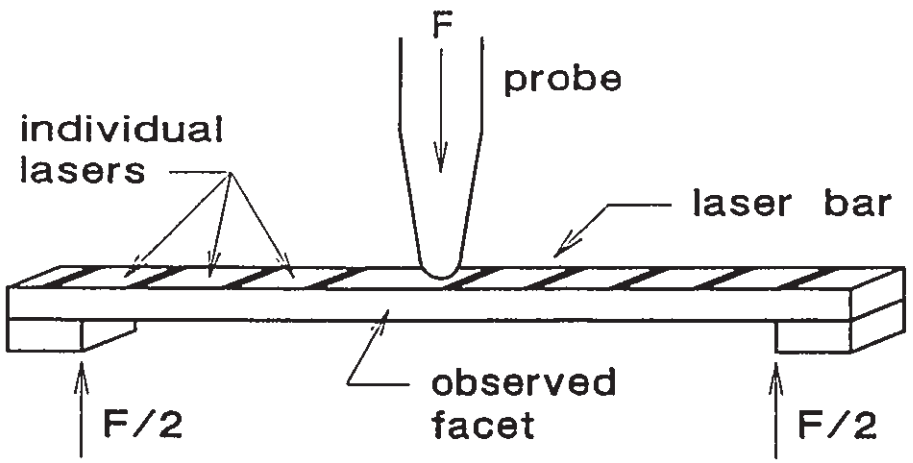

Figure 4.10 The constant K_a was determined by applying a known force to a diode laser bar.

the compressive stress $-\sigma_{xx}$ near the top of the bar increases ρ, and the observed values of ρ increase linearly with applied stress. Note in Fig. 4.11(a) that nine stressed areas along the upper (active) surface due to breaks about 35 μm wide in the metallization layer between diodes (shown in Fig. 4.10) can be resolved. Metallization layers are therefore capable of inducing significant stresses, in this case $\sigma_{xx} \approx 2\times10^8$ dyn/cm^2. Weaker stress distibutions due to the ridge structures of the active regions are evident midway between the breaks in metallization; the stresses near the ridges also reach about 2×10^8 dyn/cm^2 (not evident in a scan of this scale), but the extent of these stress distributions is less due to the smaller width of the ridges (about 4 μm).

Figure 4.11(d) shows a theoretical calculation of the distribution of ρ for a simply-supported rectangular beam, with σ calculated using [61]

$$\sigma_{xx} = \frac{6F}{wh^3}\left(\frac{L}{2} - |x|\right) z \qquad (62)$$

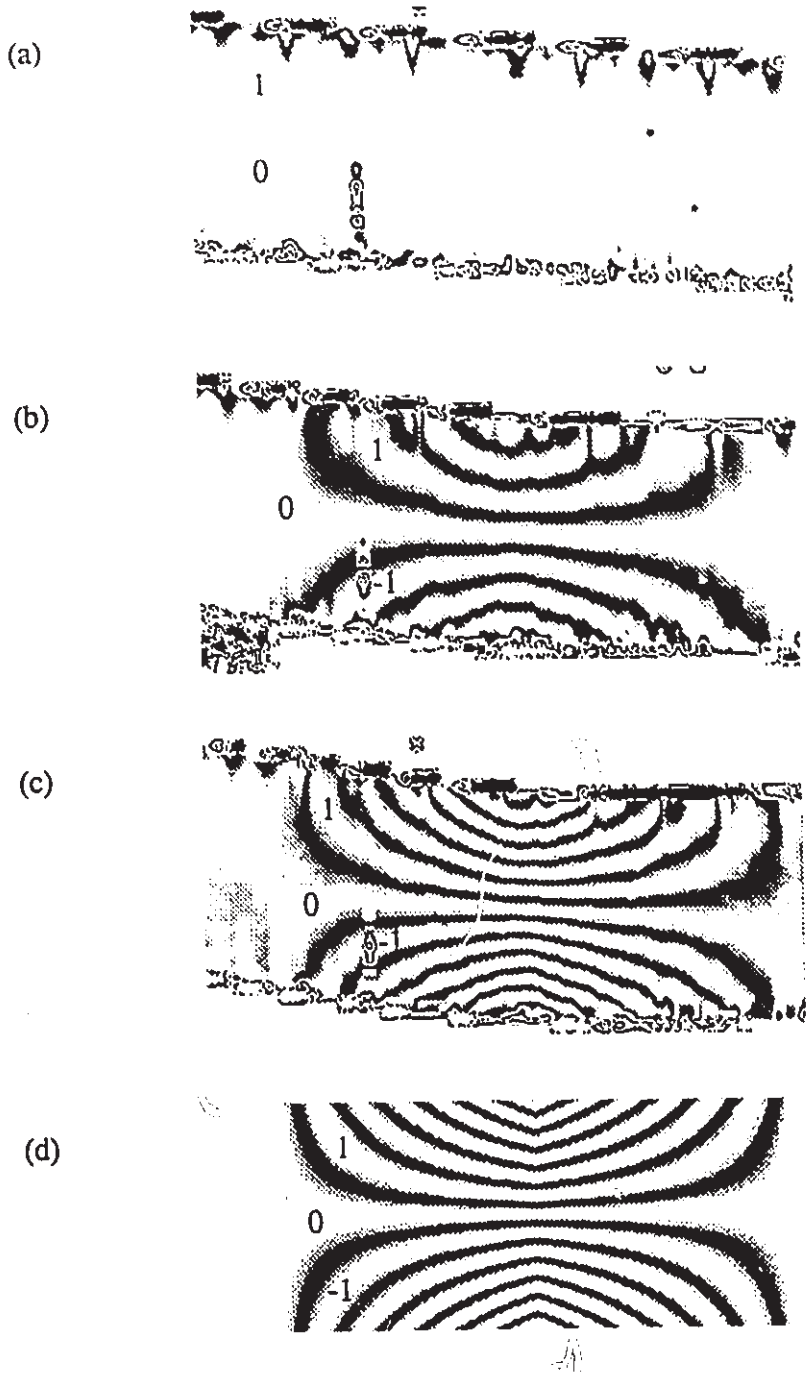

Figure 4.11 Images of the distribution of ρ for the diode laser bar with (a) F = 0, (b) F = 0.075 N, and (c) F = 0.156 N, and (d) a calculation for F = 0.156 N. The fringe spacing is $\rho_0 = 0.01$.

and $\sigma_{zz} = 0$, where F is the applied force (0.156 ± 0.004 N), w is the width of the beam (400 ± 10 μm), h is the thickness (108 ± 2 μm), and L is the length (2.45 ± 0.05 mm), and the origin is at the center of the beam. The value of K_σ in Eq. (2) was adjusted for the best correspondence between Figs. 4.11(c) and 4.11(d), giving $K_\sigma = -(5.1 \pm 0.3)\times 10^{-11}$ cm^2/dyn. This value of K_σ corresponds reasonably with the value of $-(4.4 \pm 0.6)\times 10^{-11}$ cm^2/dyn reported for electroluminescence in Chapter 3.

A rough double-check of the applied stress is provided by the observed deflection of the laser bar under stress. The deflection at the center of a narrow rectangular beam is given by [61]

$$\delta = \frac{FL^3}{4Ewh^3} \tag{63}$$

where E is Young's Modulus. For the crystal orientation of the current experiment (see Fig. 4.2) and uniaxial stress applied parallel to the x axis, the effective value of $1/E$ is $\delta\epsilon_{xx}/\delta\sigma_{xx} = (s_{11}+s_{12}+s_{44}/2)/2$, where $s_{11} = 1.173\times 10^{-12}$ cm^2/dyn, $s_{12} = -0.366\times 10^{-12}$ cm^2/dyn, and $s_{44} = 1.684\times 10^{-12}$ cm^2/dyn are the elastic compliances of GaAs [68]. This yields an effective value of $E = 1.21\times 10^{12}$ dyn/cm^2. Note that for the case of bending of a thin plate, which may be closer to the present situation, we must have $\epsilon_{yy} = 0$. This causes E in (63) to be replaced by $E/(1-\nu^2)$. However, the effective value of ν for uniaxial stress applied parallel to the x axis is given by $-\delta\epsilon_{yy}/\delta\epsilon_{xx} = -(s_{11}+s_{12}-s_{44}/2)/(s_{11}+s_{12}+s_{44}/2) = 0.021$, so $(1-\nu^2) \approx 1$ and the expected deflection is essentially the same. This result also means that the stresses at the facets of the laser bar represent the stresses throughout the width of the bar. A deflection of 9.4 μm is

expected with an applied force of 0.156 N, and the observed deflection in Fig. 4.11(c) is 10 ± 1 μm.

To determine the value of K_a for InP, a piece of semi-insulating InP 4 mm long, 0.93 mm wide, and 0.34 mm thick was cleaved from a wafer. The beam-bending experiment was performed by scanning the cleaved facet, as for the GaAs diode laser bar. The resulting value of K_a was $-(9.4 \pm 1.0)\times10^{-11}$ cm^2/dyn, about twice the value for GaAs. This sample was also turned on its side so that the polished (001) surface was scanned, making the analyzing axes correspond to the [110] and [1$\bar{1}$0] crystal directions. In this case the value of K_a was $-(4.6 \pm 1.0)\times10^{-11}$ cm^2/dyn, indicating a large degree of anisotropy in InP for the two crystal orientations. The tensor analysis of Section 2.2 suggests that the value $K_{aav} = -9.4\times10^{-11}$ cm^{2}dyn should be used when the isotropic assumption is to be used, since the value for this crystal orientation should represent the average of the upper and lower bounds of K_a for all crystal orientations.

To obtain a comparison of polarization-resolved photoluminescence with another strain measurement technique, a comparision was made with an X-ray diffraction measurement of a strained epitaxial layer. The sample consisted of a 3 μm thick layer of GaAsP grown by molecular-beam epitaxy (MBE) on a GaAs substrate (sample MBE-210). The phosphorus was present at a low concentration as a contaminant in the grown layer, causing a slight lattice mismatch. The cleaved facet of the sample was scanned using polarization-resolved photoluminescence, revealing a difference in degree of polarization of $\delta\rho = -0.002 \pm 0.0005$ between the epitaxial layer and the substrate. Using $K_a = -5.1\times10^{-11}$ cm^2/dyn, this indicates a tensile stress of about $\sigma_{xx} = (4 \pm$

$1)\times10^7$ dyn/cm^2, or a strain of about $(3.4 \pm 1.0)\times10^{-5}$, in the epitaxial layer. The X-ray diffraction rocking curve showed the epitaxial layer diffraction peak offset by about 18 $\pm$ 4 arc seconds from the substrate peak, indicating a tensile strain in the epitaxial layer of about $(4 \pm 1)\times10^{-5}$. The value of K_a obtained by the beam-bending experiment therefore appears to be reasonable.

4.3.3 Bonding Stresses

Figure 4.12 shows scans of gain-guided oxide-stripe diodes (4 μm stripe width) bonded to Cu heat sinks with (a) Au-Sn solder (80% Au, 20% Sn by weight) and (b) In solder, and (c) an unbonded diode of the same type. The bonding of these devices was done by EG&G Optoelectronics. The scanned area is 400 $\times$ 100 μm^2 and the stepsizes are 4 μm horizontally and 2 μm vertically in each case, and the fringe spacing is ρ_0 = 0.01. The diodes in Figs. 4.12(a) and 4.12(b) had been bonded two months prior to taking these scans and life-tested for two weeks at 50°C, so some relaxation of the bonding stress has undoubtedly occurred, as observed in Section 3.5. Nevertheless, there is a large compressive stress throughout the AuSn-bonded device, greatest near the bonded surface, with a peak value of about $\sigma_{xx} = -2.0\times10^9$ dyn/cm^2. This is consistent with the bonding stress of $-(1.96 \pm 0.12)\times10^9$ dyn/cm^2 measured for this device using electroluminescence (Section 3.4). The stress is much lower for the device of Fig. 4.12(b) bonded with the softer In solder, and reaches a maximum value of about -2.5×10^8 dyn/cm^2 near the bonded surface. The stresses in the unbonded diode of Fig. 4.12(c) appear to be due to the metallization and epitaxial layers. In Fig. 4.12(c),

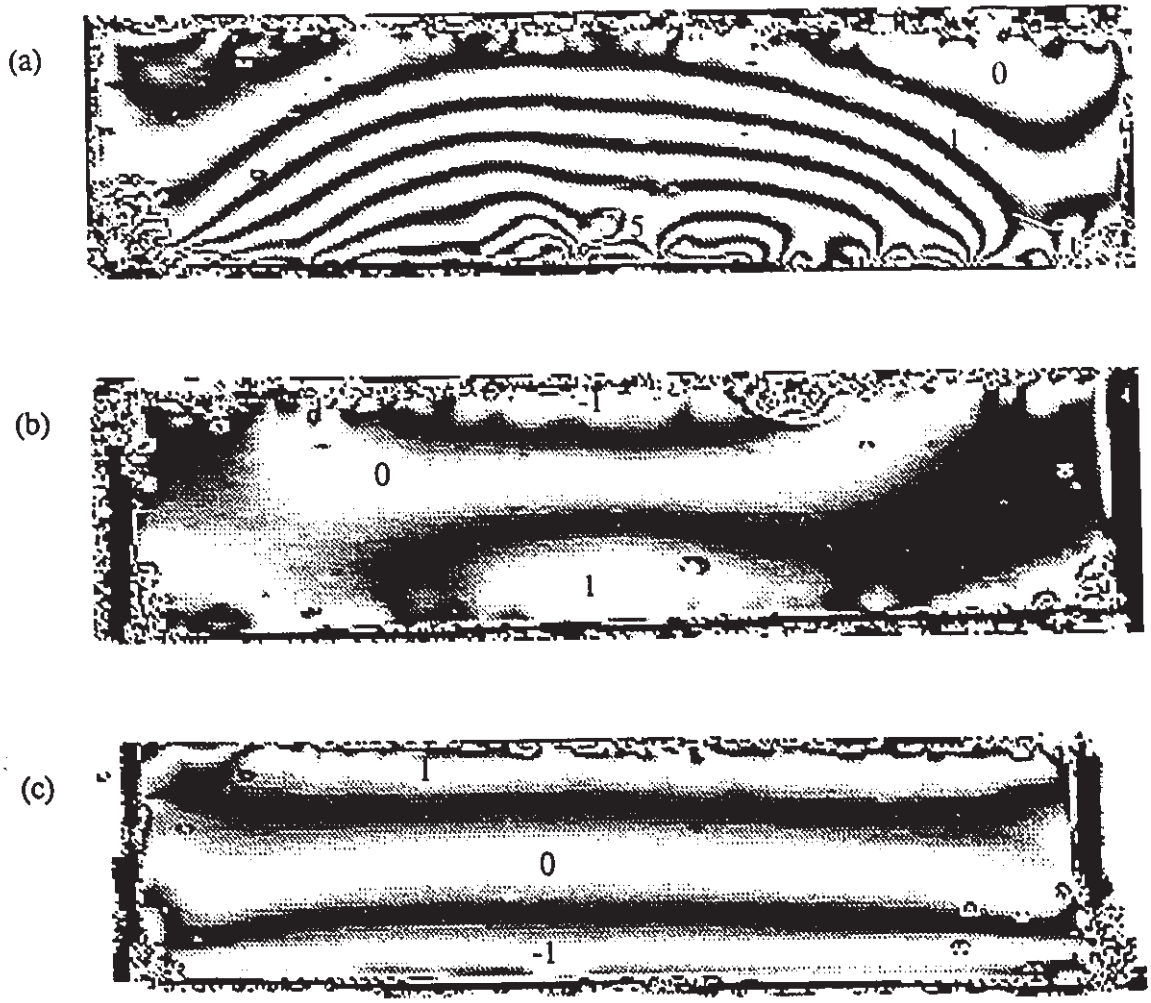

Figure 4.12 Images of ρ for diodes bonded to Cu heat sinks with (a) Au-Sn solder, (b) In solder, and (c) an unbonded diode. The fringe spacing is $\rho_0 = 0.01$.

$\sigma_{xx} = 0$ near the center of the chip, and σ_{xx} reaches about 2×10^8 dyn/cm^2 at the active (lower) surface and about -2×10^8 dyn/cm^2 at the upper surface. The difference in stress between the active layer of the In-bonded device and the active layer of the unbonded device is about -4.5×10^8 dyn/cm^2, which agrees reasonably with the bonding stress of $-(5.5 \pm 1.5)\times10^8$ dyn/cm^2 measured for this In-bonded device using electroluminescence.

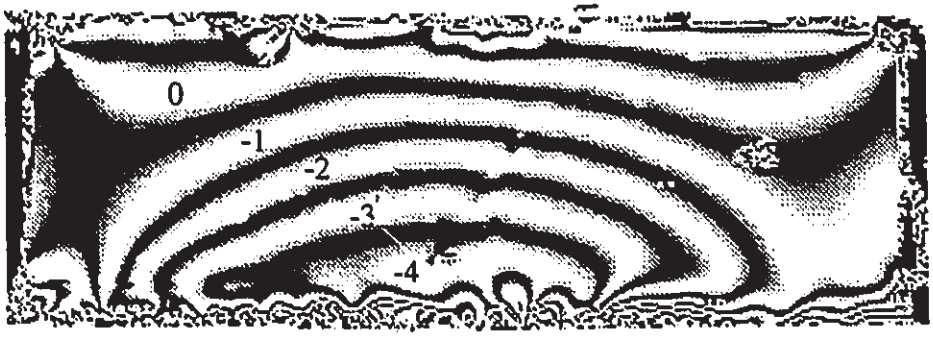

Figure 4.13 An image of ρ for an InGaAsP/InP diode laser bonded active-side up to a diamond heat sink with Au-Sn solder. The fringe spacing is $\rho_0 = 0.01$.

Fig. 4.13 shows the stress distribution for an InGaAsP/InP diode laser bonded active side up to a diamond heat sink using Au-Sn solder. The bonding stress reaches a peak value of $\sigma_{xx} = 5\times10^8$ dyn/cm^2 (tensile) near the bonded (lower) surface. The tensile stress is expected due to the low thermal expansion coefficient of diamond, but the magnitude of the stress is smaller than that of the GaAs devices bonded to copper or diamond heat sinks with Au-Sn solder. The difference in thermal expansion coefficients between InP ($\alpha = 4.56\times10^{-6}$ C^{-1} [68]) and diamond ($\alpha = 1.0\times10^{-6}$ C^{-1} [66]) is less than the difference between GaAs ($\alpha = 5.73\times10^{-6}$ C^{-1} [62]) and diamond, so it is reasonable that the bonding stress would be smaller for InP. Using the values $E = 6.07\times10^{11}$ dyn/cm^2 and $\nu = 0.36$ [68] and $\delta T = -253$°C between the Au-Sn solder

melting point and room temperature, the maximum bonding stress expected for InP on diamond is $\sigma_{xx} = E\Delta\alpha\delta T/(1-\nu) = 5.5\times10^8$ dyn/cm^2, so a measured value of 5×10^8 dyn/cm^2 is reasonable.

4.4 Summary

Stresses on the facets of GaAs and InP based diode lasers have been imaged to a spatial resolution of 1 μm and a stress resolution of 10^7 dyn/cm^2 or better using polarization-resolved photoluminescence. This technique enables the investigation of stresses induced during processing of diode lasers, due to ridge structures, oxide and metallization layers, lattice mismatch, and bonding. The sensitivity of the technique is sufficient to detect easily stresses of about 10^8 dyn/cm^2 which have been reported to cause increased degradation rates in GaAs/AlGaAs diode lasers, and stresses exceeding this value have been observed in several devices. It should be possible to use polarization-resolved photoluminescence to identify the role of mechanical stress in device degradation, and to assist in the reduction of stresses induced during the manufacture and bonding of semiconductor lasers, with the possible benefit of longer device lifetime.

Chapter 5. Dislocation Detection

5.1 Introduction

Dislocations in semiconductor electronic and opto-electronic devices can be expected to impair the device performance. Dislocations reduce the mobility of the free carriers and create generation/recombination centers in p-n junctions [78], and contribute to rapid degradation of III-V semiconductor opto-electronic devices [10]. It is therefore important to be able to detect dislocations in the semiconductor material, to ensure good substrate quality and to adjust growth and fabrication processes to discourage the formation of dislocations. Many techniques currently in use for detecting individual dislocations in semiconductors, such as chemical etching, decoration, and transmission electron microscopy [37], are destructive and therefore not suitable for routine monitoring of substrate material or epitaxial layers before processing. X-ray topography techniques provide clear images of dislocations [38], but are extremely sensitive to macroscopic stresses and thus may not be suitable for examining wafers after epitaxial growth or other processing. Infrared transmission microscopy has revealed dislocations in n-type GaAs [79], probably due to an impurity decoration effect, but it must be determined by comparison with other techniques whether all dislocations are detected for a particular material. Images of photoluminescence intensity [80], cathodo-luminescence intensity [81], or electron beam induced current (EBIC) [82] reveal

dark lines along misfit dislocations in epitaxial layers, but information about the dislocation Burgers vector cannot be obtained, and it is difficult to discriminate between the dark spots of threading dislocations intersecting the surface and dark spots due to contamination or other defects. Similar disadvantages apply to Nomarski optical microscopy of surface morphology [83]. Infrared birefringence measured in transmission can detect stresses due to individual dislocations in semiconductors and can determine the Burgers vector [39,40], but the sample must be about 1 mm thick with a polished back surface and with the dislocations running perpendicular to the surface, which limits its general use.

In this chapter it is demonstrated that the spatial resolution of 1 μm and the stress resolution of 3×10^{6} dyn/cm^{2} (strain resolution 3×10^{-6}) are sufficient to allow polarization-resolved photoluminescence to detect the stress fields due to individual dislocations. Since it is essentially a surface technique, it can detect dislocations which intersect the surface from any angle, and dislocations in epitaxial layers. Different dislocation types produce different patterns of surface stresses, so the dislocation direction and Burgers vector can be determined from the stress patterns. Polarization-resolved photoluminescence does not require special sample preparation such as back surface polishing as required by infrared transmission techniques, or chemical etching as is often required by X-ray diffraction techniques. Measurements of photoluminescence intensity are often done at low temperatures, which complicates the experimental setup. Polarization-resolved photoluminescence, on the other hand, provides sensitive dislocation detection at room temperature. It appears that polarization-resolved

photoluminescence will be a useful tool for routine checking of substrate quality, checking of growth quality in epitaxial layers, and basic research into dislocation formation and structure.

The experimental setup is the same as that used in Chapter 4 and illustrated in Fig. 4.1. However, it is the usual convention when analyzing dislocations intersecting a free surface to denote the free surface as the plane $z=0$ with the (semi-infinite) material occupying the region $z<0$. Therefore, in this chapter, the degree of polarization is defined to be

$$\rho = \frac{L_x - L_y}{L_x + L_y} \tag{64}$$

where L_x and L_y are the detected luminescence intensities polarized in the x and y directions respectively, so that the observed surface is the plane $z=0$. The x, y, and z coordinates of this chapter correspond to the x, z, and $-y$ coordinates respectively of previous chapters. In this chapter, the observed surface of the sample is the top surface of the semiconductor wafer, while in Chapters 3 and 4 the cleaved facet was observed. Therefore in both cases the top surface of the wafer corresponds to a surface of constant z, so a consistent coordinate system is maintained for the sample itself.

Assuming that the sample material is isotropic, the degree of polarization is then given by

$$\rho(x,y) = K_o[\sigma_{xx}(x,y) - \sigma_{yy}(x,y)] \tag{65}$$

where K_o is a constant and $\sigma_{xx}(x,y)$ and $\sigma_{yy}(x,y)$ are the stress distributions on the sample

surface. A second independent measurement can be made by rotating the sample 45 degrees clockwise. If the coordinate system (x,y,z) rotates with the sample and the coordinate system (x',y',z') remains fixed to the measuring apparatus, the distribution of ρ is now given by

$$\rho(x',y') = 2K_a\sigma_{xy}(x,y) \tag{66}$$

where $x = (x'-y')/\sqrt{2}$ and $y = (x'+y')/\sqrt{2}$. The coordinate axes and the corresponding crystal directions are illustrated in Fig. 5.1 for (001) oriented samples, as used in the experiments reported in this thesis. Thus, polarization-resolved photoluminescence can determine the distributions of $(\sigma_{xx}-\sigma_{yy})$ and σ_{xy} on the sample surface. In the isotropic

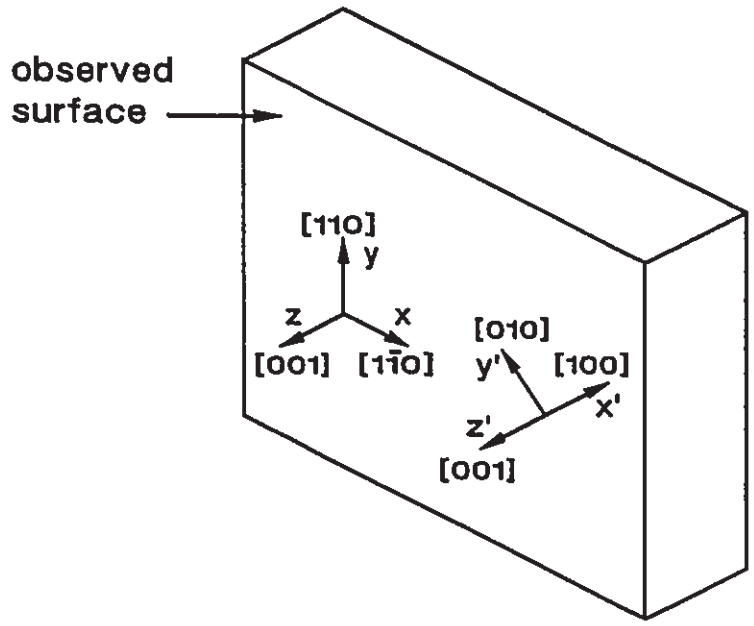

Figure 5.1 The coordinate axes and crystal directions with respect to the observed surface.

case, the stress components σ_{xz}, σ_{yz}, and σ_{zz} do not contribute to the degree of polarization; this does not represent a shortage of stress information since these stress components are known to be zero at a free surface.

The measurements of K_a reported in Chapter 4 suggest that the value of K_a varies depending on the crystal orientation. To keep the calculation of the dislocation stresses and ρ down to a reasonable level of complexity, the isotropic approximation was used and the measured average value for InP of $K_{aav} = -(9.4 \pm 1.0)\times 10^{-11}$ cm^2/dyn. Using the isotropic assumption produced reasonable results, supporting its validity.

Two types of dislocations were studied in these experiments. Threading dislocations are created in bulk material during growth of the semiconductor crystal, and were observed where they intersect the sample surface. Misfit dislocations are caused when the thickness of a strained epitaxial layer exceeds the critical thickness, and run along the interface between the epitaxial layer and the substrate material. Although the misfit dislocations do not intersect the surface, they are sufficiently close to the surface that significant surface stresses are induced. Observations of threading dislocations are reported in Section 5.2, and observations of misfit dislocations are discussed in Section 5.3.

5.2 Threading dislocations intersecting the surface

A dislocation is characterized by its direction and its Burgers vector. Figure 5.2 illustrates a dislocation in a cubic crystal. At the dislocation, indicated by the symbol

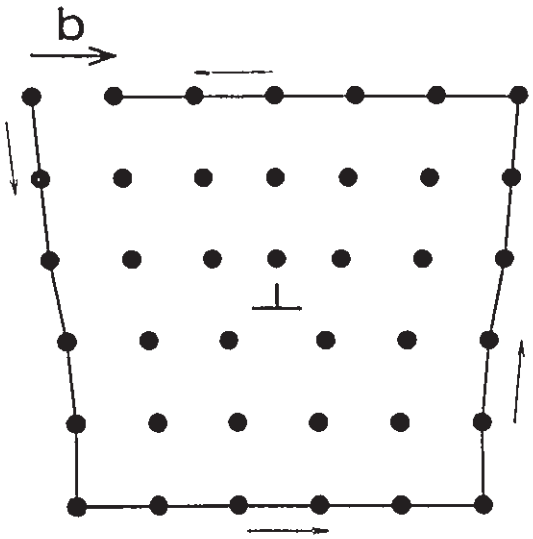

Figure 5.2 An edge dislocation in a cubic crystal. The Burgers vector **b** is the residue after making a circuit around the dislocation.

⊥, there is an imperfection in the crystal lattice. The direction of the dislocation is the line along which the imperfect crystal occurs. In the case of Fig. 5.2, the dislocation direction is out of the page. The Burgers vector **b** of the dislocation is determined by tracing a path in the perfect crystal around the dislocation, keeping track of the number of atoms passed in each direction. If one attempts to make a closed path by moving five atoms down, five atoms to the left, five atoms up, and five atoms to the right, for example, the end point will not correspond to the starting point if the path encircles a dislocation. The difference between the starting point and the end point is called the Burgers vector. Note that the path is taken in a right-handed sense around the dislocation line. If the dislocation direction is chosen to be in to opposite direction (into the page in the case of Fig. 5.2), the Burgers vector also reverses, which can lead to confusion if the dislocation direction is not assigned consistently. In this thesis, the direction of a

dislocation intersecting a free surface is chosen in the direction of increasing z, i.e., emerging from the material.

If the Burgers vector is perpendicular to the dislocation direction, as in Fig. 5.2, the dislocation is called an edge dislocation. A screw dislocation has its Burgers vector parallel to the dislocation direction. Dislocations can also be mixed, with both edge and screw components, and are then usually identified by the angle between the Burgers vector and the dislocation direction. For example, a 60 degree dislocation is common in zincblende type crystals such as GaAs and InP. Dislocations tend to have directions which follow crystallographic directions (usually $<110>$ type directions in zincblende type crystals), but in general there is no limitation on the dislocation direction. The Burgers vector, however, must be a vector joining two identical atoms of the crystal, and hence must lie along a crystallographic direction.

Several authors have approached the problem of calculating the stresses around a long, straight dislocation in an isotropic material. Hirth and Lothe [84] give the stresses due to a straight dislocation in an infinite material. Honda [85] gives the stresses due to a dislocation intersecting a free surface at normal incidence, and Shaibani and Hazzledine [86] give the stresses for a dislocation intersecting a free surface at an arbitrary angle. These formulae give the stress field throughout the semi-infinite material, but the present experiments only measure the stress in the material which is within a fraction of a micron of the sample surface, due to the short absorption length of the 633 nm pump light in InP. As long as this sampling depth is much less than the distance from the sampled point to the dislocation ($|z| \ll r$, where $r^2 = x^2+y^2$), the

surface value of the stress ($z=0$) can be used to predict the measured degree of polarization. This considerably simplifies the calculation of the distributions of ρ.

For the case of an edge dislocation at normal incidence (parallel to the z axis), the surface values of the stresses $(\sigma_{xx}-\sigma_{yy})$ and σ_{xy} are simply $(1+2\nu)(1-\nu)$ times the values far from the surface (an increase of about 12 percent for $\nu \approx 0.3$). For the edge component of the Burgers vector b_e along the x axis, the resulting surface stresses are given by

$$\sigma_{xx}(x,y)-\sigma_{yy}(x,y) = -\frac{2\mu b_e(1+2\nu)}{\pi} \cdot \frac{x^2 y}{(x^2+y^2)^2}$$
$$\sigma_{xy}(x,y) = \frac{\mu b_e(1+2\nu)}{2\pi} \cdot \frac{x(x^2-y^2)}{(x^2+y^2)^2} \qquad (67)$$

For a screw dislocation parallel to the z axis in an infinite material, $\sigma_{xx} = \sigma_{yy} = \sigma_{xy} = 0$. However, a screw dislocation intersecting a free surface at normal incidence induces surface stresses $(\sigma_{xx}-\sigma_{yy})$ and σ_{xy} of similar magnitude to those of an edge dislocation. If the screw component of the Burgers vector b_s is in the $+z$ direction, the surface stresses are given by

$$\sigma_{xx}(x,y)-\sigma_{yy}(x,y) = -\frac{2\mu b_s}{\pi} \cdot \frac{xy}{(x^2+y^2)^{3/2}}$$
$$\sigma_{xy}(x,y) = \frac{\mu b_s}{2\pi} \cdot \frac{x^2-y^2}{(x^2+y^2)^{3/2}} \qquad (68)$$

The surface stresses of a mixed dislocation at normal incidence can be calculated by summing the stresses due to the edge and screw components of the Burgers vector.

The formulae of Shaibani and Hazzledine [86] apply to a dislocation lying in the

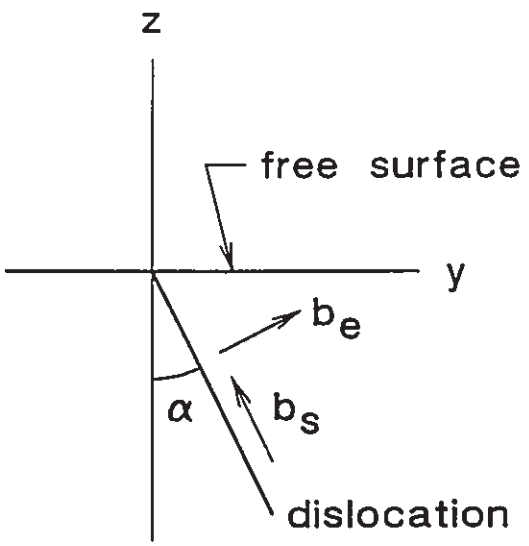

Figure 5.3 The threading dislocation lies in the *yz* plane and makes an angle α with the *z* axis.

yz plane, intersecting the surface at the point (0,0,0) and making an angle α with the normal to the surface as shown in Fig. 5.3. The dislocation Burgers vector is resolved into three components: b_s, which lies along the dislocation direction; b_e, which lies in the *yz* plane and is perpendicular to the dislocation direction; and b_x which lies in the *x* direction (out of the page in Fig. 5.3). When evaluated at the free surface (z=0), the stress formulae of Shaibani and Hazzledine [86] reduce to the following:

$$\sigma_{xx}(x,y) = \frac{\mu b_s}{2\pi}\left[M_s x^2 + \frac{2(1-\nu)x\sin 2\alpha}{RB} - \frac{2xy\cos^3\alpha}{RB^2} + C'x\sin\frac{\alpha}{2}\right]$$
$$+\frac{\mu b_e}{4\pi(1-\nu)}\left[M_e x^2 - \frac{4x\cos^2\alpha}{B^2} - \frac{4(1-\nu)(1-2\nu)x\cos^2\alpha}{RB}\right.$$
$$\left.-\frac{(1-\nu)C'x\cos\alpha}{\cos(\alpha/2)}\right]$$
$$+\frac{\mu b_x}{4\pi(1-\nu)}\left[M_x x^2 - \frac{2x^2y\cos\alpha}{B^2R^2} - \frac{2y\cos\alpha}{RB} + \frac{2y\cos^3\alpha}{B^2}\right. \quad (69)$$
$$-2\cos\alpha\left\{\frac{2(1-2\nu)y}{RB} - \frac{(1-4\nu)\sin\alpha}{B}\right\}$$
$$+\frac{4(1-\nu)(1-2\nu)(2y-R\sin\alpha)\cos\alpha}{RB}$$
$$\left.+\frac{(1-\nu)C'y}{\cos(\alpha/2)}\right]$$

$$\sigma_{yy}(x,y) = \frac{\mu b_s}{2\pi}\left[M_s y^2 - 2x\sin\alpha\cos\alpha\left(\frac{1}{RB}+\frac{1}{B^2}\right) + \frac{2xy(1+\sin^2\alpha)\cos\alpha}{RB^2}\right.$$
$$\left.-C'x\sin\frac{\alpha}{2}\right]$$
$$+\frac{\mu b_e}{4\pi(1-\nu)}\left[M_e y^2 + 4x\cos^2\alpha\left(\frac{2(1-\nu)}{RB} - \frac{1}{B^2}\right) + \frac{(1-\nu)C'x\cos\alpha}{\cos(\alpha/2)}\right] \quad (70)$$
$$+\frac{\mu b_x}{4\pi(1-\nu)}\left[M_x y^2 - \frac{2y(y-R\sin\alpha)^2\cos\alpha}{R^2B^2} + \frac{2y\cos\alpha}{RB} + \frac{2y\cos^3\alpha}{B^2}\right.$$
$$+\frac{8\nu\sin\alpha\cos\alpha}{B} - \frac{4(1-\nu)(1-2\nu)y\cos\alpha}{RB}$$
$$\left.-\frac{(1-\nu)C'y}{\cos(\alpha/2)}\right]$$

$$\sigma_{xy}(x,y) = \frac{\mu b_s}{2\pi}\left[M_s xy + \frac{(3-4\nu)y\sin\alpha\cos\alpha}{RB} + \frac{\cos\alpha}{R}\left(\frac{2x^2}{B^2}-1\right) + C'y\sin\frac{\alpha}{2}\right]$$
$$+ \frac{\mu b_e}{4\pi(1-\nu)}\left[M_e xy - \frac{8(1-\nu)^2 y\cos^2\alpha}{RB} - \frac{(1-\nu)C'y\cos\alpha}{\cos(\alpha/2)}\right] \qquad (71)$$
$$+ \frac{\mu b_x}{4\pi(1-\nu)}\left[M_x xy - \frac{2xy(y-R\sin\alpha)\cos\alpha}{R^2B^2} + \frac{8\nu(1-\nu)x\cos\alpha}{RB} - \frac{(1-\nu)C'x}{\cos(\alpha/2)}\right]$$

where

$$R^2 = x^2+y^2$$
$$B = R - y\sin\alpha \qquad (72)$$
$$C' = -\frac{2(1-2\nu)\cos\alpha}{R^2\cos(\alpha/2)}\left[1+\frac{2y^2\cos^2(\alpha/2)}{RB}\right]$$

and

$$M_s = -\frac{2x(R+B)\sin\alpha\cos\alpha}{R^3B^2}$$
$$M_e = \frac{4(1-\nu)(R+B)\cos^2\alpha}{R^3B^2} \qquad (73)$$
$$M_x = -\frac{2y\cos\alpha}{R^3B} - 2(1-2\nu)\cos\alpha\left[\frac{y(R+B)}{R^3B^2} - \frac{\sin\alpha}{RB^2}\right]$$

and C' is related to the parameter C of Shaibani and Hazzledine by $C = C'x\sin\alpha$. If the dislocation direction is not in the yz plane, it is necessary to perform a coordinate transformation to place the dislocation in the yz plane, calculate the stresses using Eqs. (69)-(71), and transform the stresses back to the original coordinates. Note that

singularities at $\alpha=0$, such as $\cot(\alpha)$, appear in the formulae of Shaibani and Hazzledine. These singularities have been removed from Eqs. (69)-(71) so that they can be evaluated accurately by computer for small values of α. The following relationships have been used to remove the singularities:

$$\cos\alpha + \frac{y}{R}\sin\alpha - \frac{R}{B} = 2\sin^2(\alpha/2)\left[1 + \frac{2y^2\cos^2(\alpha/2)}{RB}\right]$$

$$\frac{R\cos^2\alpha}{B} + \frac{y\sin\alpha}{B} - 1 = \frac{(2y - R\sin\alpha)\sin\alpha}{B} \qquad (74)$$

$$\left[\frac{1}{R} - \frac{1}{B}\right] = -\frac{y\sin\alpha}{RB}$$

The stress formulae of Eqs. (69)-(71) are quite complicated, even for the special case of evaluating the stresses only at the free surface. Thus it is considered impractical at this time to attempt to calculate the stresses with the additional complication of anisotropic materials.

Computer evaluation of Eqs. (69)-(71) for various dislocation types, using the program DISS.FOR, indicates that all dislocations which intersect the surface will cause surface stresses of similar magnitude if the Burgers vectors are comparable. Different dislocation types produce different patterns of surface stresses, so that the Burgers vector and direction of a dislocation may be determined by matching the observed distribution of ρ with calculated distributions. Because the Burgers vector must lie along a crystallographic direction and the dislocation direction also tends to lie along a crystallographic direction, there are only a finite number of common dislocation types, so the problem of finding a dislocation for which the calculated distribution of ρ matches

the observed distribution is greatly simplified.

The calculated distribution of the degree of polarization due to an edge dislocation at normal incidence to the surface (direction **d** out of the page) is illustrated in Fig. 5.4(a) over a 50 x 50 μm area for the case of a dislocation with Burgers vector **b** = 1/2 $[1\bar{1}0]$ = 4.15 Å in InP. Note the characteristic four-petal pattern. The shading of Figs. 5.4-5.8 is such that lighter shading corresponds to a higher value of ρ, with the full graduation from black to white corresponding to a variation in ρ from -0.00167 to $+0.00167$. The image is shaded black if ρ is below -0.00167, and white if ρ is above $+0.00167$. The distribution of Fig. 5.4(a) was calculated using Eq. (65), with $\sigma_{xx}(x,y)-\sigma_{yy}(x,y)$ given by Eq. (67). When evaluating the dislocation stresses, the Voight averages of the shear modulus μ and Poisson's ratio ν were used [84], calculated to be $\mu = 3.65\times10^{11}$ dyn/cm^2 and $\nu = 0.28$ from the elastic stiffness coefficients for InP [68].

If the sample containing the dislocation of Fig. 5.4(a) is rotated 45 degrees clockwise, the calculated distribution of ρ around the dislocation exhibits the six-petal pattern illustrated in Fig. 5.4(b). This distribution was calculated using Eqs. (66) and (67). Images of the stresses due to edge dislocations normal to the wafer surface have been previously obtained using IR birefringence [39], and are similar to the images of Figs. 5.4(a) and 5.4(b) since in this case the surface stresses are simply $(1+2\nu)(1-\nu)$ times the stresses in the bulk material. However, in general the surface stress distributions are considerably different from the distributions far from the surface.

Figures 5.5(a) and 5.5(b) show the calculated distributions of ρ for a screw dislocation penetrating the surface of the material in a $[0\bar{1}1]$ direction, at 45 degrees to

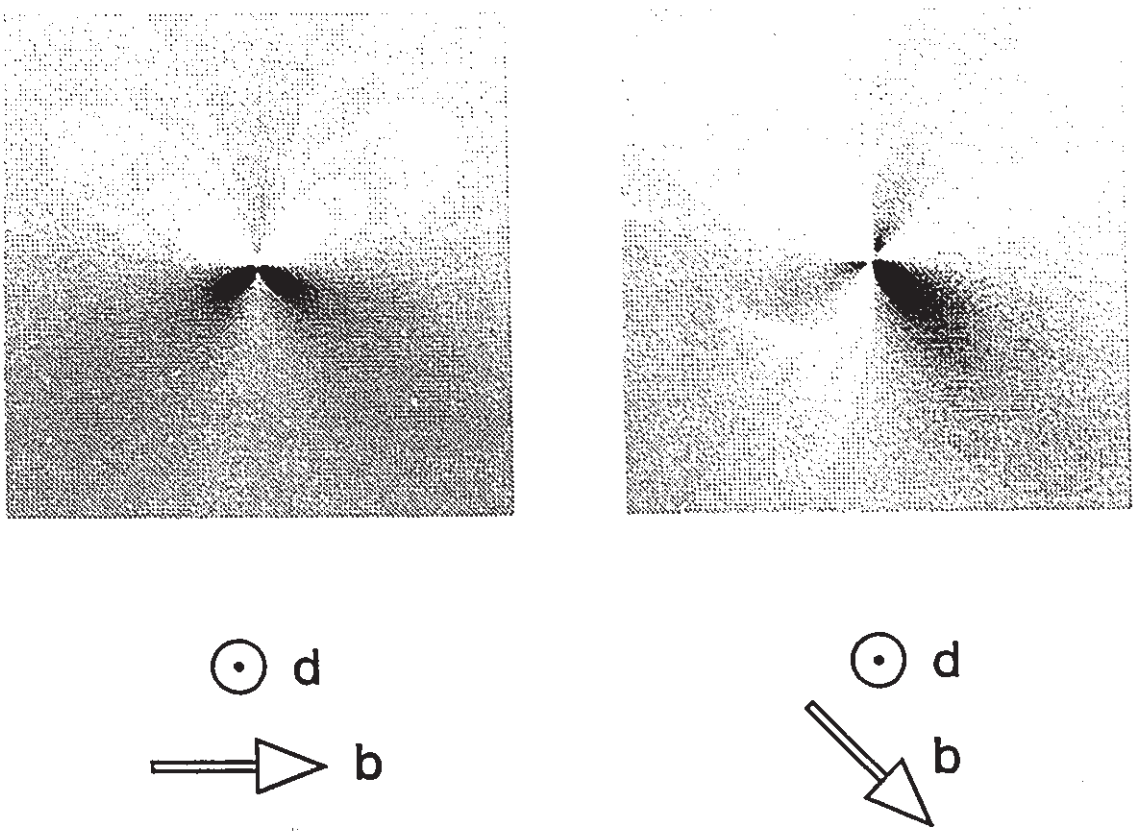

Figure 5.4 The calculated distribution of ρ near an edge dislocation at normal incidence, with the sample rotated (a) 0°, and (b) 45°.

the (001) surface with Burgers vector b = 1/2 [01$\bar{1}$], for 0 and 45 degree orientations of the sample respectively. These distributions were calculated using surface stresses given by Eqs. (69)-(71) with appropriate coordinate transformations. Note that unlike Figs. 5.4(a) and 5.4(b), rotation of the patterns of Figs. 5.5(a) and Fig. 5.5(b) by 180 degrees and inversion of shading result in different patterns. This asymmetry is due to the non-normal incidence of the dislocation. In general, the distribution of ρ will show the same symmetry as the dislocation's direction and Burgers vector.

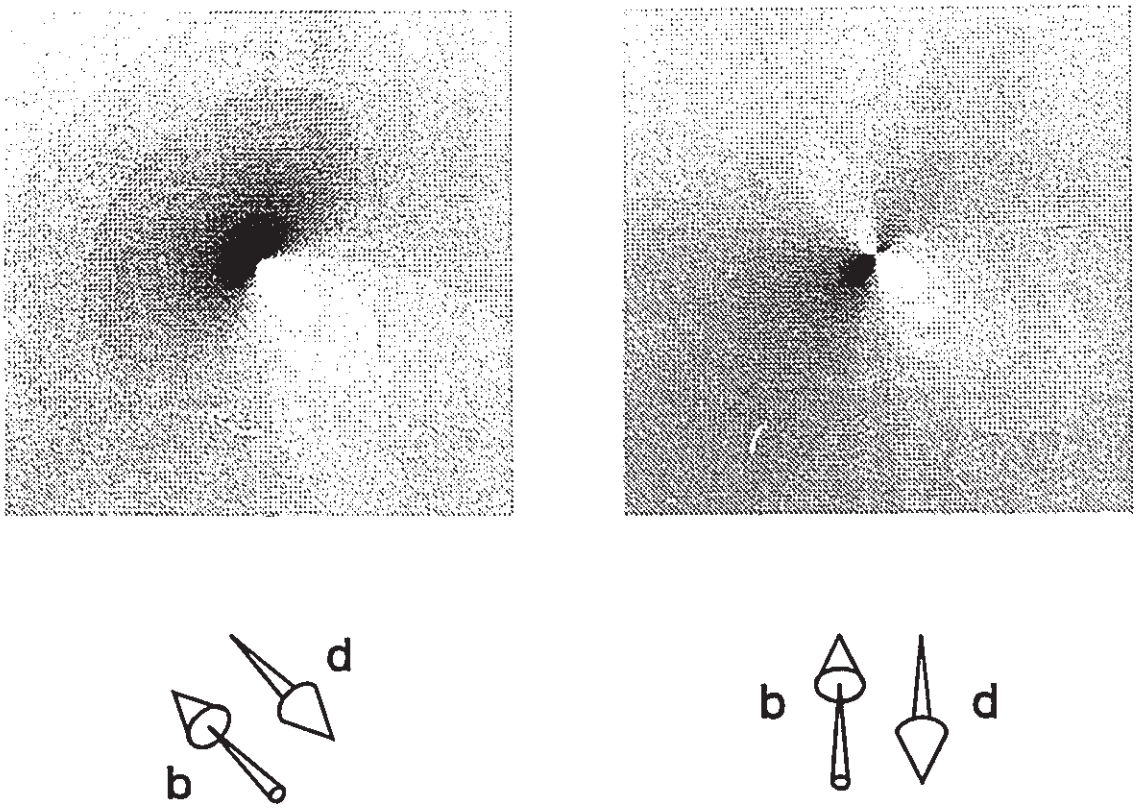

(a) (b)

Figure 5.5 The calculated distribution of ρ near a screw dislocation at 45 degrees to the sample surface, with the sample rotated (a) 0°, and (b) 45°.

Figures 5.6(a) and 5.6(b) show the calculated distributions of ρ for a 60 degree dislocation with Burgers vector $\mathbf{b} = 1/2\ [\bar{1}01]$ intersecting the surface of the material in a $[0\bar{1}1]$ direction, for 0 and 45 degree orientations of the sample respectively. These distributions were calculated using surface stresses given by Eqs. (69)-(71).

The calculated distribution of ρ due to a screw dislocation at normal incidence, calculated using Eqs. (65) and (68), is shown in Fig. 5.7. The distribution of ρ is the same regardless of the sample rotation, due to the rotational symmetry of a screw

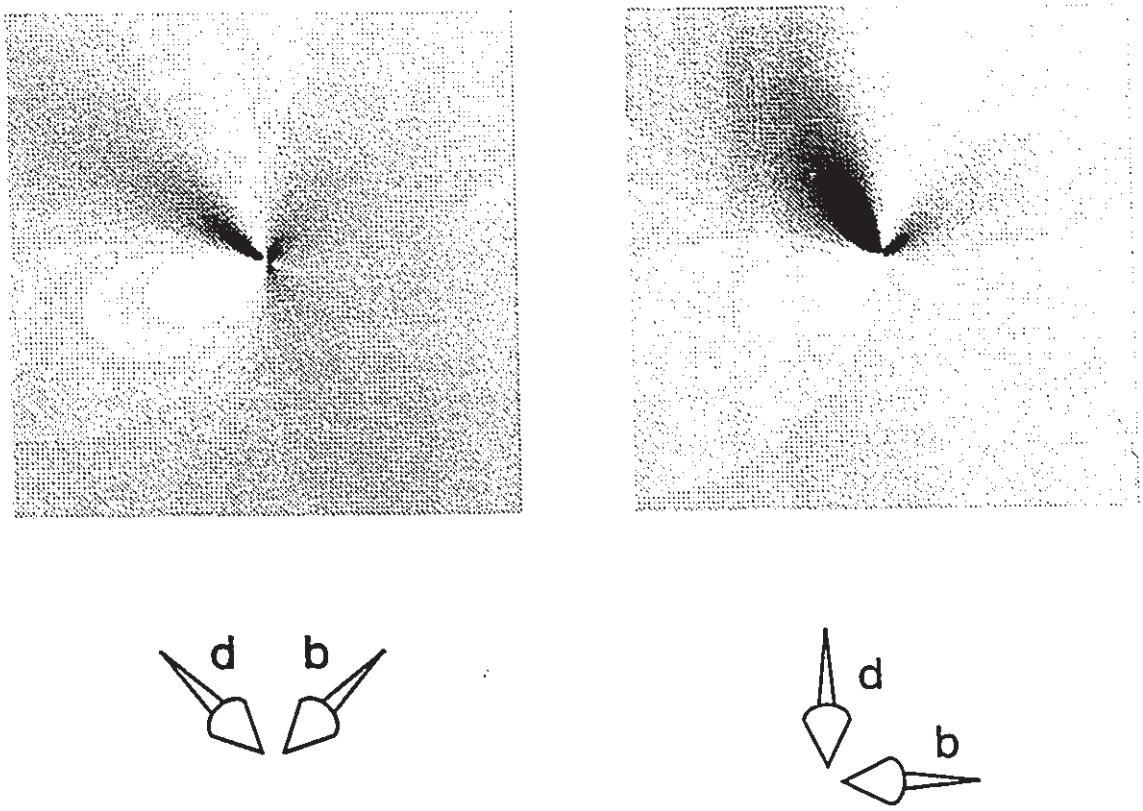

Figure 5.6 The calculated distribution of ρ near a 60° dislocation at 45 degrees to the sample surface, with the sample rotated (a) 0°, and (b) 45°.

dislocation at normal incidence.

Often, dislocations in observed samples will not be in the same orientation as those of Figs. 5.4-5.6. For example, a screw dislocation similar to Fig. 5.5 may have any of the equivalent dislocation directions of [011], [$0\bar{1}1$], [101], or [$\bar{1}01$], with the Burgers vector either in the same direction or the opposite direction as the dislocation direction, for a total of eight equivalent dislocations. The distributions of ρ for each of these dislocations can be determined by rotating or inverting the shading of Fig. 5.5. In

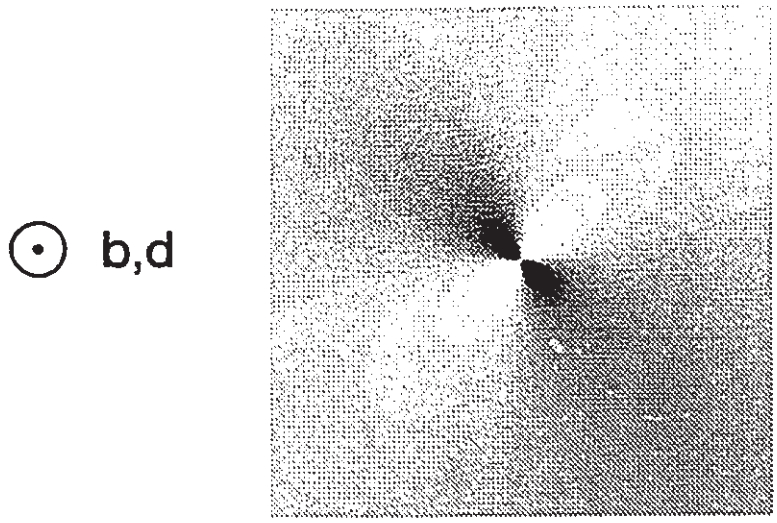

Figure 5.7 The calculated distribution of ρ near a screw dislocation at normal incidence to the sample surface.

general, if the dislocation is rotated by 90°, 180°, or 270° from the given dislocation, the distribution of ρ image will be rotated by the same angle. Note, however, that the shading will invert for 90° and 270° rotations because of the reversal of the sign of ρ as σ_{xx} and σ_{yy} are interchanged in Eq. (65). A reversal of the Burgers vector also causes inversion of shading. Thus, the distributions of ρ for all 8 equivalent screw dislocations can be readily derived from Fig. 5.5, and hence the direction and Burgers vector of a screw dislocation causing any of the 8 images can be easily determined. In the case of the 60° dislocation of Fig. 5.6, mirror images of the dislocations are possible as well as reversal of the Burgers vector and rotations. A mirror image of the dislocation about a vertical or horizontal plane, i.e., $x = 0$ or $y = 0$, causes the distribution of ρ to be a mirror image about the same plane with inversion of shading. A mirror image about a diagonal plane, i.e., $x = y$ or $x = -y$, causes the distribution of ρ to be a mirror image

about the same plane. Thus, 16 types of equivalent 60° dislocations are possible, and each may be identified from its pattern of surface stresses.

It is clear from the calculated stress distributions that different dislocation types produce very different surface stress patterns. The direction and Burgers vector of dislocations may therefore be identified by comparing the measured distributions of $(\sigma_{xx}-\sigma_{yy})$ and σ_{xy} with the calculated distributions.

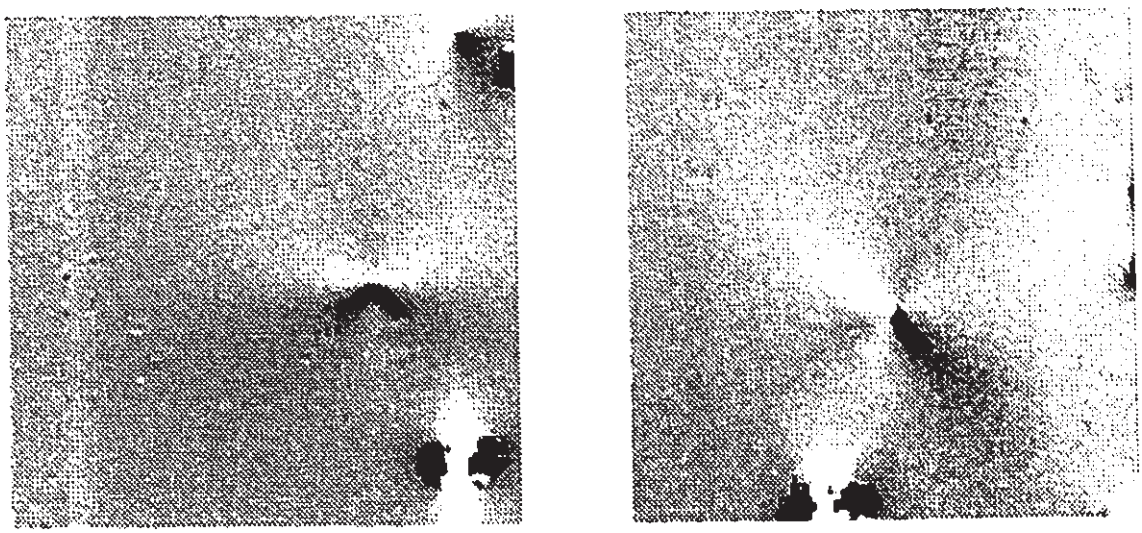

(a) (b)

Figure 5.8 The measured distribution of ρ for an InP sample indicating an edge dislocation at normal incidence to the surface (compare Fig. 5.4), with the sample rotated (a) 0° and (b) 45°.

Fig. 5.8(a) shows the measured distribution of ρ over a 50 x 50 μm area of a (001) oriented InP sample consisting of an MBE-grown InP layer on an InP substrate. The feature in the lower right corner is due to an oval defect in the grown layer. The four-petal pattern of Fig. 5.4(a) is clearly visible near the center of Fig. 5.8(a), indicating the presence of an edge dislocation normal to the wafer surface with Burgers

vector $\mathbf{b} = 1/2\ [1\bar{1}0]$ (horizontal and to the right in Fig. 5.8(a)). A reduction in the luminescence intensity of about 10 percent was observed over a 1 μm diameter area (the spatial resolution of the optical system) around the dislocation. The observable stresses (greater than 3×10^6 dyn/cm^2) extend at least 15 μm from the dislocation. Fig. 5.8(b) shows the distribution of ρ for the same dislocation after the sample was rotated clockwise 45 degrees. The distribution of ρ now resembles the six-petal pattern of Fig. 5.4(b). It is clear that Fig. 5.8(a) and Fig. 5.8(b) indicate the presence of a dislocation, since the observed distributions of ρ closely match the calculated distributions in shape and magnitude (within 30 percent).

Fig. 5.9(a) shows the distribution of ρ over another 50 x 50 μm section of the same InP wafer. The pattern near the center of the image resembles Fig. 5.5(a), indicating a screw dislocation running along a $[0\bar{1}1]$ direction with Burgers vector $\mathbf{b} = 1/2\ [01\bar{1}]$, penetrating the surface at a 45 degree angle. A second dislocation with inversion of shading is visible in the lower right corner of Fig. 5.9(a), indicating a screw dislocation with the same direction but opposite Burgers vector. Fig. 5.9(b) shows the same region after the sample was rotated clockwise 45 degrees. The two-petal pattern of Fig. 5.5(b) is apparent. For these screw dislocations the reduction in the luminescence intensity was about 5 percent at the position of the dislocation.

Screw dislocations resembling the ones in Fig. 5.9 outnumbered edge dislocations resembling Fig. 5.8 by about 50 to 1 on the observed samples, and appeared in only four of eight possible orientations, with roughly equal probability. The four orientations observed included the two seen in Fig. 5.9 (i.e., inversion of shading), plus rotation of

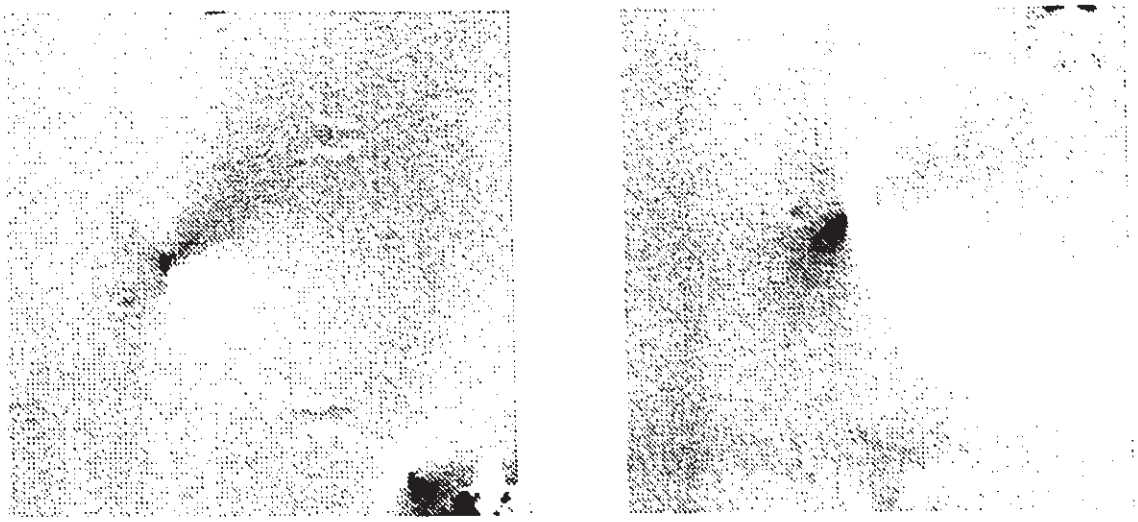

(a) (b)

Figure 5.9 The measured distribution of ρ for an InP sample indicating a screw dislocation at 45 degrees to the surface (compare Fig. 5.5), with the sample rotated (a) 0° and (b) 45°.

those by 180 degrees. The absence of images rotated by 90 degrees in these samples suggests a directional preference for dislocation formation during crystal growth. No 60° threading dislocations or screw dislocations at normal incidence were seen.

The observed dislocation densities were about the same on the MBE-grown layers and the substrate material, which indicates that the dislocations were not generated during the MBE growth. A density of dislocations of about $4\times10^4/cm^2$ was observed, which is in agreement with the dislocation density of $\leq5\times10^4/cm^2$ specified by the manufacturer of the substrate material (determined from etch pit density). By comparison, a dislocation density of about $5\times10^3/cm^2$ was observed on another type of InP substrate material specified as $\leq5\times10^3/cm^2$. These factors strongly support the claim that the observed stress patterns are due to individual dislocations. Dislocation

stresses have also been observed in GaAs samples, and it is expected that the technique is suitable for any luminescent semiconductor.

The images presented in this section cover an area 50 x 50 μm in 0.5 μm steps. The fine stepsize was used to produce clear images of the dislocation stresses. However, dislocations may be readily identified from images produced with stepsizes of at least 2 μm, allowing faster counting of dislocations if necessary.

5.3 Misfit dislocations in epitaxial layers

The stresses due to a dislocation running parallel to a free surface can be calculated using techniques similar to the image charge technique of electrostatics. If the surface is the plane $z=0$, the free surface boundary conditions are $\sigma_{xz}=\sigma_{yz}=\sigma_{zz}=0$.

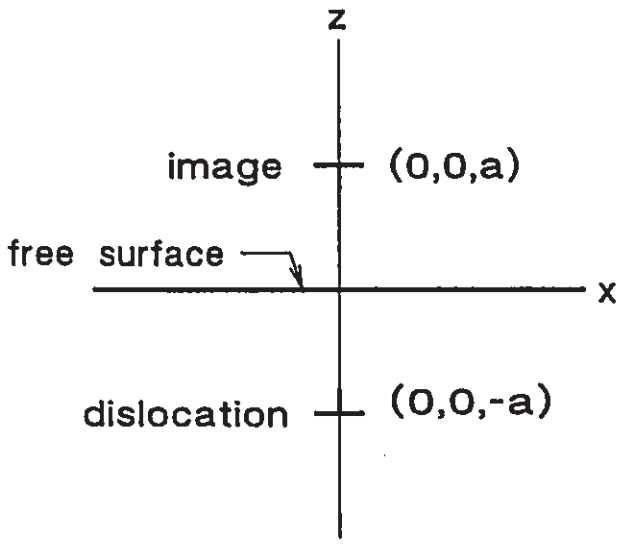

Figure 5.10 The surface stresses due to a misfit dislocation can be solved by placing an 'image' dislocation outside the free surface.

Taking the dislocation to run in the $+y$ direction through the point $(0,0,-a)$, an image dislocation of opposite Burgers vector is placed passing through the point $(0,0,a)$ as shown in Fig. 5.10. The image dislocation induces stresses which cancel, or partly cancel, the stresses σ_{xz}, σ_{yz}, and σ_{zz} induced by the real dislocation at the plane $z=0$. For a screw dislocation, the combined real and image stresses satisfy the boundary conditions, and hence the problem is solved [84], resulting in surface stresses which are double the values in an infinite material, and for the case of the Burgers vector b_s along the $+y$ direction,

$$\begin{aligned} \sigma_{xx} &= \sigma_{yy} = 0 \\ \sigma_{xy} &= \frac{\mu b_s}{\pi} \cdot \frac{a}{x^2+a^2} \end{aligned} \tag{75}$$

For the case of an edge dislocation parallel to a free surface, the problem is not so simple. Additional stress terms must be added to satisfy the boundary conditions. This problem has been solved by Head [87] for edge dislocations with Burgers vectors parallel and perpendicular to the free surface. The surface stresses ($z=0$) are given by

$$\begin{aligned} \sigma_{xx} &= \frac{2Eb_\parallel}{\pi(1-\nu^2)} \cdot \frac{ax^2}{(a^2+x^2)^2} \\ \sigma_{yy} &= \nu\sigma_{xx} \\ \sigma_{xy} &= 0 \end{aligned} \tag{76}$$

if the Burgers vector $b_\parallel$ is parallel to the surface (along the $+x$ direction), and

$$\sigma_{xx} = \frac{2Eb_{\perp}}{\pi(1-\nu^2)} \cdot \frac{a^2 x}{(a^2+x^2)^2}$$
$$\sigma_{yy} = \nu\sigma_{xx} \qquad (77)$$
$$\sigma_{xy} = 0$$

if the Burgers vector $b_{\perp}$ is perpendicular the the surface (along the $+z$ direction). The normalized stresses $a(\sigma_{xx}-\sigma_{yy})$ and $2a\sigma_{xy}$ are graphed in Fig. 5.11 as a function of the normalized position x/a for each dislocation type, assuming a Burgers vector of magnitude 4.15 Å in each case. Note that the shear modulus μ of Eq. (75) and Young's modulus E of Eqs. (76) and (77) are related by $\mu = E/2(1+\nu)$ [47].

For mixed dislocations with arbitrary Burgers vectors, the stresses can be calculated by summing the stresses induced by the edge and screw components [84]. For example, for a 60 degree misfit dislocation in an (001) oriented sample, the components of the Burgers vector are $|b_{\parallel}| = |\mathbf{b}|/2$, $|b_{\perp}| = |\mathbf{b}|/\sqrt{2}$, and $|b_s| = |\mathbf{b}|/2$. The resulting surface stresses are graphed in Fig. 5.11.

Note that the width between the two peaks of the surface stress generated by a 60 degree dislocation is about 1.2 times the thickness of the epitaxial layer. Provided the epitaxial layer is sufficiently thick (>0.7 μm) so that the two peaks may be resolved, it is possible to determine the sign of the perpendicular edge component of a 60 degree misfit dislocation. The parallel edge component and the screw component can always be resolved, since the surface stresses are of a single sign. Even if the spatial extent of the stress distribution is smaller than the resolution of the measurement system, the sign of the observed stress will indicate the sense of the parallel edge component and the

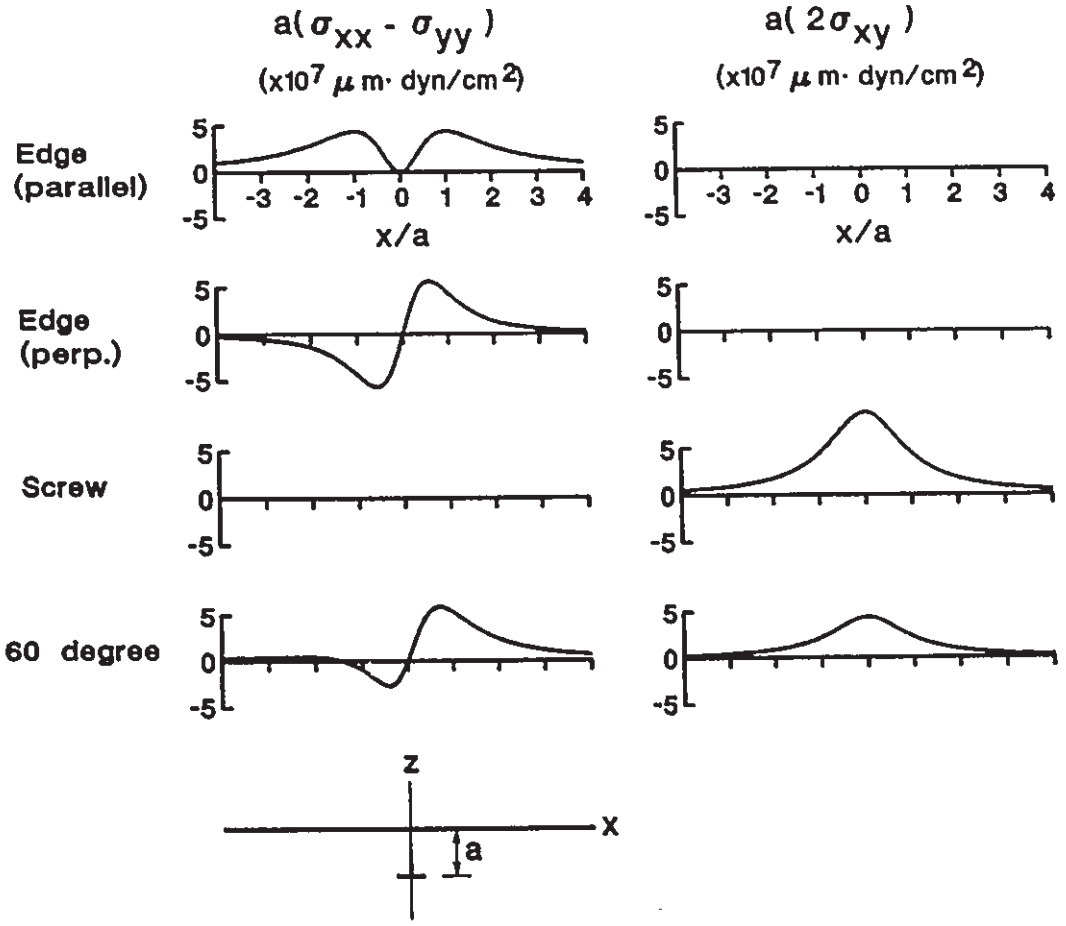

Figure 5.11 The calculated surface stresses near misfit dislocations of various types in an epitaxial layer of thickness *a*.

screw component of the dislocation.

Figure 5.12 reveals misfit dislocations in a 2.3 μm thick $In_{0.99}Ga_{0.01}P$ layer grown by MBE on an InP substrate (sample MBE-296). The scan area is 100×100 μm^2. The dislocation lines in Fig. 5.12(a) show the pattern expected from the edge components of a 60 degree dislocation, with the vertical dislocations appearing light with a weaker dark line to the right, and the horizontal lines appearing dark with a weaker light line above. The lines in Fig. 5.12(b) show the single-shaded pattern expected from the screw

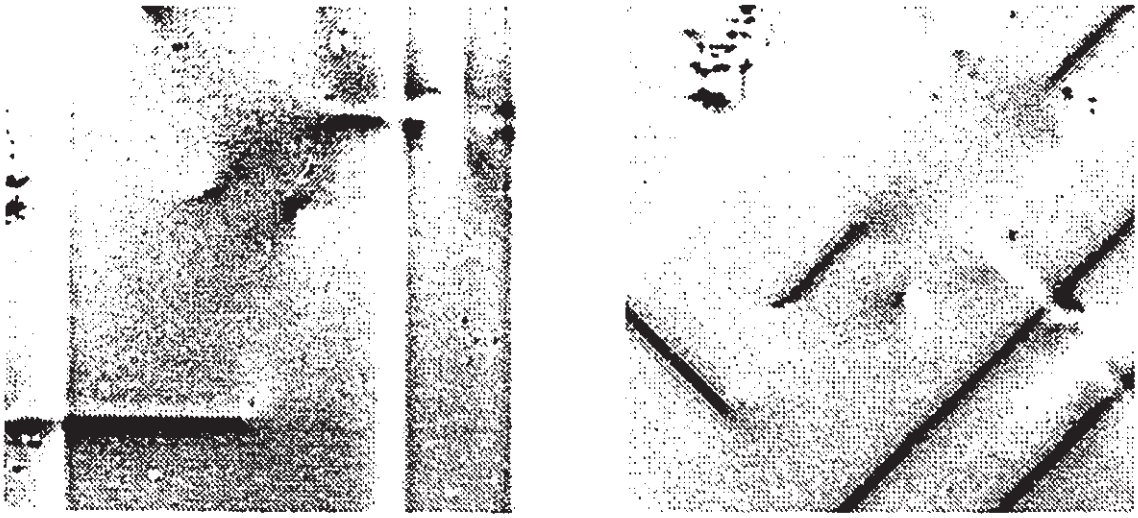

(a) (b)

Figure 5.12 The measured distribution of ρ for an MBE-grown InGaP/InP sample indicating 60° misfit dislocations, with the sample rotated (a) 0° and (b) 45°.

component of a 60 degree dislocation. Therefore, the misfit dislocations seen in Fig. 5.12 are all determined to be 60 degree dislocations. The magnitudes of the observed stresses match those of the calculated stresses within about 20 percent. The direction of the parallel edge component of the Burgers vector (determined by the sense of the most strongly shaded line of each dislocation in Fig. 5.12(a)) is always in the direction required to relax the strain in the epitaxial layer, as expected. The edge component perpendicular to the surface (determined by which side of each dislocation in Fig. 5.12(a) has the weakly-shaded line) is the same for each dislocation of Fig. 5.12(a). Some dislocations in other parts of the sample had opposite perpendicular components of the Burgers vector, but there were a greater number with the same sense as Fig. 5.12(a). The screw component direction (determined by the sense of the shading of each line in

Fig. 5.12(b)) appears to be random. The perpendicular edge component and the screw component of each dislocation should be random, since these components of the Burgers vector do not contribute to the relaxation of the misfit strain. The apparent preference for one sense of the perpendicular edge component is unexpected, and suggests that there is a difference in the energy of formation of 60 degree dislocations with different perpendicular edge components of the Burgers vector.

Note that one of the dislocations near the center of Fig. 5.12 became shorter between the scans of Figs. 5.12(b) and 5.12(a) (the scan of Fig. 5.12(b) was done first). This dislocation was repeatedly observed, and became shorter in each successive scan, eventually diminishing to only a threading dislocation penetrating the surface. Apparently, the pump laser illumination caused the dislocation to move through recombination enhanced defect motion. It is interesting that, although it was obviously energetically favorable for dislocations to form in this sample at the growth temperature, it appears to be energetically unfavourable for the misfit dislocations to be present at room temperature. Perhaps the dislocation density could be reduced in certain strained epitaxial layers by illuminating the sample for a period of time after the epitaxial growth.

Fig. 5.13(a), also taken from sample MBE-296, reveals two 60 degree misfit dislocations, plus an edge dislocation with Burgers vector parallel to the sample surface. The scan area is 45×45 μm^2. The separation between the two lines of the edge dislocation stress pattern in Fig. 5.13(a) is about twice the layer thickness, in agreement with the calculated stress distribution of Fig. 5.11. The edge of the sample is at the upper edge of Fig. 5.13(a). At the edge of the sample, the compressive elastic stress σ_{yy}

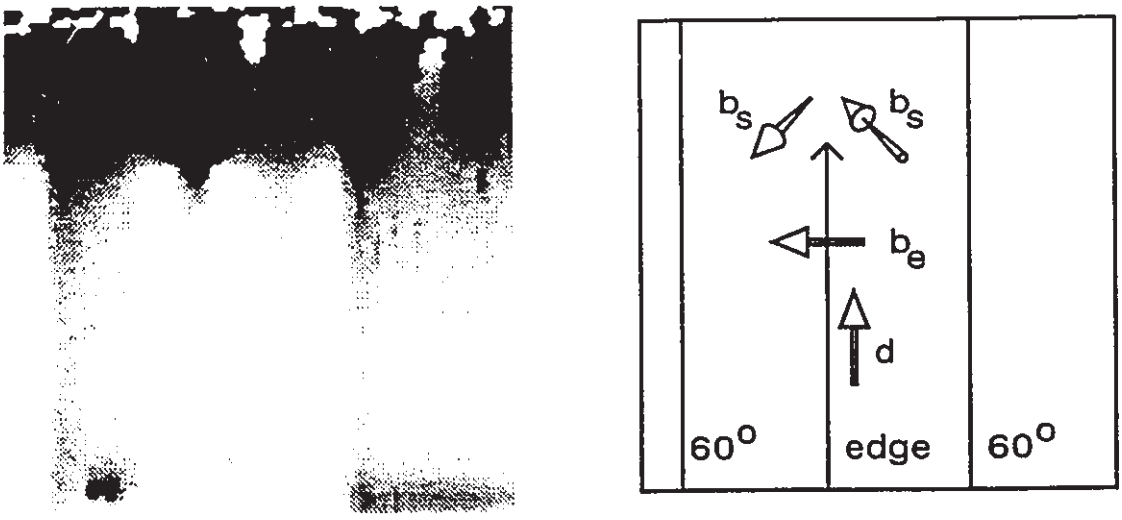

(a) (b)

Figure 5.13 (a) Two 60° misfit dislocations and an edge misfit dislocation are revealed in an MBE-grown InGaP/InP sample. (b) The edge dislocation splits into two screw dislocations, which intersect the surface.

of the epitaxial layer is relieved because the boundary condition $\sigma_{yy} = 0$ must be met at the free edge. This causes the dark band at the top of Fig. 5.13(a). Near the top of the picture, the edge dislocation ends and two screw dislocations are seen penetrating the surface. This combination of dislocations maintains continuity of the total Burgers vector at the intersection point, illustrated in Fig. 5.13(b), as required by any dislocation network [88]. In Fig. 5.13(b), the dislocation direction **d** was chosen such that the directions for the screw dislocations would be emerging from the material. The relieving of the stress at the edge of the sample may have caused the edge dislocation to split into the two screw dislocations, which then moved away from the edge of the sample.

Figure 5.14 shows a pattern of misfit dislocations in a 0.3 μm thick MBE-grown $In_{0.95}Ga_{0.05}P$ layer on InP. The scan area is 50 × 50 μm^2. Dark horizontal lines and

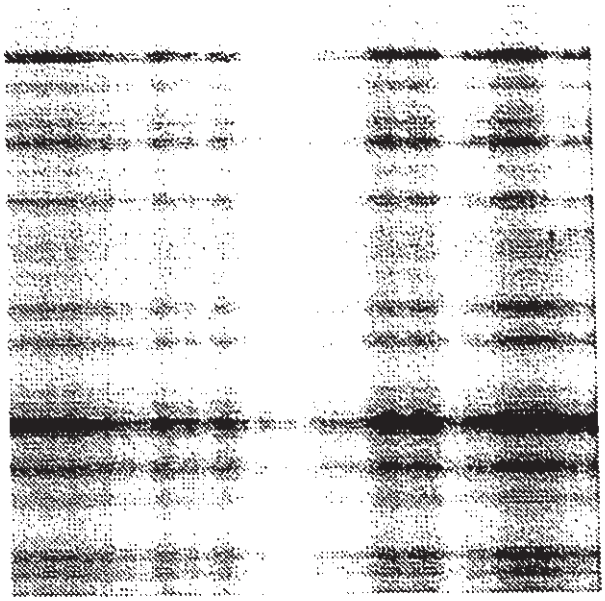

Figure 5.14 The distribution of ρ for an MBE-grown InGaP layer on InP, revealing an array of misfit dislocations. The stresses add where dislocations overlap.

light vertical lines indicate misfit dislocations. In this image, some of the dislocations are too closely spaced to be resolved optically. Nevertheless, the dislocations can still be 'counted' because the stresses from each dislocation add linearly, creating lighter and darker lines where dislocations overlap. Other techniques such as photoluminescence and cathodoluminescence intensity maps [80,81], which reveal dislocations from the reduced luminescence intensity near the dislocation, do not have the property that the signal depth is proportional to the number of dislocations present, and therefore cannot provide an accurate dislocation count at higher dislocation densities.

5.4 Summary

In summary, it has been demonstrated that polarization-resolved photoluminescence can be used to detect stresses due to individual dislocations in semiconductors. The observed stress patterns matched the calculated patterns in shape and magnitude for both threading and misfit dislocations, and the observed density of threading dislocations agreed with the wafer manufacturer's specification of dislocation density. It has been shown that the Burgers vector and direction of the dislocations can be readily determined from the stress patterns. This technique provides a simple, non-destructive method of counting and characterizing dislocations in luminescent semiconductors.

Chapter 6. Future Work

The results of the research presented in this thesis suggest many possibilities for future work. The most important topic to be addressed, in my opinion, is the relationship between the processing-induced active region stresses and device degradation in semiconductor diode lasers. The techniques of polarization-resolved electroluminescence and photoluminescence provide measures of the active region stress to a resolution not previously attainable. The relative simplicity of the techniques should allow stress measurements to be done on statistically significant numbers of devices, to look for a correlation between active region stress and life-test performance. This would require a high level of interaction between manufacturers and researchers, because special stress-free and/or stress-enhanced structures would have to be made to provide meaningful comparisons. A conclusive experiment would probably require several iterations of refinements in device structure and processing. Unfortunately, I did not have the time or the required level of interaction with the manufacturer(s) to achieve this goal.

Before the relationship between stress and degradation can be adequately addressed, it must first be determined which manufacturing processes are inducing the active region stresses. This could be achieved by examining wafer sections at various stages of processing. Once the causes of the stresses are known, modifications to the manufacturing processes could be developed to reduce the stress.

More information about degradation could be obtained by imaging the active layer through the substrate (similar to the technique of Peters and Cassidy [60]), using electroluminescence or photoluminescence, to observe the formation of dark line defects or dark spot defects during device operation. It could be determined whether the defects form more readily in regions which are under greater stress. This experiment would be possible only for devices for which the substrate is transparent to the active region luminescence, such as InP-based devices or GaAs-based devices with an emission wavelength greater than about 910 nm. It may be possible to examine shorter wavelength GaAs devices through the p-side cap layers if they could be manufactured with a window in the metallization layer.

An interesting experiment would be to determine the coefficients of the tensor K relating stress and the degree of polarization, and to verify that the stress-induced degree of polarization does in fact vary with crystal orientation according to the tensor relationships developed in Chapter 2. A more complete theory of stress-induced degree of polarization, and comparison with the experimental data, may provide useful information about the band structures of GaAs and InP. Any measured dependence of K on temperature, doping level and type, excitation level, or other parameters may also provide useful information.

It would be useful to calculate and measure the effect of stress on the degree of polarization of quantum well structures, which are already highly polarized due to the quantum confinement. It is likely that the changes in band structure due to the quantum confinement significantly affect the relationship between stress and the degree of

polarization. More information about this effect would be valuable for determining active region stresses from the electroluminescence data of quantum well lasers, and for determining the level of strain in strained-layer quantum wells from polarization-resolved measurements.

Three-dimensional scanning of stress distributions may be possible with polarization-resolved photoluminescence. It is a property of a confocal imaging system such as the photoluminescence setup that resolution in three dimensions can be obtained. If the pump laser wavelength is selected to provide a fairly long absorption depth in the semiconductor sample, the pump beam may be focussed such that the region in the sample producing the brightest luminescence is well below the sample surface. If the detectors are also focussed at the same point, the luminescence from other regions of the sample will be rejected, and hence a stress measurement at a point below the sample surface can be obtained. A tunable diode laser may be a suitable pump laser. Possible problems may arise from self-absorption of the luminescence from the sample, or variations in the absorption cutoff wavelength (bandgap) throughout the sample due to stress variations, impurities, or defects.

Investigation into the waveguiding properties of various structures may be aided by polarization-resolved photoluminescence. Stress-induced refractive index changes can affect the waveguiding properties, and polarization-resolved photoluminescence is capable of measuring the stress distributions, so that a more accurate picture of the refractive index profile of the waveguide structure can be obtained.

Polarization-resolved photoluminescence may be used to determine the critical

thickness for strained layers, which is the maximum thickness which can be grown without misfit dislocations. Anisotropy effects in the dislocation formation could also be investigated. These measurements can also be easily made using other dislocation-detecting techniques such as photoluminescence or cathodoluminescence intensity maps, but polarization-resolved photoluminescence has the advantage of determining the Burgers vectors of the dislocations. This information can be interesting; for example, recent measurements indicate that for strained layers grown on misoriented substrates the screw and perpendicular edge components of the dislocation Burgers vectors are not random, but are correlated with the dislocation direction and the direction of misorientation of the substrate.

Chapter 7. Conclusion

After completing this research, I have become convinced of two things: first, that it is important to be able to measure stresses in diode lasers and related structures; and second, that polarization-resolved electroluminescence and photoluminescence are the most useful techniques for performing such stress measurements. I hope that others will reach the same conclusions after reading this thesis. The relationship between stress and degradation has been mentioned in many articles and books on diode laser reliability from 1975 to the present, but most experimental correlations of degradation with internal processing stresses have been based on calculated stresses, not measured stresses. As mentioned in Chapter 1, all previous methods known to me of measuring stress in diode lasers have either insufficient spatial resolution or insufficient stress resolution to be of practical use for diode laser analysis. Fortunately, polarization-resolved electroluminescence and photoluminescence have the required resolution in both stress and position to provide useful information near the active region of diode lasers, as shown by the results reported in Chapters 3 and 4.

I anticipated that polarization-resolved photoluminescence should be able to detect individual dislocations, since the product of the spatial and strain resolutions suggests that an atomic displacement of about $(1\ \mu m)\times(10^{-5}) = 0.1$ Å should be detectable. However, I expected that it would be difficult to prove that an observed feature was in fact a dislocation. Fortunately this was not the case, since as shown in Chapter 5, the

observed stress patterns are unmistakable. The greatest advantage of polarization-resolved photoluminescence in dislocation detection is its ability to determine the Burgers vector of the dislocations. In this respect the only competing non-destructive technique, to my knowledge, is X-ray topography. Because of fundamental differences in the detection mechanisms, X-ray topography and polarization-resolved photoluminescence will likely be complementary techniques, each with certain advantages in particular situations.

Since polarization-resolved stress measurement techniques are so simple and useful, it is puzzling that they have not been used until so recently. Ryan and Miller [13] noted in 1963 that uniaxial strain affects the spontaneous emission probability in the TE and TM polarizations of a GaAs diode laser. Still, in 1990, Kawasaki et. al. [27] used polarization-resolved photoluminescence to determine the stress direction in GaAs, but used the wavelength shift instead of the degree of polarization to determine the stress magnitude, resulting in much more time-consuming and less accurate measurements. It is unfortunate that the degree of polarization has not been utilized to a greater extent for measuring stresses in GaAs and InP, since many efforts have been made using less favourable techniques. Hopefully this oversight will be corrected in the future.

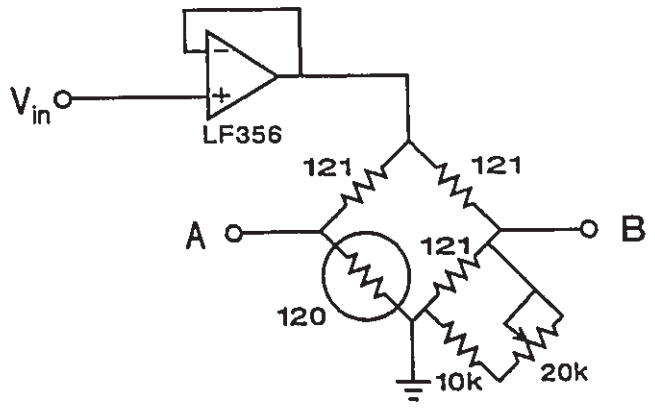

V_{in} is supplied by PAR Model 126 lock-in amplifier, 1930 Hz, 1V rms sinewave. Lock-in input is set to 'A−B' mode.

Figure A.1 The bridge circuit used to measure the strain gauge resistance.

Chapter 9. References

1. P. G. Eliseev and A. V. Khaidarov, "Role of mechanical stresses in gradual degradation of light-emitting diodes and injection lasers," *Sov. J. Quantum Electron.* 5, 73-74 (1975).

2. S. Kishino, N. Chinone, H. Nakashima, and R. Ito, "Dark-line defects induced by mechanical bending in GaAs-$Ga_{1-x}Al_xAs$ double-heterostructure wafers," *Appl. Phys. Lett.* **29**, 488-490 (1976).

3. B. Wakefield, "Strain-enhanced luminescence degradation in GaAs/GaAlAs double-heterostructure lasers revealed by photoluminescence," *J. Appl. Phys.* **50**, 7914-7916 (1979).

4. M. J. Robertson, B. Wakefield, and P. Hutchinson, "Strain-related degradation phenomena in long-lived GaAlAs stripe lasers." *J. Appl. Phys.* **52**, 4462-4466 (1981).

5. A. R. Goodwin, P. A. Kirkby, I. G. A. Davies, and R. S. Baulcomb, "The effects of processing stresses on residual degradation in long-lived $Ga_{1-x}Al_xAs$ lasers," *Appl. Phys. Lett.* **34**, 647-649 (1979).

6. P. W. Epperlein, A. Fried, and A. Jakubowicz, "Stress-induced defects in GaAs quantum well lasers," *Inst. Phys. Conf. Ser.* **112**, 567-572 (1990).

7. T. Hayakawa, N. Miyauchi, S. Yamamoto, H. Hayashi, S. Yano, and T. Hijikata, "Improved lifetimes of (GaAl)As visible (740 nm) lasers by reducing bonding stress," *Appl. Phys. Lett.* **42**, 23-24 (1983).

8. A. K. Chin, W. C. King, T. J. Leonard, R. J. Roedel, C. L. Zipfel, V. G. Keramidas, and F. Ermanis, "Stress-induced dark line defect formation in GaAlAs:Si LED's," *J. Electrochem. Soc.* **128**, 661-669 (1981).

9. B. Sieber, J. L. Farvacque, J. Wang, and J. W. Steeds, "Possible origin of degradation mechanisms in AlGaAs/GaAs laserlike structures," Appl. Phys. Lett. **60**, 2654-2656 (1992).

10. O. Ueda, "Degradation of III-V opto-electronic devices," *J. Electrochem. Soc.* **135**, 11C-22C (1988).

11. H. Shimizu, K. Itoh, M. Wada, T. Sugino, and I. Teramoto, "Improvement in operation lives of GaAlAs visible lasers by introducing GaAlAs buffer layers," *IEEE J. Quantum Electron.* **QE-17**, 763-767 (1981).

12. W. Both, G. Erbert, A. Klehr, R. Rimpler, G. Stadermann, and U. Zeimer, "Catastrophic optical damage in GaAlAs/GaAs laser diodes," *IEE Proc.* **134**, pt. J, 95-103 (1987).

13. F. M. Ryan and R. C. Miller, "The effect of uniaxial strain on the threshold current and output of GaAs lasers," *Appl. Phys. Lett.* **3**, 162-163 (1963).

14. P. G. Eliseev, B. N. Sverdlov, and N. Shokhudzhaev, "Reduction of the threshold current of InGaAsP/InP heterolasers by unidirectional compression," *Sov. J. Quantum Electron.* **14**, 1120-1121 (1984).

15. T. Kobayashi and K. Sugiyama, "Effects of uniaxial stress on the double heterostructure lasers," *Japan. J. Appl. Phys.* **12**, 1388-1392 (1973).

16. C. S. Adams and D. T. Cassidy, "Effects of stress on threshold, wavelength, and polarization of the output of InGaAsP semiconductor diode lasers," *J. Appl. Phys.* **64**, 6631-6638 (1988).

17. N. K. Dutta and D. C. Craft, "Effect of stress on the polarization of stimulated emission from injection lasers," *J. Appl. Phys.* **56**, 65-70 (1984).

18. N. B. Patel, J. E. Ripper, and P. Brosson, "Behavior of threshold current and polarization of stimulated emission of GaAs injection lasers under uniaxial stress," *IEEE J. Quantum Electron.* **QE-9**, 338-341 (1973).

19. V. Swaminathan, P. Parayanthal, and R. L. Hartman, "Electro-optical effects of externally applied $<100>$ uniaxial stress on InGaAsP 1.3 and 1.5 μm injection lasers," *Appl. Phys. Lett.* **52**, 1461-1463 (1988).

20. P. A. Kirkby, P. R. Selway, and L. D. Westbrook, "Photoelastic waveguides and their effect on stripe-geometry GaAs/$Ga_{1-x}Al_xAs$ lasers," *J. Appl. Phys.* **50**, 4567-4579 (1979).

21. K. Kobayashi, Y. Inoue, T. Nishimura, M. Hirayama, Y. Akasaka, and T. Kato, "Local-oxidation-induced stress measured by Raman microprobe spectroscopy," *J. Electrochem. Soc.* **137**, 1987-1989 (1990).

22. V. Swaminathan, W. R. Wagner, P. J. Anthony, G. Henein, and L. A. Koszi, "Bonding pad induced stresses in (Al,Ga)As double heterostructure lasers," *J. Appl. Phys.* **54**, 3763-3768 (1983).

23. V. Swaminathan, L. A. Koszi, and M. W. Focht, "Effect of macroscopic stress on accelerated aging of GaInAsP channeled substrate buried heterostructure lasers," *J. Appl. Phys.* **66**, 1849-1854 (1989).

24. G. E. Henein and W. R. Wagner, "Stresses induced in GaAs by TiPt ohmic contacts," *J. Appl. Phys.* **54**, 6395-6400 (1983).

25. I. A. Blech and E. S. Meieran, "Enhanced X-ray diffraction from substrate crystals containing discontinuous surface films," *J. Appl. Phys.* **38**, 2913-2919 (1967).

26. B. G. Yacobi, B. Elman, C. Jagannath, A. N. M. Masum Choudhury, and M. Urban, "Cathodoluminescence observation of metallization-induced stress variations in GaAs/AlGaAs multiple quantum well structures," *Appl. Phys. Lett.* **52**, 1806-1808 (1988).

27. K. Kawasaki, S. Sakai, N. Wada, and Y. Shintani, "Geometrical effects on the thermal stress in GaAs layers grown on Si substrates," *Inst. Phys. Conf. Ser.* **112**, 269-274 (1990).

28. A. Jakubowicz, "Revealing process-induced strain fields in GaAs/AlGaAs lasers via electron irradiation in a scanning electron microscope," *J. Appl. Phys.* **70**, 1800-1804 (1991).

29. F. K. Reinhart and R. A. Logan, "Interface stress of $Al_xGa_{1-x}As$-GaAs layer structures," *J. Appl. Phys.* **44**, 3171-3175 (1973).

30. D. T. Cassidy and C. S. Adams, "Polarization of the output of InGaAsP semiconductor diode lasers," *IEEE J. Quantum Electron.* **25**, 1156-1160 (1989).

31. P. D. Colbourne and D. T. Cassidy, "Bonding stress measurements from the degree of polarization of facet emission of AlGaAs superluminescent diodes," *IEEE J. Quantum Electron.* **27**, 914-920 (1991).

32. P. D. Colbourne and D. T. Cassidy, "Measurement of bonding stresses from the degree of polarization of facet emission," in Conference on Lasers and Electro-Optics, 1991 (Optical Society of America, Washington, DC 1991), pp. 264-265.

33. P. D. Colbourne and D. T. Cassidy, "Imaging of stresses in GaAs diode lasers using polarization-resolved photoluminescence," accepted for publication in *IEEE J. Quantum Electron.*

34. P. D. Colbourne and D. T. Cassidy, "Diode laser stress distributions measured by polarization-resolved photoluminescence," in Conference on Lasers and Electro-Optics, 1992, Vol. 12, OSA Technical Digest Series (Optical Society of America, Washington, DC 1992), pp. 492-493.

35. P. D. Colbourne and D. T. Cassidy, "Observation of dislocation stresses in InP using polarization-resolved photoluminescence," accepted for publication in *Appl. Phys. Lett.* **61** (Sept. 7, 1992).

36. P. D. Colbourne and D. T. Cassidy, "Dislocation detection using polarization-resolved photoluminescence," to be presented at the Sixth Canadian Semiconductor Technology Conference, 1992, Ottawa, Canada.

37. S. Amelinckx, The Direct Observation of Dislocations. Academic Press, New York, 1964.

38. J. B. Newkirk and J. H. Wernick, eds., Direct Observation of Imperfections in Crystals. Interscience Publishers, New York, 1962.

39. V. L. Indenbom, V. I. Nikitenko, and L. S. Milevskii, "Analysis of dislocation structure in crystals with polarized light," *Sov. Phys. Solid State* **4**, 162-166 (1962).

40. G. R. Booker, Z. Laczik, and P. Kidd, "The scanning infrared microscope (SIRM) and its application to bulk GaAs and Si: a review," *Semicond. Sci. Technol.* **7**, A110-A121 (1992).

41. G. E. Pikus and G. L. Bir, "Effect of deformation on the hole energy spectrum of germanium and silicon," *Sov. Phys. Solid State* **1**, 1502-1517 (1960).

42. M. S. Skolnick, A. K. Jain, R. A. Stradling, J. Leotin, J. C. Ouesset, and S. Askenazy, "An investigation of the anisotropy of the valence band of GaAs by cyclotron resonance," *J. Phys. C* **9**, 2809-2821 (1976).

43. R. N. Bhargava and M. I. Nathan, "Stress dependence of Photoluminescence in GaAs," *Phys. Rev.* **161**, 695-698 (1967).

44. F. H. Pollak and M. Cardona, "Piezo-electroreflectance in Ge, GaAs, and Si," *Phys. Rev.* **172**, 816-837 (1968).

45. E. O. Kane, "Band structure of indium antimonide," *J. Phys. Chem. Solids* **1**, 249-261 (1957).

46. S. W. Corzine, R. H. Yan, and L. A. Coldren, "Simple formulation for the polarization dependence of optical transitions in bulk and reduced dimensional structures," unpublished. Also, S. W. Corzine, R. H. Yan, and L. A. Coldren, "Optical gain in III-V bulk and quantum well semiconductors," in Quantum Well Lasers, Peter Zory, ed.

47. A. S. Saada, Elasticity Theory and Applications. Krieger, Malabar, Fla., 1983.

48. T. B. Bateman, H. J. McSkimin, and J. M. Whelan, "Elastic moduli of single-crystal gallium arsenide," *J. Appl. Phys.* **30**, 544-545 (1959).

49. J. M. Luttinger and W. Kohn, "Motion of electrons and holes in perturbed periodic fields," *Phys. Rev.* **97**, 869-883 (1955).

50. D. Ahn and S. Chuang, "Optical gain in a strained-layer quantum well laser," *IEEE J. Quantum Electron.* **24**, 2400-2406 (1988).

51. V. M. Agranovich and V. L. Ginzburg, Crystal Optics with Spatial Dispersion and Excitons, 2nd ed., Springer-Verlag, Berlin, 1984.

52. J. I. Pankove, Optical Processes in Semiconductors. Dover, New York, 1971.

53. J. Vilms and W. E. Spicer, "Quantum efficiency and radiative lifetime in p-type gallium arsenide," *J. Appl. Phys.* **36**, 2815-2821 (1963).

54. T. S. Narasimhamurty, Photoelastic and Electro-Optic Properties of Crystals, Plenum Press, New York, 1981.

55. B. W. Char, K. O. Geddes, G. H. Gonnet, M. B. Monagan, and S. M. Watt, MAPLE Reference Manual, 5th ed., Waterloo Maple Publishing, Waterloo, Ontario, Canada, 1990.

56. K. Maeda, Y. Yamashita, N. Maeda, and S. Takeuchi, "Radiation enhanced dislocation glide and rapid degradation," in Degradation Mechanisms in III-V Semiconductor Devices and Structures, V. Swaminathan, S. J. Pearton, and O. Manasreh, eds., Materials Research Society, Pittsburgh, 1990, pp. 69-80.

57. E. I. Gordon, "Mode selection in GaAs injection lasers resulting from Fresnel reflection," *IEEE J. Quantum Electron.* **QE-9**, 772-776 (1973).

58. G. A. Alphonse, D. B. Gilbert, M. G. Harvey, and M. Ettenberg, "High-power superluminescent diodes," *IEEE J. Quantum Electron.* **24**, 2454-2457 (1988).

59. J. C. Dyment, "Hermite-Gaussian mode patterns in GaAs junction lasers," *Appl. Phys. Lett.* **10**, 84-86 (1967).

60. F. H. Peters and D. T. Cassidy, "Spatially and polarization resolved electroluminescence of 1.3-μm InGaAsP semiconductor diode lasers," *Appl. Opt.* **28**, 3744-3750 (1989).

61. R. C. Juvinall, Fundamentals of Machine Component Design. New York, Wiley, 1983.

62. J. S. Blakemore, "Semiconducting and other major properties of gallium arsenide," *J. Appl. Phys.* **53**, R123-R181 (1982).

63. Y. C. Chen and J. M. Liu, "Temperature-dependent polarization behavior of semiconductor lasers," *Appl. Phys. Lett.* **45**, 731-733 (1984).

64. R. C. Weast, ed., CRC Handbook of Chemistry and Physics, 70th ed. CRC Press, Boca Raton, Fla., 1989, p. D-187.

65. Hitachi, Hitaceram SC-101 product specifications.

66. G. A. Slack and S. F. Bartram, "Thermal expansion of some diamondlike crystals," *J. Appl. Phys.* **46**, 89-98 (1975).

67. T. R. Massalski, ed., Binary Alloy Phase Diagrams. Am. Soc. for Metals, Metals Park, Ohio, 1986.

68. S. Adachi, "Material parameters of $In_{1-x}Ga_xAs_yP_{1-y}$ and related binaries," *J. Appl. Phys.* **53**, 8775-8792 (1982).

69. F. Garofalo, Fundamentals of Creep and Creep-Rupture in Metals. MacMillan, New York, 1965.

70. B. W. Hakki, P. E. Fraley, and T. F. Eltringham, "1.3-μm Laser Reliability Determination for Submarine Cable Systems," *AT&T Tech. J.* **64**, 771-807 (1985).

71. A. R. Goodwin, I. G. A. Davies, R. M. Gibb, and R. H. Murphy, "The design and realization of a high reliability semiconductor laser for single-mode fiber-optical communication links," *J. Light. Tech.* **6**, 1424-1433 (1988).

72. K. Mizuishi, M. Sawai, S. Todoroki, S. Tsuji, M. Hirao, and M. Nakamura, "Reliability of InGaAsP/InP buried heterostructure 1.3 μm lasers," *IEEE J. Quantum Electron.* **QE-19**, 1294-1301 (1983).

73. T. Wilson and C. J. R. Sheppard, Theory and Practice of Scanning Optical Microscopy. Academic Press, London, 1984.

74. A. R. Carlini and T. Wilson, "The role of pinhole size and position in confocal imaging systems," in Scanning Image Technology, T. Wilson and L. Balk, eds., *Proc. SPIE* **809**, 97-100 (1987).

75. M. M. Frocht, Photoelasticity, Vol. 1. Wiley, New York, 1941.

76. M. Ettenberg and R. J. Paff, "Thermal expansion of AlAs," *J. Appl. Phys.* **41**, 3926-3927 (1970).

77. F. Chatenoud, K. M. Dzurko, M. Dion, D. Moss, R. Barber, A. Delage, and D. Landheer, "GaAs-AlGaAs multiple-quantum-well lasers for monolithic integration with optical modulators," *Can. J. Phys.* **69**, 491-496 (1991).

78. K. V. Ravi, Imperfections and Impurities in Semiconductor Silicon. Wiley, New York, 1981.

79. X. Z. Cao and A. F. Witt, "Identification of dislocation etch pits in n-type GaAs by NIR transmission microscopy," *J. Crystal Growth* **114**, 255-257 (1991).

80. P. L. Gourley, I. J. Fritz, and L. R. Dawson, "Controversy of critical layer thickness for InGaAs/GaAs strained-layer epitaxy," *Appl. Phys. Lett.* **52**, 377-379 (1988).

81. G. P. Watson, D. G. Ast, T. J. Anderson, Y. Hayakawa, and B. Pathangey, "The thermal stability of lattice mismatched InGaAs grown on patterned GaAs," *J. Electron. Mater.* **20**, 703-708 (1991).

82. Y. Kohama, Y. Fukuda, and M. Seki, "Determination of the critical layer thickness of $Si_{1-x}Ge_x/Si$ heterostructures by direct observation of misfit dislocations," *Appl. Phys. Lett.* **52**, 380-382 (1988).

83. J. R. Jones, S. H. Jones, M. F. Zybura, L. K. Seidel, and D. K. Oh, "Effects of mesa area and orientation on defects in strained $In_xGa_{1-x}As$ films grown by LPOMCVD," *J. Electron. Mater.* **20**, 709-717 (1991).

84. J. P. Hirth and J. Lothe, Theory of Dislocations. McGraw-Hill, New York, 1968.

85. K. Honda, "Dislocation walls consisting of double arrays in white tin single crystals," *Japanese J. Appl. Phys.* **18**, 215-224 (1979).

86. S. J. Shaibani and P. M. Hazzledine, "The displacement and stress fields of a general dislocation close to a free surface of an isotropic solid," *Phil. Mag. A* **44**, 657-665 (1981).

87. A. K. Head, "Edge dislocations in inhomogeneous media," *Proc. Phys. Soc. B* **66**, 793-801 (1953).

88. F. R. N. Nabarro, Theory of Crystal Dislocations. Clarendon Press (Oxford University Press), Oxford, England, 1967.